

ABSTRACT

ZHANG, SHU. Preparation of $\text{Li}_2\text{MnSiO}_4/\text{C}$ and $\text{LiF}/\text{Fe}/\text{C}$ Nanofiber Cathode Materials for High-Energy Li-Ion Batteries. (Under the direction of Dr. Xiangwu Zhang).

The ever-growing demand of energy and pursuit of renewable energy sources, i.e., wind, solar, and geothermal energies require urgent development of energy storage devices. Li-ion batteries have been considered as one of the most promising candidates as they assume the store energy responsibilities to meet high energy and high power target. Comparing to conventional Ni-Cd and Ni-MH batteries, Li-ion batteries possess overwhelming advantages of high energy density, environmental friendliness, and long cycle life, etc. Most importantly, they weigh less and take less space but deliver more energy. These properties lead to practical applications of Li-ion batteries in various devices with both high power and high energy requirements, from hybrid electric vehicles to consumer electronics such as cell phones and laptops. However, to use Li-ion batteries for large-scale energy storage, they require further improvements on cost, durability, and power density.

Among various factors limiting the performance of Li-ion batteries, the most crucial one relates to the low capacity of current cathode materials. To reach the highest possible cathode capacity, all the possible oxidation states of the active material should be utilized. To address this, our effort has been focused on developing cathode materials with high capacities, including $\text{Li}_2\text{MnSiO}_4$ and LiF/Fe . Unlike most of cathode materials in the commercial market and under scientific research, which can deliver only one electron per formula unit leading to the highest capacity of 167 mAh/g in LiFePO_4 ,

$\text{Li}_2\text{MnSiO}_4$ contains two lithium ions per transitional metal, and the full reduction of transitional metal Mn(II) from Mn(IV) allows complete delithiation of $\text{Li}_2\text{MnSiO}_4$, which potentially enables both lithium ions to be extracted and therefore delivers a high theoretical capacity of around 330 mAh/g. For LiF/Fe, with the reversible conversion reaction of Fe into FeF_3 , three-electron transfer reaction can be realized by utilizing three valent state of metallic Fe, and this leads to a high theoretical capacity of 732 mAh/g. However, both $\text{Li}_2\text{MnSiO}_4$ and LiF/Fe suffer from low intrinsic conductivities, resulting in slow kinetics, and only a small portion of theoretical capacities have been realized.

Our research has devoted to preparing $\text{Li}_2\text{MnSiO}_4/\text{C}$ and LiF/Fe/C nanofibers by electrospinning and heat treatment. These carbon nanofiber-based cathodes facilitate the easy access of Li ions between the active particles, which dramatically promote effective Li ion diffusions, thereby improving the electron/ionic transfer rates and overcome the low intrinsic conductivities of $\text{Li}_2\text{MnSiO}_4$ and LiF/Fe. For $\text{Li}_2\text{MnSiO}_4$, doping treatments including Fe and Cr doping have been conducted to improve other intrinsic properties of $\text{Li}_2\text{MnSiO}_4$, such as unstable crystal structures upon Li ion insertion/extraction. Results show that Li-ion batteries using $\text{Li}_2\text{MnSiO}_4/\text{C}$ and LiF/Fe/C nanofiber cathodes offer advantages of improved energy densities, long cycle life and high discharge capacities. With electrospinning and heat treatment, the process also provides advantages of low cost, easy fabrication, and low pollution. The technological impact of preparing carbon nanofibers with controlled structures and compositions is not only instructive to the fundamental research of overcoming the limits of cathode materials, but also opens up new opportunities to design new-generation Li-ion batteries with high performance and

good safety, which provides the possibility of turning into renewable energies from fossil fuels and coals as a relief of energy crisis.

Preparation of $\text{Li}_2\text{MnSiO}_4/\text{C}$ and $\text{LiF}/\text{Fe}/\text{C}$ Nanofiber Cathode Materials for High-Energy Li-Ion Batteries

by
Shu Zhang

A dissertation submitted to the Graduate Faculty of
North Carolina State University
in partial fulfillment of the
requirements for the degree of
Doctor of Philosophy

Fiber and Polymer Science

Raleigh, North Carolina

2012

APPROVED BY:

Dr. Xiangwu Zhang
Committee Chair

Dr. Peter Fedkiw

Dr. Saad Khan

Dr. Behnam Pourdeyhimi

BIOGRAPHY

Shu Zhang was born in Jiujiang, Jiangxi Province, P.R. China. She attended Nanjing University of Technology, Jiangsu for her undergraduate education and graduated with a Bachelor Degree in Light Chemical Engineering in July 2006. After that, she studied and interned in Modern Analytical Chemistry Institution of Nanjing University, Jiangsu for one year, where she assisted the research work on analyzing the trace amount of minerals in Changjiang River- the mother river of China.

In August 2007, Shu Zhang moved to Raleigh, USA and started her Master's research in College of Textiles. She studied fabrication of oriented nanofibers by electrospinning, and investigated the effect of orientation of fibers on their mechanic properties. In summer 2009, she graduated with a Mater Degree in Textile Engineering in North Carolina State University. In the same year, she joined Dr. Xiangwu Zhang's group and started working toward her Ph.D degree in Fiber and Polymer Science. Her research ranges from designing and preparing carbon nanofibers with active materials and their applications in energy storage, to modifying the intrinsic structure of high-energy cathode materials for Li-ion batteries. In addition to conducting research in the lab, Shu Zhang also enjoys cooking, singing, and playing tennis, especially with the company of her husband.

ACKNOWLEDGMENTS

I would like to thank Dr. Xiangwu Zhang for allowing me to be a member of his laboratory as a graduate student. My experience in his lab has exposed me to a wide breadth of energy materials research, which has been invaluable in my exploration of the field. Additionally, he has supported all of my academic endeavors, and I express sincere gratitude for his guidance and encouragement over the past few years. I also deeply appreciate my committee professors: Dr. Peter Fedkiw, Dr. Saad Khan, and Dr. Behnam Pourdeyhimi for their necessary counsel, direction, and support. It helped me to grow in many aspects.

I would also like to thank all of the graduate students in Dr. Zhang's lab. Their counseling has exponentially advanced my knowledge in nanomaterials for energy storage and has allowed me to be a productive member in the lab. I will, especially miss the daily conversations with my peers in lab 2124. The friendly atmosphere and frequent anecdotes have made my tenure as graduate student more memorable.

Last but not the least, I would like to thank my husband, Xiaofeng Pang, for providing moral support during difficult times and for his help in proof reading the papers generated from the research presented in this dissertation.

TABLE OF CONTENTS

List of Tables.....	viii
List of Figures.....	ix
Chapter 1 Overview of Li-ion Batteries	1
1 Development of Li-ion Batteries.....	1
1.1 Introduction	1
1.2 Structure of Li-ion Batteries	3
1.3 Components of Li-ion Batteries.....	6
1.3.1 Anode.....	6
1.3.2 Cathode	7
1.3.2.1 LiMO ₂ with closely packed lattice structure	7
1.3.2.2 Transition-metal phosphate LiMPO ₄ with olivine structure	9
1.3.2.3 Li ₂ MnSiO ₄ cathode	13
1.3.2.4 LiF/Metal cathode	14
1.3.2.5 Polymer cathodes.....	15
1.3.3 Electrolyte.....	18
1.3.4 Separator.....	20
1.3.5 Other Components.....	21
1.4 Working Mechanism of Li-ion Batteries	22
1.5 Characteristics of Li-ion Batteries	23
1.6 Key Parameters to Evaluate Li-ion Batteries.....	26
1.7 Cathode Structure and Electronic/Ionic Transport	27
2 Overview of Electrospinning	29
2.1 Introduction.....	29

2.2	General Experimental Description.....	31
2.3	Electrospun Inorganic Fibers	33
2.4	Producing Carbon Fibers from Polyacrylonitrile	34
	References	37
	Chapter 2 Research Objectives	46
	References	52
	Chapter 3 Fabrication of $\text{Li}_2\text{MnSiO}_4$/Carbon Composite Nanofibers as High-Capacity Cathode Materials for Li-ion Batteries	53
1	Introduction	53
2	Materials and method	54
3	Results and discussion.....	55
4	Conclusions	60
	References	61
	Chapter 4 High-Capacity $\text{Li}_2\text{Mn}_{0.8}\text{Fe}_{0.2}\text{SiO}_4$/Carbon Composite Nanofiber Cathodes for Lithium-Ion Batteries	63
1	Introduction	63
2	Experimental.....	65
2.1	Chemicals	65
2.2	Preparation of $\text{Li}_2\text{Mn}_{0.8}\text{Fe}_{0.2}\text{SiO}_4$	65
2.3	Fabrication of $\text{Li}_2\text{Mn}_{0.8}\text{Fe}_{0.2}\text{SiO}_4$ /carbon Composite Naofibers.....	66
2.4	Naofiber Chacterizations	66
2.5	Electrochemical Evaluation	67
3	Results and Discussion	67
3.1	X-Ray Diffraction.....	67

3.2	Morphology and Structure	69
3.3	Raman Analysis.....	72
3.4	Electrochemical Properties.....	73
3.5	Conclusions.....	77
References		77
 Chapter 5 Cr-Doped Li₂MnSiO₄/Carbon Composite Nanofibers as High-Energy		
Cathodes for Li-Ion Batteries.....		79
1	Introduction	79
2	Experimental.....	81
2.1	Chemicals	81
2.2	Li ₂ Mn _(1-x) Cr _x SiO ₄ Preparations	81
2.3	Li ₂ Mn _(1-x) Cr _x SiO ₄ /carbon composite Nanofibers Frabrication	82
2.4	Nanofiber Characterization	83
2.5	Electrochemical Evaluation.....	83
3	Results and Discussion	84
3.1	Morphology and Strucyture Characterization.....	84
3.2	X-ray Diffraction Analysis.....	87
3.3	Electrochemical Performance	90
4	Conclusions	94
References		95
 Chapter 6 LiF/Fe/Carbon Nanofibers as High-Energy Cathode Materials for Li-Ion		
Batteries		97
1	Introduction	97
2	Experimental.....	100

2.1	Chemicals	100
2.2	$\text{Li}_2\text{Mn}_{(1-x)}\text{Cr}_x\text{SiO}_4$ Preparations	100
2.3	$\text{Li}_2\text{Mn}_{(1-x)}\text{Cr}_x\text{SiO}_4$ /carbon composite Nanofibers Frabrication	101
2.4	Electrochemical Evaluation.....	101
3	Results and Discussion	102
3.1	Elemental Analysis	102
3.2	Morphology and Strucytue Characterization.....	103
3.3	Electrochemical Performance	108
4	Conclusions	112
	References	112
	Chapter 7 Recommended Future Work	115

LIST OF TABLES

Table 1-1. Comparisons between different anode materials	7
Table 1-2. Properties of popular high-energy cathode materials	18
Table 1-3. Comparisons of different types of secondary batteries.....	24
Table 2-1. Important factors affecting electrospinning process	33
Table 5-1. Lattice parameters for $\text{Li}_2\text{MnSiO}_4$	88

LIST OF FIGURES

Figure 1-1. Ragon plot of electrochemical devices.....	2
Figure 1-2. 18650 Cylindrical Li-ion battery.....	4
Figure 1-3. Prismatic Li-ion battery.....	5
Figure 1-4. Li-ion coin cells.....	5
Figure 1-5. Layered structure of LiMO_2 , showing the lithium ions between the transition-metal oxide sheet	8
Figure 1-6. SEM and TEM images of hydrothermally-prepared LiCoO_2	9
Figure 1-7. Crystal structure of LiFePO_4	10
Figure 1-8. (a) low-magnification image of the nanowire; (b) magnified part in (a); (c) magnified part in (b).....	12
Figure 1-9. Charge/discharge curves of uncoated LiFePO_4 and $\text{LiFePO}_4/\text{CNT}$ nanocomposite with different ratio	13
Figure 1-10. Schematic of the energy storage of LBL-MWNT electrodes.....	17
Figure 1-11. Cyclic voltammogram of LBL-MWNT electrode.....	18
Figure 1-12. SEM surface photomicrograph of Celgard monolayer PP battery separator	22
Figure 1-13. Schematic charge/discharge mechanism of a Li-ion battery.....	24
Figure 1-14. Decreasing surface area of a particle during lithiation.....	31
Figure 1-15. Graphic illustration of graphene hexagonal layers.....	32
Figure 1-16. Electrospinning set-up.....	34
Figure 1-17. Molecular structure of PAN	36

Figure 1-18. Stabilization of PAN under air at 250-300°C and graphinization under argon at 700-800°C	37
Figure 2-1. Samples prepared from a combined method of electrospinning and heat-treatment can be directly used in Li-ion batteries	52
Figure 2-2. Electronic characterizations of $\text{Li}_2\text{MnSiO}_4$ and $\text{Li}_2\text{FeSiO}_4$	62
Figure 3-1. SEM images of $\text{Li}_2\text{MnSiO}_4$ particle at different magnifications.....	63
Figure 3-2. SEM images of electrospun $\text{Li}_2\text{MnSiO}_4/\text{PAN}$ nanofibers (A, B, and C) and $\text{Li}_2\text{MnSiO}_4/\text{carbon}$ nanofibers (D and E) at different magnifications.....	64
Figure 3-3. TEM image of a $\text{Li}_2\text{MnSiO}_4/\text{carbon}$ composite nanofiber.....	65
Figure 3-4. X-ray diffraction patterns of (A) $\text{Li}_2\text{MnSiO}_4$ powder, and (B) $\text{Li}_2\text{MnSiO}_4/\text{carbon}$ nanofibers.....	66
Figure 3-5. Galvanostatic charge-discharge curves of (A) $\text{Li}_2\text{MnSiO}_4$ powder, and (B) $\text{Li}_2\text{MnSiO}_4/\text{carbon}$ nanofibers	75
Figure 4-1. patterns of (A) $\text{Li}_2\text{MnSiO}_4$ and (B) $\text{Li}_2\text{Mn}_{0.8}\text{Fe}_{0.2}\text{SiO}_4$ powders	76
Figure 4-2. SEM images of (A) $\text{Li}_2\text{MnSiO}_4$ and (B) $\text{Li}_2\text{Mn}_{0.8}\text{Fe}_{0.2}\text{SiO}_4$ powders	77
Figure 4-3. SEM image of electrospun $\text{Li}_2\text{Mn}_{0.8}\text{Fe}_{0.2}\text{SiO}_4/\text{PAN}$ nanofibers.....	78
Figure 4-4. SEM images of $\text{Li}_2\text{Mn}_{0.8}\text{Fe}_{0.2}\text{SiO}_4/\text{carbon}$ nanofibers obtained after heat-treatment	78
Figure 4-5. TEM images of $\text{Li}_2\text{Mn}_{0.8}\text{Fe}_{0.2}\text{SiO}_4/\text{carbon}$ nanofibers with magnifications of (A) $10,000\times$ and (B and C) $30,000\times$	78
Figure 4-6. Raman Raman spectrum of $\text{Li}_2\text{Mn}_{0.8}\text{Fe}_{0.2}\text{SiO}_4/\text{carbon}$ composite nanofibers.....	80

Figure 4-7. Charge-discharge curves of (A) $\text{Li}_2\text{MnSiO}_4$ powder, (B) $\text{Li}_2\text{Mn}_{0.8}\text{Fe}_{0.2}\text{SiO}_4$ powder, and (C) $\text{Li}_2\text{Mn}_{0.8}\text{Fe}_{0.2}\text{SiO}_4$ /carbon nanofibers	82
Figure 4-8. Cycling performance of $\text{Li}_2\text{MnSiO}_4$ powder, $\text{Li}_2\text{Mn}_{0.8}\text{Fe}_{0.2}\text{SiO}_4$ powder, and $\text{Li}_2\text{Mn}_{0.8}\text{Fe}_{0.2}\text{SiO}_4$ /carbon nanofibers	83
Figure 5-1. SEM images of (A and B) $\text{Li}_2\text{MnSiO}_4$ and (C and D) $\text{Li}_2\text{Mn}_{0.94}\text{Cr}_{0.06}\text{SiO}_4$ powders.....	93
Figure 5-2. SEM images of $\text{Li}_2\text{Mn}_{0.94}\text{Cr}_{0.06}\text{SiO}_4$ /PAN nanofibers	94
Figure 5-3. SEM images of $\text{Li}_2\text{Mn}_{0.94}\text{Cr}_{0.06}\text{SiO}_4$ /carbon nanofibers.....	94
Figure 5-4. TEM images of $\text{Li}_2\text{Mn}_{0.94}\text{Cr}_{0.06}\text{SiO}_4$ /carbon nanofibers with different magnifications of (A) 20,000 \times , and (B, C, and D) 30,000 \times	95
Figure 5-5. XRD diffractions of (A) $\text{Li}_2\text{MnSiO}_4$ and (B) $\text{Li}_2\text{Mn}_{(1-x)}\text{Cr}_x\text{SiO}_4$ (a: $x=0.03$, b: $x=0.06$, and c: $x=0.10$)	98
Figure 5-6. Charge-discharge curves of (A) $\text{Li}_2\text{MnSiO}_4$, and $\text{Li}_2\text{Mn}_{(1-x)}\text{Cr}_x\text{SiO}_4$ powders with (B) $x=0.03$, (C) $x=0.06$, and (D) $x=0.10$	100
Figure 5-7. Charge-discharge curves of $\text{Li}_2\text{Mn}_{0.94}\text{Cr}_{0.06}\text{SiO}_4$ /carbon nanofibers....	102
Figure 5-8. Cycling performance of $\text{Li}_2\text{MnSiO}_4$ powder, $\text{Li}_2\text{Mn}_{0.94}\text{Cr}_{0.06}\text{SiO}_4$ powder, and $\text{Li}_2\text{Mn}_{0.94}\text{Cr}_{0.06}\text{SiO}_4$ /carbon nanofibers.....	103
Figure 6-1. X-ray diffraction pattern of LiF/Fe/C composite nanofibers prepared from 16 wt% precursor solution	112
Figure 6-2. Energy-dispersive X-ray spectrum of LiF/Fe/C composite nanofibers prepared from 16 wt% precursor solution	113
Figure 6-3. SEM images of LiF/ferrocene/PAN nanofibers electrospun from: (a,b)	

11, (c,d) 16, (e,f) 21, and (g,h) 26 wt% precursor solutions	114
Figure 6-4. Diameter distributions of LiF/ferrocene/PAN nanofibers prepared from:	
(a) 11, (b) 16, (c) 21, and (d) 26 wt% precursor solutions.....	115
Figure 6-5. SEM images of LiF/Fe/C nanofibers prepared from: (a,b) 11, (c,d) 16,	
(e,f) 21, and (g,h) 26 wt% precursor solutions	117
Figure 6-6. Diameter distributions of LiF/Fe/C nanofibers prepared from: (a) 11, (b)	
16, (c) 21, and (d) 26 wt% precursor solutions.....	117
Figure 6-7. Backscatter SEM images of LiF/Fe/C composite nanofibers prepared	
from 21 wt% precursor solution. The bright dots indicate LiF and Fe particles	118
Figure 6-8. Galvanic charge-discharge curves of LiF/Fe/C nanofibers prepared from:	
(a) 11, (b) 16, (c) 21, and (d) 26 wt% precursor solutions.....	120
Figure 6-9. Cycling performance of LiF/Fe/C nanofiber composites prepared from	
precursor solutions with different concentrations.....	121

Chapter 1 Overview of Li-ion Batteries

1. Development of Li-ion Batteries

1.1. Introduction

Energy is a central societal issue, impacting our way of life, world economy, environment, and human health. Although combustion-based energy technologies continue to play a dominant role in meeting our energy needs, it comes at a huge price: rapid increase in greenhouse gas emissions, long lasting environmental consequences, and global climate change [1]. With increasing exhaustion of chemical energy source, people have recognized the importance and urgency of developing and utilizing new generation energy nowadays.

Many nations around the world have put tremendous manpower and material resources on developing sustainable alternative energy source. Among many renewable energy sources, wind and solar power have attracted the most interest. However, they both suffer from the problems of instability and location dependence. Therefore, energy storage devices are required. The ever-growing demand for compact, high-energy density electrochemical energy storage has led to the development of advanced batteries.

Batteries have so far found the largest commercial market compared to fuel cells and supercapacitors and fill an intermediate region on the Ragone plot (shown in Fig.1-1) of specific power versus specific energy [2]. Li-ion batteries are considered to be one of the most promising technologies among all batteries. They have been commonly used in compact electronics such as laptops, mobile phones, cameras, etc. In addition, they have been considered to be one of the best candidates for applications in electrical vehicles

(EVs) and hybrid electrical vehicles (HEVs).

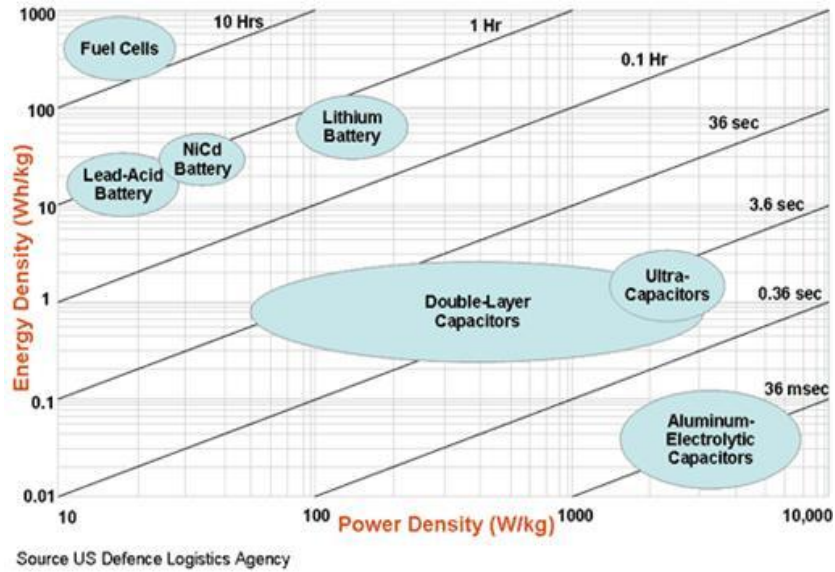


Figure 1-1. Ragone plot of electrochemical devices [3].

Li-ion batteries originated from lithium batteries. Lithium batteries include lithium primary batteries and lithium secondary batteries. They both use metallic lithium as the anode. The atomic weight of lithium is 6.94, and its density is 0.53 g/cm³, which makes it the lightest metal. In addition, with a relative potential versus standard hydrogen electrode (SHE) of -3.04 V, lithium has the lowest redox potential among all known elements. All these characteristics result in the highest output potential when using lithium as the anode of a battery. Furthermore, the diameter of a lithium ion is only around 0.78 Å, facilitating reversible extraction/insertion of lithium ions out of /into the crystal unit of transition metal in the cathode.

The research of lithium primary batteries started in 1950's. The energy crisis in 1960's

initiated a great progress on the development of lithium primary batteries, which directly promoted their commercialization in 1970's. However, due to the growing of lithium crystal branches on lithium anode during repeated charging and discharging processes, Lithium secondary batteries not only suffer from poor cycling performance, but more importantly, serious safety issue. This strongly inhibited its industrialized production. Until 1980's, as graphite with lattice structure was used as the replacement of metallic lithium anode, pairing with composite oxides of lithium and transition metal as the cathodes, Li-ion batteries were developed and produced. Sony pervaded our life in 1990's by introducing the first LiCoO_2 /graphite lithium ion battery in market. The commercialization of Li-ion batteries officially began since then.

As we entered the 21st century, Li-ion batteries experienced a swift and violent development, with a major trend over Ni/Cd batteries and Ni/MH batteries. An economic crisis is often followed by a technological revolution. The financial crisis in early 21st century was believed to be a cradle of new-generation energy revolution. Great expectations have been placed on Li-ion batteries for power supply.

1.2. Structure of Li-ion Batteries

Based on appearance, Li-ion batteries can be defined as cylindrical Li-ion battery and prismatic Li-ion battery. Fig. 1-2 shows a standard cylindrical Li-ion battery, i.e. 18650-type steel shell Li-ion battery, in which 18 means the diameter of 18 mm, and 650 represents the height of 65.0 mm. Generally, there are five digits in the label of cylindrical batteries, with the first two digits indicating the outer diameter of the battery

in the unit of millimeter and last three digits representing the overall height of the battery in the unit of tenth of millimeter. A cylindrical Li-ion battery is typically assembled by wrapping the cathode, separator and anode around a conducting pole, followed by placing the whole package in a cylindrical steel can, injecting electrolyte, and sealing product.

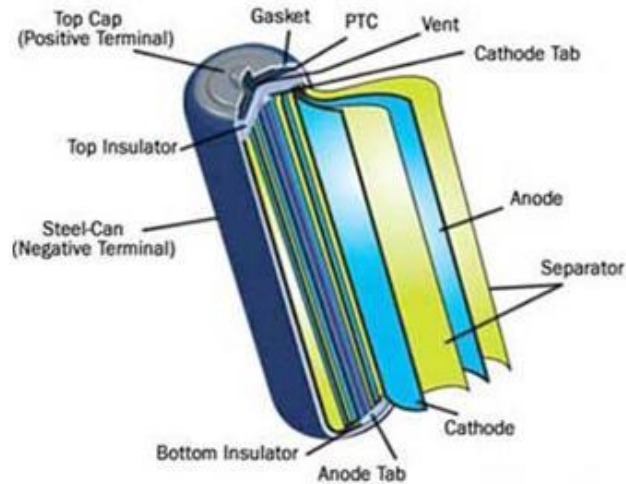


Figure 1-2. 18650 cylindrical Li-ion battery.

Fig. 1-3 visually presents the appearance of a prismatic Li-ion battery. Unlike cylindrical Li-ion batteries, some prismatic Li-ion batteries are represented by six digits instead of five, with first two digits for thickness, third and fourth digits for width, and last two digits for length. Prismatic Li-ion batteries have the same inner structure as cylindrical Li-ion batteries, *i.e.*, anode, cathode, separator and electrolyte. But the battery shell materials vary from aluminum-plastic to stainless steel depending on the type of application.

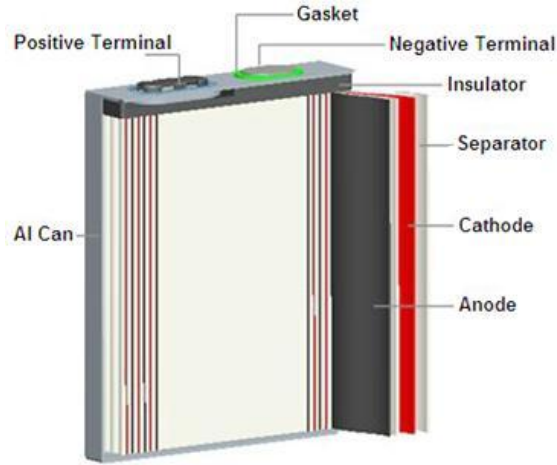


Figure 1-3. Prismatic Li-ion battery.

In addition to these two types of Li-ion batteries, Li-ion coin type batteries are also common (shown in Fig. 1-4). With a straightforward structure, coin type Li-ion batteries are normally used for laboratory research or testing.



Figure 1-4. Li-ion coin cells.

1.3. Components of Li-ion Batteries

The major components of Li-ion batteries are anode, cathode, electrolyte, separator, and PTC terminal, etc.

1.3.1. Anode

Electrodes in Li-ion batteries are usually composed of active material, conducting agent, binder, and current collector. An anode is the low-potential electrode where oxidation reaction occurs. Graphite and carbon with a structure of graphitic layers are usually used as the active material in the anode. Spinel-structured $\text{Li}_4\text{Ti}_5\text{O}_{12}$ has also been commercialized in addition to graphitic materials as an important candidate for HEV/EVs. Moreover, new types of silicon and tin based, and transition metal anodes have attracted significant interest in recent years. Table 1-1 [4-8] lists the most commonly studied anode materials. Normally the anode is under lower potential than the cathode, copper is used as the anode current collector of anode because of its strong resistance to being reduced.

Table 1-1. Comparisons between different anode materials

Anode Material	Characteristics
Graphite (lattice structure)	Pros: High conductivity; working potential close to lithium anode; LiC_6 when fully charged; theoretical capacity of 372 mAh/g. Cons: can be easily stripped due to the Van Der Waals force supporting between layers; poor compatibility with electrolyte; only artificial graphite can be used.
Ungraphitised Carbon	Includes soft carbon and hard carbon, both are amorphous; good compatibility with electrolyte; Soft carbon is the mostly used anode in power batteries; Hard carbon is paralyzed from polymers with very high surface area and higher reversible capacity than graphite (~400 mAh/g).
$\text{Li}_4\text{Ti}_5\text{O}_{12}$ (spinel structure)	Pros: flat discharge plateau (~1.55V); good compatibility with different electrolytes; very small volume change during charge and discharge; Cons: low conductivity; low capacity of 176 mAh/g.
Transition Metal Oxide	Pros: high capacity; excellent rate performance; Cons: high cost; poor cycling performance; high initial capacity loss.
Silicone Based Material	Pros: high theoretical capacity of over 4000 mAh/g; Cons: huge volume expansion; poor cycling performance (but can be minimized by nanofabrication or making it as composite).
Tin Based Material	Pros: high specific capacity; safe; Cons: volume expansion; poor cycling performance.

1.3.2. Cathode

A cathode is consequently the sink of lithium ions [9] by intercalation in the crystal structure with high redox potential where reduction occurs. Cathode materials can be categorized based on their crystalline structure, including but not limited to lattice structure, olivine structure, and monoclinic structure.

1.3.2.1. LiMO_2 (M= Co, Ni, or Mn) with closely packed lattice structure

In this type of materials, microscopically alternative sheets of transition metal (Co, Ni, or Mn) oxides are parallelly layered to two sides of the lithium ions on plane 111. The stacking of layers builds up to form a hexagonal cell with relatively long interlayer distance and short metal-to-metal distance [10]. This special structure leads to facile

lithium intercalation sites (Fig. 1-5).

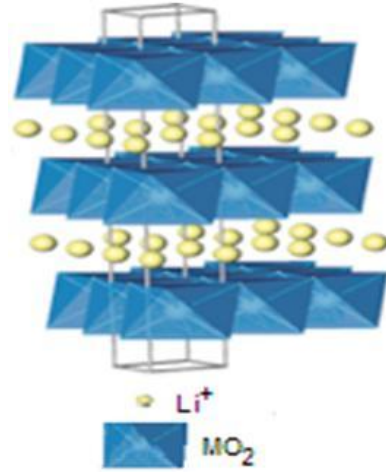
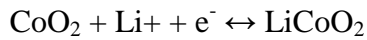


Figure 1-5. Layered structure of LiMO₂, showing the lithium ions between the transition- metal oxide sheets [11].

The most commonly used transition metal is cobalt due to its advantages of cost and battery cycle life. The conversion reaction on electrodes for LiCoO₂ is written as below.



Even though LiCoO₂ has decent ion diffusion coefficient, LiCoO₂ powders prepared by conventional method have large particle size (>1 μm). As a result, this material suffers from relatively low electronic conductivity (10⁻³ S/cm) [12]. In addition, the surface area is not large enough to contact the electrolyte at this size scale, therefore lithium ions are not able to be transported quickly into the layered structure [10] leading to low capacity and power density.

Therefore, reducing the particle size becomes very critical to improve the kinetics of lithium ion transportation by shortening diffusion distance and enlarging surface area [12]. Active research has been conducted on preparing LiCoO_2 particles at nanoscale. Cho's group produced LiCoO_2 particles with sizes of around 150 nm through a hydrothermal method [10] (shown in Fig. 1-6).

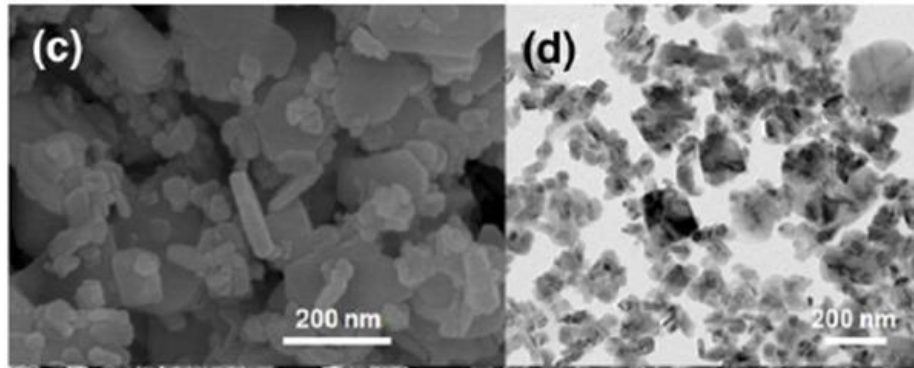


Figure 1-6. SEM (c) and TEM (d) images of hydrothermally prepared LiCoO_2 [10].

LiCoO_2 has been subjected to the basis of most commercial cells during the past 25 years. However, the chemical and thermal instability of LiCoO_2 is a substantial limitation. A strong research effort has been focused on finding new cathode materials to replace LiCoO_2 [13].

1.3.2.2. Transition-metal Phosphate LiMPO_4 (M=Fe, Mn, or Ni) with Olivine Structure

Lithium transition metal phosphate is gaining significant attention since Goodenough

discovered LiFePO_4 in 1997. This family of cathode material provides overwhelming advantages of low cost, good cycling performance, excellent thermal stability, and low toxicity.

Lithium transition- metal phosphate typically has an olivine structure. This structure has hexagonally close-packed oxygen array, in which the octahedral share both edges and faces. Different from the layered structure of LiCoO_2 , there is no continuous network of FeO_6 edge-shared octahedral that may contribute to electronic conductivity, and divalent Fe^{2+} ions occupy corner shared octahedral instead. The phosphorous ions are located in tetrahedral sites, and the lithium ions reside in chains of edge shared octahedral as shown in Fig. 1-7.

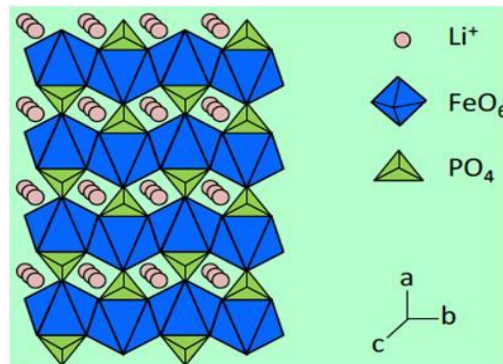
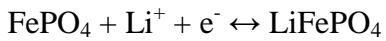


Figure 1-7. Crystal structure of LiFePO_4 [14].

LiMPO_4 ($M=\text{Fe}$, Mn , or Ni) includes one Li^+ ion per formula unit that can be extracted and transferred to the anode in the first charge process, compensating for the oxidation of transition metal (e.g. Fe^{2+} to Fe^{3+}). Only a small volume reduction is included during

charge process from LiMPO_4 to MPO_4 , as calculated from the change in lattice constant.

This volume reduction compensates for the volume expansion of the anode and contributes to efficient use of the volume of a practical Li-ion battery [15]. The conversion reaction at the cathode is expressed as:



Similar to LiCoO_2 , the main obstacle which prevents LiMPO_4 from reaching theoretical capacity is its low intrinsic electronic conductivity. This is due to the one-dimensional paths in olivine structure. Lithium motions are confined within these tunnels with little possibility of crossing between channels. Moreover, these one-dimensional paths can be easily blocked by impurities and defects, resulting in slow lithium ion diffusion.

Nanostructured LiFePO_4 incorporated with carbon coating has been investigated to improve the electronic conductivity and lithium ion diffusion.

Recently, Honoson's research groups synthesized a triaxial LiFePO_4 nanowire with a multiwall carbon nanotube core and an amorphous carbon shell through the electrospinning method [16] (shown in Fig. 1-8). The performance of the LiFePO_4 cathode is greatly enhanced by this approach due to the combined effect of smaller lithium diffusion path length and electronically conductive matrix provided by carbon nanotubes.

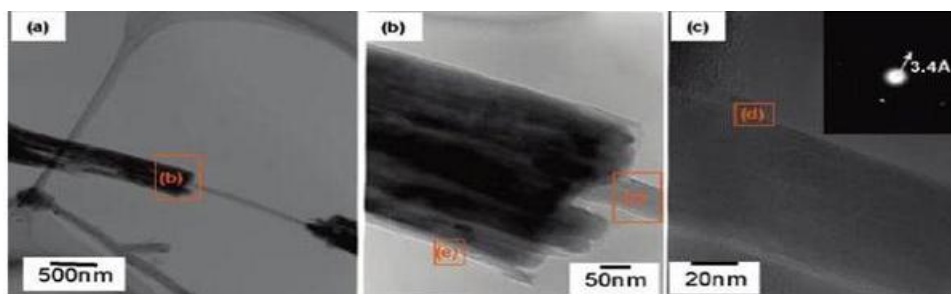


Figure 1-8. (a) low- magnification image of the nanowire; (b) magnified part in (a); (c) magnified part in (b) [16].

Some other research groups are also making efforts to control the particle sizes at a small scale aiding to realize a better electrochemical utilization of LiFePO_4 by making it into LiFePO_4 /polymer nanocomposite. For example, Manthiram's group encapsulated the LiFePO_4 within an electronically and ionically conducting p-toluene sulfonic acid doped poly(3,4-ethylenedioxy thiophene) at ambient temperatures to obtain an organic-inorganic nanocomposite [15]. This nanocomposite cathode offers a capacity of 166 mAh/g, which is very close to the theoretical value of 170 mAh/g. With LiFePO_4 encapsulated in carbon nanotubes Manthiram's group, the data in Fig. 1-9 also demonstrate that both minimizing particle sizes and coating with conductive material are essential in improving the electrochemical properties of olivine LiFePO_4 .

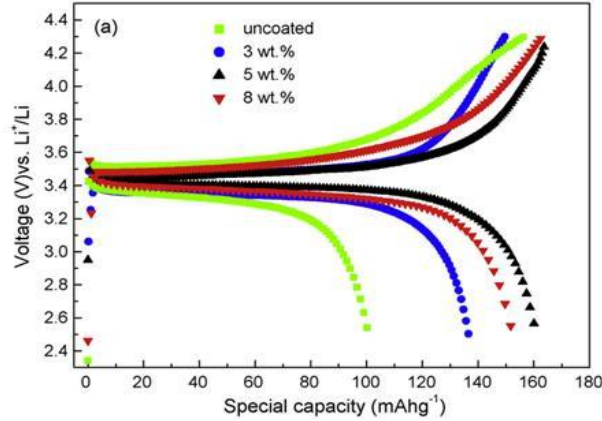


Figure 1-9. Charge/discharge curves of uncoated LiFePO_4 and $\text{LiFePO}_4/\text{CNT}$ nanocomposite with different ratios [17].

1.3.2.3. $\text{Li}_2\text{MnSiO}_4$ Cathode

Goodenough's [18] discovery of LiFePO_4 as cathode materials has changed the landscape of Li-ion batteries due to its high stability and reliable safety. However, LiFePO_4 can only provide one lithium ion per formula unit, and hence its theoretical capacity is only 167 mAh/g [19,20]. Nyten [21, 22] firstly synthesized and characterized $\text{Li}_2\text{FeSiO}_4$, which not only has the same benefits as LiFePO_4 , but also can theoretically extract two lithium ions per formula unit from the structure. The extraction of two lithium ions leads to a high theoretical capacity of 320 mAh/g for $\text{Li}_2\text{FeSiO}_4$. However, electrochemical tests only realized up to 1 lithium extraction per transitional metal in practice due to the poor conductivity and slow kinetics [20-23]. Dominko [23] then proposed the substitution of Fe with Mn. It was anticipated that with two redox pairs of Mn(II)/Mn(III) and Mn(III)/Mn(IV) , two-electron reaction could become possible, corresponding to a high theoretical capacity of 332 mAh/g. However, they only achieved 0.7 lithium ion per

formula unit during charge/discharge.

The poor conductivity (5×10^{-16} S/cm) and slow kinetics of $\text{Li}_2\text{MnSiO}_4$ are probably the main reason why researchers have not been able to extract more than one lithium ion per formula unit [24]. To circumvent the low electronic conductivity and slow kinetics of the lithium orthosilicate, several methods were employed including size reduction [25], carbon coating [26], and super-valent metal doping [27]. Although progress has been made by these methods, the overall performance of $\text{Li}_2\text{MnSiO}_4$ is still not sufficient for practical battery applications. A strategy that can increase the conductivity, stabilize the crystal structure and improve the performance of $\text{Li}_2\text{MnSiO}_4$ is in urgent need.

1.3.2.4. LiF/Metal Cathode

Among various factors contributing to the performance of Li-ion batteries, the most crucial one relates to the capacity of cathode material [28]. To reach the highest specific capacity of a cathode material, all the possible oxidation states of a compound should be utilized [29]. Iron trifluoride (FeF_3) was firstly studied by Arai et al. [30] because of its high theoretical capacity (237 mAh/g per 1 e^- transfer). However, due to the insulative nature of FeF_3 with low conductivity of 10^{-17} S cm^{-1} [31], the observed reversible capacity was only around 80 mAh/g, and since then this material has been ignored as a potential candidate for cathode materials. The conversion reaction of this cathode material is written as:



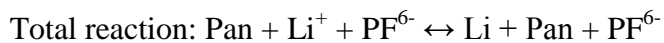
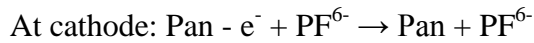
Previous studies also pointed out that it is essential to improve the transport properties of FeF_3 , which can be achieved by decreasing particle size, adding conductive additives, modifying surface, and optimizing microstructure [29,32]. Badway et al. demonstrated a highly reversible capacity of 600 mAh/g from FeF_3 by making it into carbon/ FeF_3 nanocomposites through high-energy milling. It was believed that nanosized carbon crystals introduced a greater number of surface defects and enhanced both electronic and ionic conductivities [33].

An alternative way to make carbon/metal fluoride nanocomposites is to grow thin films consisting of either FeF_3 and conductor additives or LiF and pure metal. In this method, the separations between LiF and Fe could be prevented. Many different techniques were employed including pulsed laser deposition (PLD) [34,35], ultrahigh vacuum evaporation [36,37], and combinatorial sputtering [38]. However, no detailed performance was reported and the needs for usage of precision instruments limited their practical applications. Furthermore, to be used in rechargeable Li-ion batteries, iron must be in the metallic form as the initial component to prelithiate the cathode [39]. Therefore, it is essential to explore a more feasible method to both produce metallic iron and enhance the conductivity of LiF/metal composite.

1.3.2.5. Polymer Cathodes

The history of conductive polymer started since the discovery of polyacetylene. Not until recently, studies began to make an attempt at using conductive polymer in Li-ion batteries due to its low cost and high capacitance comparing to conventional cathodes.

The most widely studied polymer materials for cathode include two groups: the first group includes polyaniline, polypyrrole, and polythiophene, etc., with the ability of p-type doping. Take Li/LiPF₆/PAN battery as an example. The one-electron transfer reactions in this battery are:



The second group is polymers with functional groups so that redox reactions can occur on the surface to store energy. Lee assembled a cathode material for Li-ion batteries based on functionalized multiwalled carbon nanotubes (MWNT) that include stable pseudo-capacitive functional groups using layer-by-layer (LBL) technique (Fig. 1-10) [40].

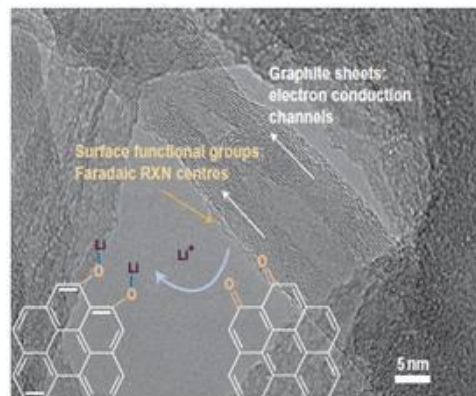


Figure 1-10. Schematic of the energy storage of LBL-MWNT electrodes. Faradaic reactions between surface oxygen species and Li schematically illustrated on an HRTEM image [40].

The cyclic voltammogram of Fig. 1-11 indicates a surface-redox limited process with the evidence that the current at around 3V increases linearly with scan rate. That means the capacitance comparable to electrochemical capacitor can be realized by enlarging the surface area of functionalized polymer cathodes.

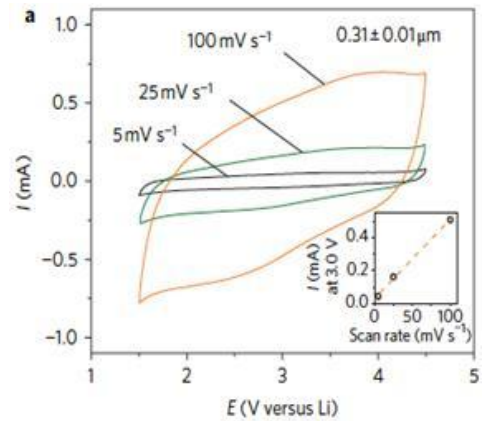


Figure 1-11. Cyclic voltammogram of LBL-MWNT electrode [40].

Beside the above- introduced cathode materials, research has been extended to other new materials to meet high energy target. Table 1-2 lists the most attractive or most studied cathode materials [41-48].

Table 1-2. Comparisons between high-energy cathode materials for Li-ion batteries [26-48].

Cathode Materials	Advantages	Disadvantages
Li[Ni _{1-x} Mx]O ₂ (M=metal) [19]	1. high reversible capacity (~200 mAh/g) 2. excellent cycling and safety characteristics	1. poor thermal characteristics due to oxygen release from the highly delithiated state 2. high interfacial cell impedance resulted from high concentration of unstable Ni ⁴⁺ during charging
LiMnPO ₄ [20]	1. higher redox potential (~4.1V) than LiFePO ₄ 2. low energy cost	1. high ionic and electronic resistance 2. debate on electrochemical stability
LiVPO ₄ F [21]	1. average lithium-de intercalation-intercalation voltage is ~4.2V 2. good thermal stability 3. good cycling performance	has not been reported yet
Li ₂ CoPO ₄ F [22]	1. high working plateau (~5V) 2. theoretically two Li ⁺ ion can be extracted	1. hard to find a working electrolyte at 5V 2. only one Li ⁺ ion can be reversibly cycled

1.3.3. Electrolyte

The electrolyte system in Li-ion batteries is normally a solution system containing mixed organic solvent and lithium salt. The majority of mixed organic solvents are non-proton polar solvents. They are with high dielectric constants, do not react with lithium, and

allow a maximum solvation of lithium salt. However, a higher dielectric constant usually means a higher viscosity, which may result in a higher resistance to ion migration. As such, a less viscous solvent is coupled with high dielectric constant solvents to make the viscosity of the mixed electrolyte solution favorable for ion movements.

For solute, univalent polyanionic lithium salt, such as LiPF_6 , LiClO_4 , LiBF_4 , LiAsF_6 , lithium perfluoroalkyl sulfonate (e.g. LiCF_3SO_3), and lithium bis(perfluoroalkyl) sulfonate (e.g. $\text{LiN}(\text{CF}_3\text{SO}_2)_2$ and $\text{LiN}(\text{C}_2\text{F}_5\text{SO}_2)_2$) are commonly used. Lithium ions with larger sizes dissociate more easily, leading to more ion migration, which ensures a higher electronic conductivity. LiClO_4 has the oldest history with an appropriate conductivity, thermal and oxygen stability. However, it can only be used for research purpose instead of industrial production due to the safety issue caused by its strong ability of oxidation. A distinctive disadvantage of LiBF_4 is its low ionic conductivity resulted from the relatively small ion size. Among all other lithium salts, LiAsF_6 , possesses the highest electronic conductivity, but it suffers from carcinogenic potential of As which hinders its application. While both $\text{LiN}(\text{CF}_3\text{SO}_2)_2$ and LiCF_3SO_3 are corrosive to current collector, LiPF_6 although has poor thermal stability and relatively high water solubility, it has still been extensively used in commercial Li-ion batteries. Another newly developed lithium salt lithium bis(oxalato)borate (LiBOB) is considered as the most promising substitute of LiPF_6 due to its advantages of low cost, excellent thermal stability and good overall electrochemical properties. The only problem of LiBOB is low solubility and low conductivity.

In electrolyte system, besides lithium salt, there might be some other functional additives

including film-forming agent, overcharge protecting agent, and fire retardant [49-52].

1.3.4. Separator

The separator is also essential in Li-ion batteries to physically separate the anode and cathode. It allows the transport of lithium ions and prevents a short circuit. Most commercial separators are polyethylene and polypropylene mesoporous membrane. Fig. 1-12 is a Celgard 2400 separator with a thickness of 25 μm , 37% porosity, and pore size of 0.117 μm -0.042 μm [53]. The thickness of separator is very important. The separator cannot be either too thick or too thin because thicker membrane will result in higher inner impedance of the battery, while thinner separators tend to be less durable and more safety hazardous. The separator showed in Fig. 1-12 has a melting point of around 120 $^{\circ}\text{C}$, and high temperature shrinkage of 2% to prevent short circuit caused by overheating. Melting point is also critical since overcharging will bring a temperature increase to the melting point, leading to membrane pore closure and consequently a rapid increase in inner impedance to cut the circuit as a protection. Therefore, polypropylene with a melting temperature of 165 $^{\circ}\text{C}$ is better as a separator material than polyethylene and in terms of safety. In addition, a higher melting temperature enables a higher dimensional stability under high temperature, therefore polypropylene in another way can sustain a better shape than polyethylene to reduce the risk of short circuit caused by separator melting. To balance the benefits of both polyethylene and polypropylene, Celgard introduced new separators with a three-layer structure of PP/PE/PP. The PP on two sides can keep the shape while the PE in the middle layer can provide higher impedance if the

battery is overcharged.

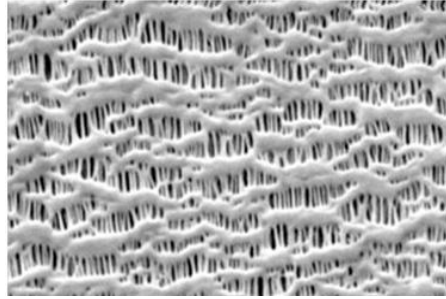


Figure 1-12. SEM surface photomicrograph of Celgard monolayer PP battery separator [53].

1.3.5. Other Components

Beside electrodes, electrolytes, and separators, commercial Li-ion batteries also contain positive temperature coefficient thermistor (PTC) terminals and safety valves. PTC terminals work as recoverable fuses. When they reach certain temperature, their impedance increases rapidly to cut off the circuit; when the temperature decreases, they will return to the low impedance status, and the circuit will be recovered. This process can be repeated up to thousands of times.

PTC terminals are normally made up with specially treated polymers and conductive agents such as carbon black. Under normal circumstances, the polymer attracts conductive agent particles tightly packed within its amorphous phase, which produces low impedance. The current flow through the bonds creates such low heat that it cannot change the crystalline structure of the polymer and keep the current flowing.

While with a presence of sharp increase in current, the temperature of recoverable fuse will increase rapidly. The crystalline polymer will become amorphous under high temperature, and the expansion of the polymer matrix will draw apart the highly packed conductive particles resulting in a significant increase in impedance. In this way, the current flow will be cut back, and the whole system can be protected. When the current reduces, the temperature of the polymer will also decrease to a normal level, and the low impedance bonds of closely packed conductive agents on polymer chains will be rebuilt. For safety vent, it can be automatically switched on to release high pressure in the battery to prevent battery explosion and provide additional protection.

1.4. Working Mechanism of Li-ion Batteries

During charge and discharge, the difference in potentials at two electrodes drives lithium ions back and forth through the electrolyte between the anode and cathode, while electrons through the external circuit [54]. When a battery is charged, lithium is extracted in the form of ions from the cathode, and move through the electrolyte into the anode. In the same time, electrons move to the anode through external circuit. The process reverses when the battery is discharged with lithium ions moving back from the anode to the cathode. Therefore, Li-ion batteries were also called "rocking chair" batteries to describe the to and fro transportation of lithium ions between two electrodes. Because both charge and discharge are realized by the movement of lithium ions without the presence of metallic lithium, this type of batteries are called "lithium ion" batteries. Fig. 1-13 schematically illustrates the charge/discharge mechanism of Li-ion batteries.

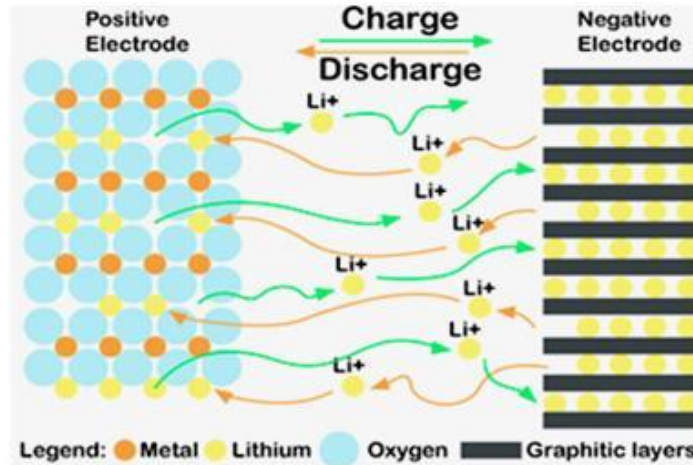
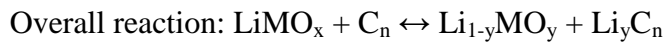
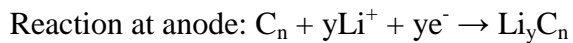
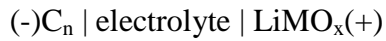


Figure 1-13. Schematic charge/discharge mechanism of a Li-ion battery [55].

The electrochemical expression for the Li-ion battery shown in Fig. 1-5 is written as



1.5. Characteristics of Li-ion Batteries

Table 1-3 lists the major characteristic difference of Li-ion batteries comparing to traditional Ni/Cd and Ni/MH batteries.

Table 1-3. Comparisons of different types of secondary batteries [56-61].

Battery Type	Lead acid	Ni-Cd	Ni-Mh	LiCoO ₂	LiMn ₂ O ₄	LiFePO ₄
Selling Price (\$)	1	2	2.4	4	6	8
Safety	Medium	Medium	Medium	Low	Low	High
Recyclability	Low	Low	High	High	High	High
Patent Protection	No	No	No	No	No	Yes
Memory Effect	No	Yes	Yes	No	No	No
Energy Density (Wh/L)	100	150	250	466	285	255
Power Density (W/kg)	300	855	800	320	400	2000
Round Trip Efficiency (%)	60	75	90	90	90	95
Life Cycle	400	500	500	>500	>500	>2000
Charging-up Time (hr)	8	1.5	4	2-4	2-4	<2
Application	Large Scale	Large Scale	Large Scale	Small Scale	Small & Large Scale	Large Scale

The advantages of Li-ion batteries include, but not limited to:

1. High working potential: for a single unit of Li-ion battery it can be as high 3.6V, which is almost 3 times of Ni/Cd and Ni/Mh batteries, and 2 times of lead-acid batteries;
2. High energy density: Li-ion batteries have the highest power density, which is 3 times of Ni/Mh batteries and 4 times of lead-acid batteries; their energy density can be higher than 400 Wh/L, and the volume is only 1/2 to 1/3 of lead-acid batteries with the same amount of energy;

3. Long cycle life: Li-ion batteries can be cycled by more than 1000 times, leading to a high cost performance;

4. Low self-discharge: the self-discharge rate of Li-ion batteries is as low as 10% in a month, which is obviously lower than those of Ni/Cd and Ni/Mh batteries;

5. No memory effect: unlike other batteries, Li-ion batteries do not have to be fully discharged before every charge, to the contrary, they can be charged at any time.

However, Li-ion batteries are not perfect. One major issue is the hidden danger of safety due to their high energy density and relatively poor material stability. In 2006, Sony recalled rechargeable Li-ion batteries containing Sony cells used in Fujitsu, Gateway, Sony, and Toshiba notebook computers, because there have been 16 reports of laptop batteries overheating, causing minor property damage and two minor burns, and all of these reported incidents and injuries have been associated with recalled Sony batteries [62]. In 2007, Nokia issued about 46 million units of its BL-5C cell phone battery (made by Panasonic) recall due to the risk of overheating [63]. A short circuit can occur which may pose an overheating risk upon charge. About 100 separate incidents have been reported by 2007, although there were no serious injuries or property damage. LG suddenly removed its Z1-AE007 from the market in February 2008 because of the blast caused by the malfunction of a battery manufactured by LG Chem. The explosion was strong enough to destroy the laptop. A succession of battery recall incidents not only caught a great public attention, but also brought down the operating profit to a lower level for manufacturers. For instance, the operating profit of Sony plunged 68.3% primarily resulted from the cost of huge battery recall in that year.

Japanese Industrial Standards Committee, Standards Board and Technical Committee on Electricity Technology jointly took action to develop new standards of safety tests for portable Li-ion secondary cells and batteries (JIS C8714), which began to take effect in November 2007 [64]. Even though an internal short circuit test was mandatory in this standard, this regulation has yielded little results due to the intrinsic unstable state of LiCoO_2 , LiMn_2O_4 cathode materials which have been used in over 90% commercial Li-ion batteries in the market.

In addition to safety concerns, high cost has also limited the popularization of Li-ion batteries, because they cost 2-3 times more than lead-acid batteries with the same potential and capacity.

1.6. Key Parameters to Evaluate Li-ion Batteries

Some key parameters including capacity, voltage and power density, which are directly determined by the kinetics of electron transfer reactions between two electrodes, are used to evaluate the performance of a battery. Capacity is determined by the amount of lithium entering and re-emerging into the crystal structure of the cathode [64]. Voltage, also called working potential is determined by the difference of chemical potentials between the cathode and anode. Voltage is related to reaction energy of the cathode material with lithium [64]. Power density is set by how fast lithium and electrons can be removed from or enter the cathode. Higher electron conductivity and ion conductivity of the electrode materials facilitate the electron transfer reaction by reducing internal resistance/impedance of the electrodes in Li-ion batteries. These parameters must be

taken into consideration when developing new electrode materials for Li-ion batteries in order to meet high performance target.

1.7. Cathode Structure and Electronic/Ionic Transport

In for a useful cathode material, lithium ions should be able to move along certain directions of the crystal structure, and at the same time it should also have high electronic conductivity as electron mobility must accompany lithium ion mobility [65]. Therefore, the achievable capacity of a cathode material is often determined by the rate limiting step, which could be set by either the electronic or ionic conductivity [66]. Poor electronic or ionic conductivity often results in a capacity fading during cycling, and this have been a sever issue especially for some cathode materials with low intrinsic ionic and electronic conductivity, such as LiMPO_4 and LiM_2SiO_4 (M=Fe, Mn, and Co).

One common approach to enhance the electronic/ionic transport is to reduce the crystal/partcile size of active materials. As theorized by Goodenough [67], in the case of LiFePO_4 , as the lithiation of FePO_4 proceeds, the surface area of the grain boundary decreases until a critical surface area is attained where the rate of lithium intercalation across the phase boundary is not able to sustain the current applied to the battery. This effect of decreased interface of active particles during lithiation may be minimized by producing an electrode material that contains small, homogeneously-sized crystallites, which would maximize the overall surface area and decrease the lithium path length in each grain, thus minimizing problems with lithium diffusion. Reducing the particle size of cathode material would reduce the path length that the lithium would have to transport

through a given crystallite to reach the electrolyte as well as reduce the path length of the electron hopping. Size reduction of the cathode material also has the benefit of increasing the surface area of the particles, which would also aid the lithium diffusion between the solid and the liquid electrolyte. In practice, decreasing the size of the electrode active particles has been found to increase the reversible capacity [68-70]. In addition, agglomeration of small particles into large clusters should also be prevented to optimize the total surface area of the electrode material.

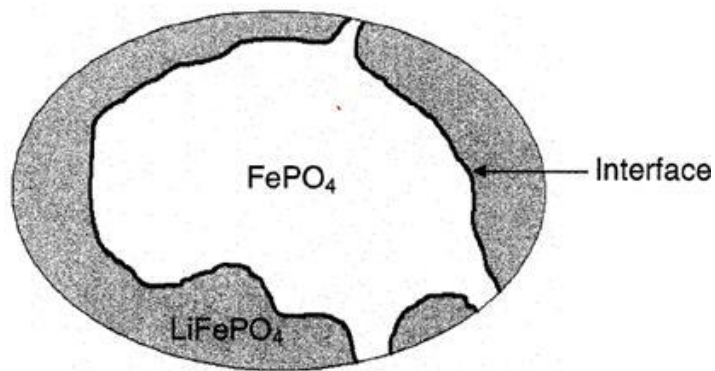


Figure 1-14. Decreasing surface area of a particle during lithiation [67].

Another approach is to add conductive additives in attempt to improve the overall electronic conductivity. The most researched method so far has been the use of carbon as an additive since carbon is inexpensive and the deposition of carbon during cathode material synthesis can be achieved easily. Carbon often behaves as a semi-conductor in an insulating matrix [71]. However, the electronic conductivity of carbon increases with the formation of more orderly-layered structure, such as graphite. This is because the

electronic conductivity of carbon is raised from the free electrons existing between the graphene lattices. Therefore, to maximize the electronic conductivity of cathode materials, carbon with a higher order structure is preferred.

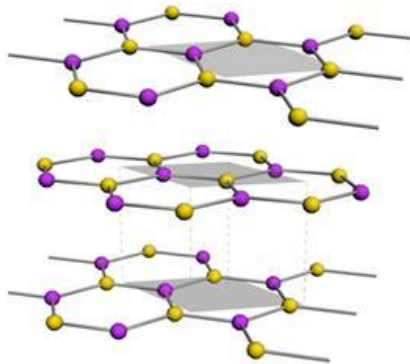


Figure 1-15. Graphic illustration of graphene hexagonal layers [72]

2. Overview of Electrospinning

2.1. Introduction

Electrospinning technology has been known for a long time. It is an old but yet immature process, which is now used to create nanoscale polymer fibers. The first discovery of electrical effects on liquids occurred more than three thousand years ago. In 1600 AD, William Gilbert observed that a spherical water droplet was pulled into a conical shape when a charged piece of amber was held above it.

In 1902, Morton received the first US patent for electrospinning artificial fibers [73]. In the 1930s and 1940s, Formhals claimed a series of patents on the process and apparatus to produce electrospun fibers [74-77]. In 1914, Zeleny presented one of the earliest

studies of electrified jetting phenomenon [78]. However, the practice of the electrospinning technology remained largely dormant until 1970s. Accordingly in electrospinning research, only a few publications appeared in the 1970s and 1980s, notably by Baumgarten and by Larrondo and St. John Manley [79, 80].

Little attention was given to the scientific aspect of electrospinning until Doshi and Reneker reintroduced this technique as a facile way to make submicron fibers [81]. Doshi made an effort to characterize the electrospinning process using aqueous polyethylene (PEO) solutions as the model fluid, and he proposed that the electric charges in the form of ions moved in response to the electric field and transferred the momentum to the polymer fluid.

The jet carried out the electric charge from polymer reservoir to the collector and thus completed the electric circuit. A decrease in jet diameter was attributed to the stretching of the jet and solvent evaporation. When the jet diameter became sufficiently small, radial forces raised by the electric charge became large enough to overcome the cohesion forces of the fiber, and this caused the jet to spray into many smaller fibers. This jet division occurred many times in rapid successions, and produced a large number of small charged fibers moving toward the collector. The divided jets repelled each other, thereby acquiring lateral velocities and chaotic trajectories. Charged fibers were collected on a ground metallic screen. The observed diameter ranged from 0.05 to 5 μm , and fibers possessed a wide variety of cross-sectional shapes, e.g. coils and beads. This process description was generally accepted and adopted in subsequent studies, such as Reneker

and Chun [81, 82].

2.2. General Experimental Description

For electrospinning to occur one needs a relatively simple set-up (Fig. 1-16). The components include a power source capable of forming large electric field (0.5 kV/cm), a counter electrode, a viscous solution, and a means of pumping the liquid. While a solution is forced out of the nozzle, either by gravity or external force, the immediate forces acting upon the liquid are gravity, surface tension, and electrical stresses. These forces compete and balance each other to form a Taylor cone. Depending on the status of equilibrium, the cone will eject droplets or a jet of liquid that travels to a grounded collector.

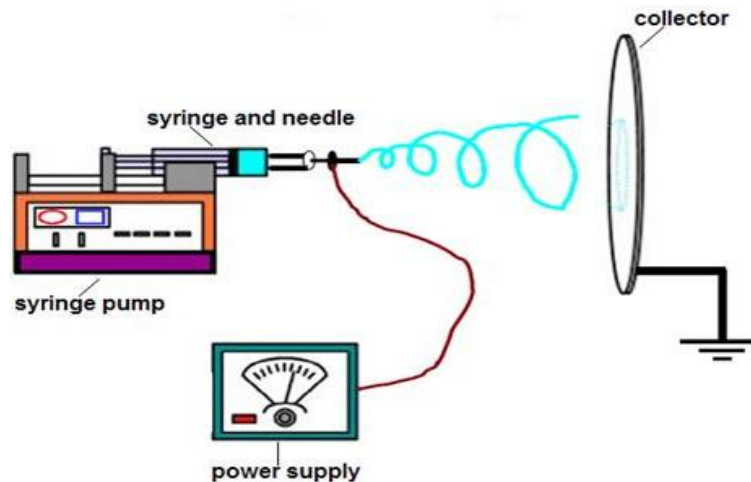


Figure 1-16. Electrospinning set-up.

Often in laboratory practice, the applied voltage and the flow rate are closely regulated.

In a more elaborated electrospinning device, a pumping device is used to deliver the fluid to the capillary. Usually, the fluid is fed through a non-conducting tube to the capillary to prevent unwanted electrical discharge to the pump. A typical voltage generator delivers 10 to 40 kilovolts at around 100 microamperes of direct current (DC). A typical distance between the nozzle and the collector is 10 centimeters or more. The fiber collector comes in myriad designs. The most basic one is an aluminum disk or plate connecting to a grounded wire. The more complicated designs may include a coagulating solvent bath or a conveyor belt.

The electrospinning process is characterized by four major regions: (1) the Taylor cone region, (2) the steady jet region, (3) the instability region, and (4) the base region. The jet initiates at the bottom of the Taylor cone and travels as a single jet decreasing in diameter toward the ground electrode. At some point the jet experiences instability from surface charge effects and nearly disappears to an untrained naked eye. At this point, the jet experiences what is commonly referred to as ‘whipping’ instability, where the jet is accelerated, stretched, and dried. The final region as described by Reneker [83] is the collection region. It is here that the jet and instability are stopped and the fibers are collected.

Table 2-1 illustrates the variables which should be taken into consideration while operating electrospinning in order to obtain nanofibers with consistency.

Table 2-1. Important factors affecting electrospinning.

Fluid Properties	Operating parameter	Process Variables
viscosity	flow rate	jet radius
conductivity	applied potential	axial velocity
dielectric constant	jet current	charge distribution

2.3. Electrospun Inorganic Fibers

Electrospinning is commonly used to prepare polymer nanofibers. Spinning inorganic materials directly into nano-sized fibers is difficult. However, electrospun polymeric nanofibrous mat can provide sturdy templates to create these hard-to-spin inorganic fibers. One method is to coat the electrospun mat with organic materials by chemical deposition. Caruso demonstrated the feasibility of this method by producing a mat of hollow titanium dioxide nanofibers [84]. A solution of poly(L-lactide) was electrospun into fibrous mat. Then the mat was dipped into a sol-gel of titanium salt. Once the mat was coated, thermal treatment burned off the poly(L-lactide), leaving behind a nonwoven mat of hollow titanium dioxide fibers.

Instead of coating the fiber mat after electrospinning, blending inorganic materials into a polymer solution before electrospinning is also possible. Shao et al. blended silica gel with poly(vinyl alcohol) and electrospun this mixture into a fiber mat [85]. The mat was then heat-treated bringing to final product of silica fiber mat. The silica fibers are quite porous, which generates a large surface area that can enhance the process efficiency

in applications like catalysis and diffusion. This method has also been employed by other researchers to obtain inorganic particle- loaded nanofiber [86, 87].

2.4. Producing Carbon Fibers from Polyacrylonitrile

Fine carbon fibers can be obtained by thermally treating electrospun polyacrylonitrile (PAN) nanofibers. In recent years, PAN as one of the most versatile polymers being considered as main precursor to produce carbon fibers. It possesses several advantages over some other popular carbon fiber precursors such as polyimide, of which the most outstanding advantages are high yield rate and low cost [88]. The molecular structure of PAN is shown in Fig. 1-17. The process of producing carbon fibers from PAN can be achieved by two steps including thermal stabilization and carbonization. In the first step, the fibrous PAN mat is heated to and kept at approximately 250-300 °C under oxygen or air. PAN is chemically modified in this step with a complex chemistry of stabilization. Generally, the nitrile groups are cyclized, and by dehydrogenation and oxidative rations, the backbone chains are crosslinked. The linear polymer is then transformed into ladder structure, which renders the polymer thermally stable and be able to survive the subsequent high temperature pyrolysis. The stabilization can also protect both the molecules and the fibrillar orientation from elimination during further heat treatment. Pyrolysis is carried out at the second step. The precursor is heated to a required pyrolysis temperature ranging from 700-900 °C in an inert atmosphere and maintained at that temperature for several hours. During this process, the non-carbon elements are eliminated in forms of hydrogen cyanide (HCN), ammonia (NH₃), nitrogen (N₂), and

carbon dioxide (CO₂), etc. Fig. 1-18 shows the proposed PAN-based carbon fiber formation mechanism of the stabilization chemistry and carbonization. The resulting fibers shrink in diameter, and the weight loss is around 50-60% of its original weight.

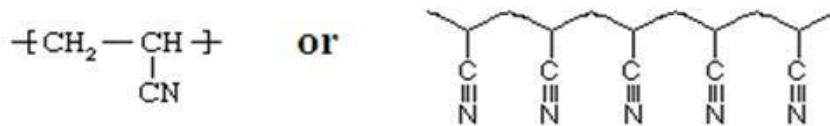


Figure 1-17. Molecular structure of PAN.

The yielded carbon can be directly used in this state, or it can undergo further heat treatment up to 3000 °C to form the graphitic structure [89]. Since the carbon fibers are conductive, in our research, the carbonized PAN nanofibers were prepared via electrospinning and were used as the cathode in Li-ion batteries.

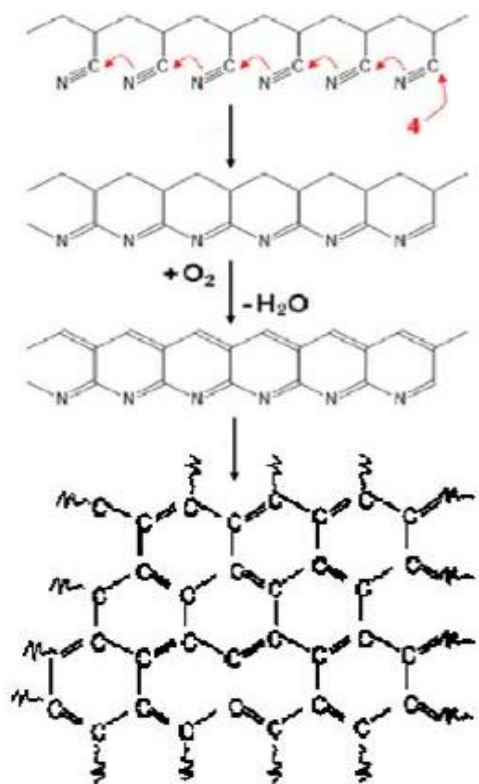


Figure 1-18. Stabilization of PAN under air at 250-300 °C and graphinization at 700-800 °C.

References

1. Winter, M.; Brodd, J. J. What are Batteries, Fuel Cells, and Supercapacitors? *Chemistry Review*, 2004, 104, 10-13.
2. Whittingham, M.S. Lithium Batteries and Cathode Materials, *Chemistry Review*, 2004, 10, 104-106.
3. <http://www.mpoweruk.com/performance.htm>
4. Peled, E.; Menichem, D.; Bar-Tow, D.; Melman, A. Improved Graphite Anode for Lithium-Ion Batteries Chemically, *J. Electrochem. Soc.*, 1996, 1 (143), L4-L7
5. Jung, H.G.; Myung, S.T.; Yoon, C.S.; Son, S.B.; Oh, K.H.; Amine, K.; Scrosati, B.; Sun, Y.K. Microscale Spherical Carbon-coated $\text{Li}_4\text{Ti}_5\text{O}_{12}$ as Ultra High Power Anode Material for Lithium Batteries, *Energy Environ. Sci.*, 2011, 4, 1345-1351.
6. Poizot, P.; Laruelle, S.; Grugeno, S.; Dupont, L.; Tarascon, J.M. Nano-sized Transition-metal Oxides as Negative Electrode Materials for Lithium- ion Batteries, *Nature*, 2000, 407, 496-499.
7. Magasinki, A.; Dixon, P.; Hertzberg, B.; Kvit, A.; Ayala, J.; Yushin. G. High-performance Lithium- ion Anodes Using A Hierarchical Bottom-up Approach, *Nature Materials*, 2010, 9, 353-358.
8. Idota, Y.; Kubota, T.; Matufuji, A.; Maekawa, Y.; Miyasaka, T. *Science*, 1997, 276 (5317), 1395-1397.
9. <http://en.wikipedia.org/wiki/Cathode>
10. Jo, M.; Jeong, S.; Cho, J. High Power LiCoO_2 Cathode Materials with Ultra Energy Density for Li- ion Cells, *Electrochemistry Communications*, 2010, 12, 992-995.

11. Wittingham, M.S. Lithium Battery and Cathode Materials, *Chemical Reviews*, 2004, 104, 4271-4301.
12. Wang, Y.; Cao, G. Developments in Nanostructured Cathode Materials for High-Performance Lithium-Ion Batteries, *Advanced Materials*, 2008, 20, 2251-2269.
13. Wang, D.; Buqa, M.; Crouzet, M.; Deghenghi, G.; etc. High-performance, Nanostructured LiMnPO_4 Synthesized via a Polyol Method, *Journal of power sources*, 2009, 189, 624-628.
14. Toprakci, O.; Zhang, X.W.; Fabrication and Electrochemical Characteristics of LiFePO_4 Powders for Lithium-Ion Batteries, *KONA Powder and Particle Journal*, 2010, 28, 50-73.
15. Manthiram, V. A.; Sarkar, A.; Muraliganth, T. Nanostructured Electrode Materials for Electrochemical Energy Storage and Conversion, *Energy & Environmental Science*, 2008, 1, 621-638.
16. Honoson, E.; Wang, Y. G.; Kida, N.; Enomoto, M.; Kojima, N. H. Synthesis of Triaxial LiFePO_4 Nanowire with a VGCF Core Column and a Carbon Shell through the Electrospinning Method, *ACS Applied Materials and Interfaces*, 2010, 2 (1), 212-218.
17. Xu, J.; Chen, G.; Li, X. Electrochemical Performance of LiFePO_4 Cathode Material Coated with Multi-Wall Carbon Nanotubes, *Materials Chemistry and Physics*, 2009, 118, 9-11.
18. Thackeray, M.M.; David, W.I.F.; Bruce, P.G.; Goodenough, J.B. Lithium Insertion into Manganese Spinels, *Mater. Res. Bull.*, 1983, 18, 461.

19. Yang, S.; Song, Y.; Zavalij, P.Y.; Whittingham, M.S. *Electrochemistry Communications* 4, 2002, 239.
20. Toprakci, O.; Ji, L.; Lin, Z.; Toprakci, H.A.K; Zhang, X. *Fabrication and Electrochemical Characteristics of Electrospun LiFePO₄/carbon Composite Fibers for Lithium-ion Batteries*, *Journal of Power Sources*, 2011, 196(18), 7692-7699.
21. Nyten, A.; Abouimrane, A.; Armand, M.; Gustafsson, T.; Thomas, J.O. *Electrochemical Performance of Li₂FeSiO₄ as a New Li-battery Cathode Material*, *Mater. Chem.*, 2005, 7, 156-160.
22. Nyten, A.; Kamali, S.; Hangstrom, L.; Gustafsson, T.; Thomas, J.O. *the Lithium Extraction/insertion Mechanism in Li₂FeSiO₄*, *Mater. Chem.*, 2006, 2266-2272.
23. Dominko, R.; Bele, M.; Kokalj, A.; Gaberscek, M.; Jamnik, J. *Journal of Power Sources* 174, 2007, 457.
24. Dominko, R. *Li₂MnSiO₄ Cathode Materials*, *Journal of Power Sources*, 2008, 184, 462-468
25. Li, Y.; Gong, Z.; Yang, Y. *Journal of Power Sources* 2007, 174, 528-532.
26. Kokalj, A.; Dominko, R.; Mali, G.; Meden, A.; Gaberscek, M.; Jamnik, J. *Beyond One-Electron Reaction in Li Cathode Materials: Designing Li₂MnxFe_(1-x)SiO₄*, *Chem. Mater.*, 2007, 19, 3633-3640.
27. Dharmaraj, N.; Park, H.C.; Kim, C.K.; Kim, Y.K.; Lee, D.R. *Nickel Titanate Nanofibers by Electrospinning*, *Mater. Chem. Phys.*, 2004, 87, 5-9.
28. Badway, F.; Pereira, N.; Cosandey, F.; Amatucci, G.G. *Solid State Ionics*, 2002, 756, 207.

29. Badway, F.; Cosandey, F.; Pereira, N.; Amatucci, G.G. *Journal of the Electrochemical Society*, 2003, 150(10), A1318.
30. Arai, H.; Okada, S.; Sakurai, Y.; Yamaki, J. *Journal of Power Sources*, 1997, 68, 716.
31. Lascaud, M.; Lachter, A.; Salarfenne, J.; Barriere, A.S. *Thin Solid Films*, 1979, 59, 353.
32. Badway, F.; Pereira, N.; Cosandey, F., Amatucci, G.G. *Journal of Electrochemical Society*, 2003, 150, 1209.
33. Maier, J. *Solid State Ionics*, 2002, 148, 367.
34. Liao, P.; Dunlap, R.A.; Dahn, J.R. *Journal of Physics: Condensed Matter*, 2008, 20, 55203.
35. Makimura, Y.; Rougier, A.; Laffont, L.; Womes, M.; Jumas, J.C.; Leriche, J.B.; Tarascon, J.M. *Electrochemistry Communications*, 2006, 8, 1769.
36. Zhou, Y.; Liu, W.; Xue, M.; Yu, L.; Wu, C.; Wu, X.; Fu, Z. *Electrochemical and Solid-State Letters*, 2006, 9(3), A147.
37. Ochi, M.; Kita, E.; Saegusa, N.; Erata, T.; Tasaki, A. *Journal of Physical Society*, 1992, 61, 35.
38. Kita, E.; Ochi, M.; Erata, T.; Tasaki, A. *Journal of Magnetism and Magnetic Materials*, 1992, 117, 294.
39. Spence, J.C.H. *High-Resolution Electron Microscopy*, Oxford University Press, 3rd Ed., 2003.
40. Lee, S.W.; Yabuuchi, N.; Gallant, B.M.; Chen, S.; Kim, B.; Hammond, P.T.; Yang,

- S.H. High-Power Lithium Batteries from Functionalized Carbon-Nanotube Electrodes, *Nature Nanotechnology*, 2010, 5, 531-537.
41. Sun, Y.K.; Myung, S.T. High-energy Cathode Material for Long- life and Safe Lithium Batteries, *Nature Materials*, 2009, 8, 320-324.
42. Oh, S.S.; Oh, S.W.; Yoon, C.S.; Scrosati, B.; Amine, K.; Sun, Y.K. High-Performance Carbon-LiMnPO₄ Nanocomposite Cathode for Lithium Batteries, *Advanced Functional Materials*, 2010, 20(19), 3260-3265.
43. Reddy, M.V.; Subba, G.V.; Chowdari, B.V.R. Long-term Cycling Studies on 4 V-Cathode, Lithium Vanadium Fluorophosphate, *Journal of Power Sources*, 2010, 195, 5768-5774.
44. Wang, D.Y.; Xiao, J.; Xu, W.; Nie, Z.; Wang, C.; Graff, G.; Zhang, J.G. Preparation and Electrochemical Investigation of Li₂CoPO₄F Cathode Material for Lithium-Ion Batteries, *Journal of Power Sources*, 2010, 21-38.
45. Ren, M.M.; Zhou, Z.; Gao, X.P.; Peng, W.X.; Wei, J.P. Core-Shell Li₃V₂(PO₄)₃/C Composites as Cathode Materials for Lithium- Ion Batteries, *J. Phys. Chem. C*, 2008, 112, 5689-5693.
46. Wang, L.; Zhao, J.; Guo, S.H.; He, X.; Jiang, C.; Wan, C. Investigation of SnO₂ modified LiMn₂O₄ Composite as Cathode Material for Lithium- ion Batteries, *Int. J. Electrochem. Sci.*, 2010, 5, 1113-1126.
47. Johnson, C.S.; Kang, S.H.; Vaughey, J. T.; Pol, S.V.; Balasubramanian, M.; Thackeray, M.M. Li₂O Removal from Li₃FeO₄: A Cathode Precursor for Lithium-Ion Batteries, *Chem. Mater.*, 2010, 22, 1263-1270.

48. Kuganathan, N.; Islam, M.S.; Li₂MnSiO₄ Lithium Battery Material: Atomic-Scale Study of Defects, Lithium Mobility, and Trivalent Dopants, *Chem. Mater.*, 2009, 21(21), 5196-5202.
49. Makino, Y.; Kusagaya, T.; Suzuki, K.; Endou, A.; Kubo, M.; Selvam, P.; Ota, H.; Yonekawa, F.; Yamazaki, N.; Miyamoto, A. Electronic Structure of the Electrode/electrolyte Interface: Large-scale Tight-binding Quantum Chemical Simulation, *Solid State Ionics*, 2004, 175, 847-850.
50. Rajendran, S.; Uma, T. Experimental investigations on PVC-LiAsF₆-DBP polymer electrolyte systems, *Journal of Power Source*, 2000, 87, 218-222.
51. Rajendran, S.; Song, M.S.; Park, M.S.; Kim, J.H.; Lee, J.Y. Lithium Ion Conduction in PVC-LiN(CF₃SO₂)₂ Electrolytes Gelled with PVdF, *Material Letters*, 2005, 59(18), 2347-2351.
52. Wang, S.; Qiu, W.; Li, T.; Yu, B.; Zhao, H. Properties of Lithium bis(oxalato)borate (LiBOB) as a Lithium Salt and Cycle Performance in LiMn₂O₄ Half Cell, *Int. J. Electrochem. Sci.*, 2006, (1), 250-257.
53. <http://www.celgard.com/monolayer-pp.aspx>
54. Ceder, G. Opportunities and Challenges for First-principles Materials Design and Applications to Li Battery Materials, *MRS Bulletin*, 2010, 35, 693-701.
55. http://www.snupeel.com/wp/wp-content/uploads/2009/01/03_secondary1.jpg
56. Pavlov, D. *Lead-acid Batteries: Science and Technology : a Handbook of Lead-acid Battery Technology and Its influence on the Product*, Elsevier Science Ltd., 2011.

57. Reid, M.A. Changes in Impedances of Ni/Cd Cells with Voltage and Cycle Life, *Electrochimica Acta*, 1993, 38(14), 2037-2041.
58. Milocco, R.H.; Castro, B.E. State of Charge Estimation in Ni-MH Rechargeable Batteries, *Journal of Power Sources*, 2009, 194(1), 558-567.
59. Cuscueta, D.J.; Ghllarducci, A.A.; Salva, H.R. Design, Elaboration and Characterization of a Ni-MH Battery Prototype, *International Journal of Hydrogen Energy*, 2010, 35(20), 11315-11323.
60. Molenda, J. Transport Properties of Li_2MnO_4 , *Solid State Ionics*, 1999, 117, 41-46.
61. Wolfenstine, J. Charge Compensation in LiCoO_2 , *Journal of Power Sources*, 2004, 129(2), 324-325.
62. <http://www.cpsc.gov/cpsc/pub/prerel/prhtml07/07011.html>
63. <http://www.betanews.com/article/Nokia-Issues-Massive-Phone-Battery-Recall/1187100296>
64. Japanese Standards Association, JISC 8714, 2007
65. Koudriachova, M.V.; Harrison, N.M.; de Leeuw, S.W. *Solid State Ionics*, 2003, 157, 35-38.
66. Chung, S.Y.; Bloking, J.T.; Chiang, Y.M. *Nature Materials* 2002, 1(2), 123-128.
67. Pahdi, A.K.; Nanjundaswamy, K.S.; Goodenough, J.B. *Journal of Electrochemical Society* 1997, 144, 1188.
68. Pistoia, G.; Pasquali, M.; Geronov, Y.; Manev, V.; Moshtev, R.V. *Journal of Power Sources* 1989, 27(1), 35-43.

69. Kawamura, T.; Makidera, M.; Okada, S.; Koga, K.; Miura, N.; Yamaki, J.C Journal of Power Sources 2005, 146, 27-32.
70. Talyosef, Y.; Markovsky, B.; Lavi, R.; Salitra, G.; Aurbach, D.; Kovacheva, D.; Gorova, M.; Zhecheva, E.; Stoyanova R. J. Electrochem. Soc. 2007, 154(7), A682-691.
71. Yamada, A.; Chung, S.C.; Hinokuma, K.J. Electrochem. Soc. 2001, 148,3, A224-229.
72. Godfrey, G.; Huang, D.; Phil. Trans. R. Soc. 368,2010, 1932, 5353-5354.
73. Morton W. J.. Methods of Dispersing Fluids, US Patent, 705,691
74. Formhals A.. Processing and Apparatus for Preparing Artificial Threads, US Patent, 1934, 2,077,373.
75. Formhals A.. Method of Producing Artificial Fibers, US Patent, 1939, 2,158,415.
76. Formhals A.. Production of artificial fibers from fiber forming liquids, US Patent, 1943, 2,323,025.
77. Formhals A.. Method and apparatus for Spinning, US Patent, 1944, 2,349,950.
78. Zeleny J.. The electrical Discharge from Liquid Points, and a Hydrostatic Method of Measuring Electric Intensity at Their Surfaces, Physical Reviews, 1914, 3, 69-91.
79. Baumgarten P.. Electrostatic Spinning of Acrylic Microfibers, Journal of Colloid and Interface Science, 1971, 36, 71-79.
80. Larrondo L., Manley R. S. Electrostatics Fiber Spinning from Polymer Melts, Polymer Science: Part B: Polymer Physics, 1981, 19, 909-920.
81. Doshi J., Reneker D. H.. Electrospinning Process and Applications of Electrospun Fibers, Journal of Electrostatics. 1995, 35, 151-160.

83. Deitzel, J. M., Kleinmeyer J. D., Hirvonen J. K., Tan N. B. Controlled Deposition of Electrospun Poly(ethylene oxide) Fibers. *Polymer*, 2001; 42, 8163-8170.
84. Telemeco T. A., Ayres C., Bowlin G. L. Regulation of Cellular Infiltration into Tissue Engineering Scaffolds Composed of Submicron Diameter Fibrils Produced by Electrospinning, *Acta Biomater*, 2005, 1, 377-385.
85. Kataphinan W., Reneker D. H., Teye-Mensah R., Evans E. A., Ramiser R., Smith D. J. Electrospinning Titanium Alkoxide Precursor with Rare Earth Compounds, *Abstracts of Papers of the American Chemical Society*. 2003, 226, U402.
86. Li, D.; Yun X. Fabrication of Titania Nanofibers by Electrospinning, *Nano Letters*, 2003, 3(4), 555-560.
87. Shao, C.; Kim, H.; Gong, J.; Lee D. A Novel Method for Making Silica Nanofibers by Using Electrospun Fiber of Polyvinylalcohol/silica Composite as Precursor, *Nanotechnology*, 2002, 13, 635-637.
88. Saufi, S.M.; Ismail, A.F. Development and Characterization of Polyacrylonitrile (PAN) Based Carbon Hollow Fiber Membrane, *Songklanakarin J. Sci. Technol.*, 2002, 24, 843-854.
89. Pierson H.O. *Handbook of Carbon, Graphite, Diamond, and Fullerenes: Properties, Processing and Applications*, Noyes publications, 1993.

Chapter 2 Research Objectives

The objective of this work is to explore and improve new cathode materials for high-performance rechargeable Li-ion batteries. Our main research work includes:

(I). Fabrication of $\text{Li}_2\text{MnSiO}_4$ /carbon composite nanofibers through electrospinning and heat treatment and their applications as cathode materials for Li-ion batteries

Although $\text{Li}_2\text{MnSiO}_4$ has a theoretical capacity of 332 mAh/g, a large number of studies can realize only around 100 mAh/g even at low charge/discharge rate of C/50. The low practical conductivity of $\text{Li}_2\text{MnSiO}_4$ is mainly attributed to the extremely low intrinsic conductivity of this material. In an effort to minimize this problem, particle-size reduction and carbon coating are proved to be very efficient in the case of another poorly conducting material, LiFePO_4 [1]. The particle size is critical and controlling the particle size is essential because the smaller particle size can aid to realize a better electrochemical utilization of the active materials. Furthermore, the reduction of particle size can lead to a larger specific surface area which allows more contact of cathode material with the electrolyte, which will also benefit the high rate capacity.

As a newly developed cathode material, although $\text{Li}_2\text{MnSiO}_4$ gained tremendous interest and active research has been conducted to improve the performance of $\text{Li}_2\text{MnSiO}_4$, there is only a few paper reported producing and controlling $\text{Li}_2\text{MnSiO}_4$ in a submicron scale. Yang and his group created a $\text{Li}_2\text{MnSiO}_4/\text{C}$ nanocomposite via so-gel method and it reached reversible more than one electron reaction at first two cycles for the first time [2].

However, a rapid decrease in capacity was observed after first three cycles. As a result, the technological impact of investigating process-structure relationship of carbon nanofibers and active $\text{Li}_2\text{MnSiO}_4$ material would be significant and needs further exploration.

By networking $\text{Li}_2\text{MnSiO}_4$ particles with carbon nanofibers, not only the particle size can be maintained in nanoscale, but also the electronic conductivity can be enhanced. This is due to the combined effect of the reduced lithium diffusion pathway and the electronically conductive matrix provided by carbon nanofibrous mat. In our research, the carbon nanofiber matrix is produced from electrospun PAN precursor mat. The electrospinning involves inorganic particles of premade $\text{Li}_2\text{MnSiO}_4$ and PAN mixture solution. Benefiting from the good mechanical property of PAN based carbon nanofibers, the active particles can be embedded and coated by the continuous carbon nanofiber matrix. The resultant $\text{Li}_2\text{MnSiO}_4$ /carbon composite nanofibers can be directly used as the cathode without the need of additional binders or conducting agents. This process is illustrated in Fig. 2-1 as a combined method of electrospinning and heat-treatment.

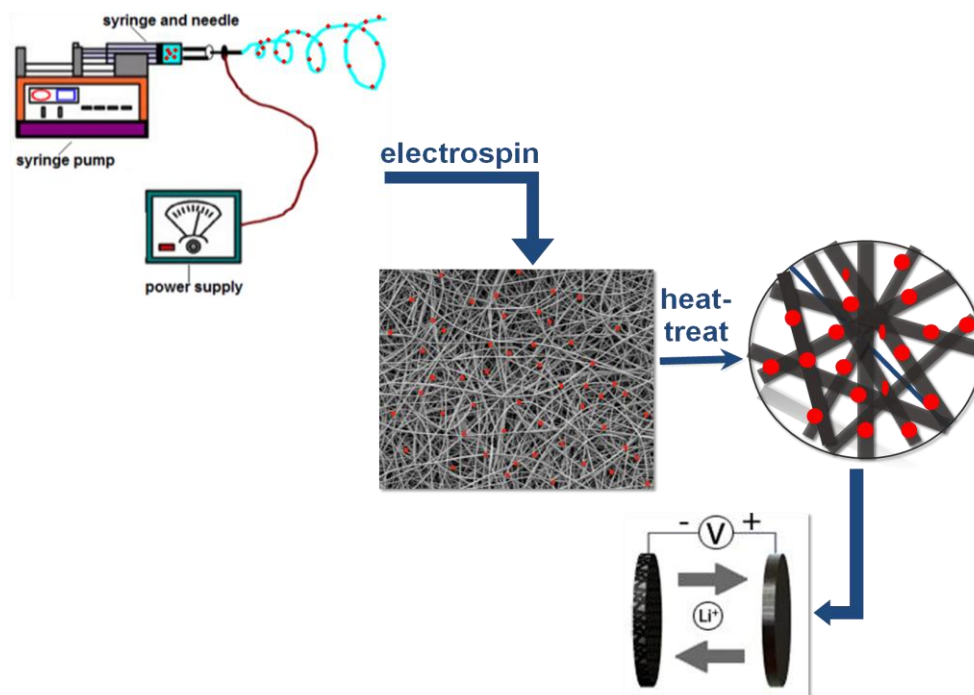


Figure 2-1. Samples prepared from electrospinning followed by heat-treatment can be directly used in Li-ion batteries.

(II). Realizing beyond one-electron reaction by designing $\text{Li}_2\text{Mn}_x\text{M}_{(1-x)}\text{SiO}_4$ (M= Fe and Cr) /carbon composite nanofibers and their applications as cathode materials for Li-ion batteries

In addition to enhancing the electronic conductivity by carbon coating, another strategy is bivalent cation (such as Ni, Fe, and Cr) doping to increase electronic and lithium ionic mobility, diffusion coefficient, and crystal structure modification as well. There are two approaches employed in our study, *i.e.*, iron doping and chromium doping.

For the first approach, as reported by Kokaj et.al, $\text{Li}_2\text{MnSiO}_4$ suffers from extremely low conductivity, which is about 2 orders of magnitude lower than for $\text{Li}_2\text{FeSiO}_4$ at a given

temperature [3] as shown in Fig. 2-2. The iron doping of $\text{Li}_2\text{MnSiO}_4$ and carbon coating can be simultaneously achieved by blending and electrospinning doped $\text{Li}_2\text{MnSiO}_4$ and PAN precursor, followed by a heat treatment. A pronounced advantage of combined method of electrospinning and heat-treatment is additive free. In conventional preparation of cathode materials, polymer binders such as polyvinylidene fluoride and polytetrafluoroethylene are added to bind active particles together. However, these binders may also act as obstacles between active materials and electrolyte resulting in slow reaction kinetics and reduction in effective electrode-electrolyte interface area. This combined method combines the advantage of conductivity improvement and elimination of non-active materials in the cathode, therefore, an improved overall electrochemical performance is possible for $\text{Li}_2\text{Mn}_x\text{M}_{(1-x)}\text{SiO}_4$ /carbon composite nanofibers as cathode material in Li-ion batteries.

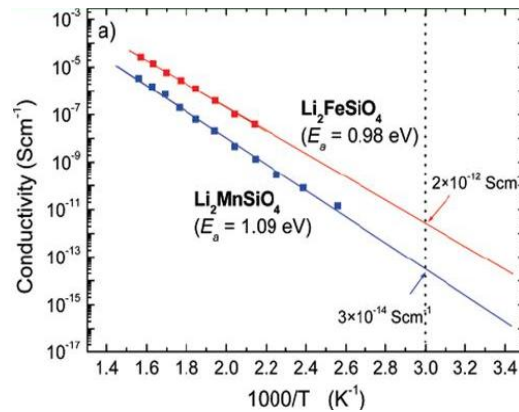


Figure 2-2. Electronic characterizations of $\text{Li}_2\text{MnSiO}_4$ and $\text{Li}_2\text{FeSiO}_4$ [2].

Beside the problem of low conductivity of $\text{Li}_2\text{MnSiO}_4$, Kokaj's group also proposed a

failing mechanism of $\text{Li}_2\text{MnSiO}_4$ cathode material- crystal structure collapse upon the removal of large amount of Li [3]. In a research of chromium doping of $\text{Li}_2\text{FeSiO}_4$ conducted by Zhang et. al., a positive effect of Cr doping was found by inducing defects in the lattice of $\text{Li}_2\text{FeSiO}_4$. Similar job was done for LiMn_2O_4 , a ZnO doped sample presented a more stable structure than undoped LiMn_2O_4 . It was believed that Zn^{2+} could act as a pillar to prevent the collapse of the crystal during cycling, as with doping by hetero-atoms in LiMn_2O_4 . In our case, chromium is investigated into its effect on crystal structure of $\text{Li}_2\text{MnSiO}_4$ during charge and discharge. To get further understanding, three different doping ratios are prepared as $\text{Li}_2\text{Mn}_{0.97}\text{Cr}_{0.03}\text{SiO}_4$, $\text{Li}_2\text{Mn}_{0.94}\text{Cr}_{0.06}\text{SiO}_4$, and $\text{Li}_2\text{Mn}_{0.9}\text{Cr}_{0.1}\text{SiO}_4$, respectively.

(III). Preparation and characterization of LiF/Fe/carbon composite nanofibers as cathode materials for Li-ion batteries

As discussed previously, material size reduction is essential to achieve better cathode performance. Carbon nanofibers have attracted tremendous interest because it has large surface area and disordered carbon matrix over which lithium diffusion and charge transfer could occur [4-6]. There are several advantages that carbon nanofibers possess. Firstly, due to the reduced diffusion length for lithium ions and electron transport within the particles, the carbon nanofibers can increase the rates of lithium insertion and extraction [7]. The high surface-to-volume ratio of carbon nanofibers allows more contact between the electrode and electrolyte. Finally, by dispersing active cathode particles into the carbon nanofiber matrix can effectively prevent accumulation of primary particles to

form large agglomeration [8].

To obtain a highly tailored structure of active particles well dispersed in the carbon nanofiber matrix, electrospinning will be used to fabricate metallic iron/LiF/carbon nanofibers with controllable structures. Metallic iron is oxidized to FeF_3 during charging while lithium ions are extracted from the cathode. During discharge, FeF_3 is reduced back to LiF/Fe composite.

It is critical to form a heterogeneous mixture of LiF and Fe at nanoscale. Electrospinning makes it possible by spinning LiF and the precursors of Fe in nanoscale. Ferrocene will be used as the precursor for metallic iron as Fe can be produced from ferrocene decomposition through thermal treatment. Ferrocene itself is also widely used as the catalyst to produce carbon nanotubes. Polyacrylonitrile as one of the most important precursors for carbon fibers can form a conductive carbon matrix after carbonization under the same thermal treatment conditions as ferrocene. Therefore, the metallic iron and carbon nanofiber formation can be synchronized in the heat-treatment step, which leads to a better contact between different components in the cathode. A mixture of ferrocene, LiF and PAN solution will be electrospun into nanofibers. The fibrous mat will be thermally treated in the furnace at a high temperature, and the resultant LiF/Fe/carbon nanofibers will be used as the cathode material.

References

1. Kokalj, A.; Dominko, R.; Mali, G.; Meden, A.; Gaberscek, M.; Jamnik, J. Beyond One-Electron Reaction in Li Cathode Materials: Designing $\text{Li}_2\text{Mn}_x\text{Fe}_{(1-x)}\text{SiO}_4$, *Chem. Mater.*, 2007, 19, 3633-3640
2. Dominko, R.; Bele, M.; Kokalj, A.; Gaberscek, M.; Jamnik, J. $\text{Li}_2\text{MnSiO}_4$ as a Potential Li-battery Cathode Material, *Journal of Power Sources*, 2007, 174, 457-461.
3. Dominko, R.; Bele, M.; Gaberscek, M.; Meden, A.; Remskar, M.; Jamnik, J. Structure and Electrochemical Performance of $\text{Li}_2\text{MnSiO}_4$ and $\text{Li}_2\text{FeSiO}_4$ as Potential Li-battery Cathode Materials, *Electrochemistry Communications*, 2006, 8, 217-222.
4. Chung, S.Y.; Bloking, Y.M.; Chiang, Y.M. Electronically Conductive Phospho-olivines as Lithium Storage Electrodes, *Nature Materials*, 2002, 1, 123-128.
5. Yheng-Wen, F.; Ma, J.; Zong, Q. LiMn_2O_4 Fibers Fabricated by a High Frequency Electrospinning, *Solid State Ionics*, 2005, 176, 1635-1640.
6. Kim, C.; Jeong, Y.I.; Ngoc, B.T.; Yang, K.S.; Kojima, M.; Kim, Y.A. Synthesis and Characterization of Porous Carbon Nanofibers with Hollow Cores through the Thermal Treatment of Electrospun Copolymeric Nanofiber Webs, *Small*, 2007, 3(1), 91-95.
7. Zhong, G.; Li, Y.; Yan, P.; Liu, Z.; Xie, M.; Lin, H. Structural, Electronic, and Electrochemical Properties of Cathode Materials Li_2MSiO_4 (M=Mn, Fe, and Co): Density Functional Calculations, *J. Phys. Chem. C*, 2010, 114, 2693-3700.
8. Dompablo, M.E.; Amador, U.; Gallardo-Amores, J.M.; Moran, E.; Eharenberg, H.; Dupont, L.; Dominko, R. Polymorphs of Li_3PO_4 and Li_2MSiO_4 (M=Mn, Co) the Role of Pressure, *Journal of Power Sources*, 2009, 189, 638-642.

Chapter 3 Fabrication of $\text{Li}_2\text{MnSiO}_4$ /Carbon Composite Nanofibers as High-Capacity Cathode Materials for Li-ion Batteries

$\text{Li}_2\text{MnSiO}_4$ /carbon composite nanofibers were prepared by a combination of electrospinning and heat treatment. $\text{Li}_2\text{MnSiO}_4$ particles were embedded in one-dimensional precursor nanofibers during electrospinning. After heat treatment, a carbon nanofiber network formed and acted as a conducting matrix to enhance the electronic conductivity and facilitate lithium ion transportation. $\text{Li}_2\text{MnSiO}_4$ /carbon nanofibers were directly used as the cathode material for Li-ion batteries, and they delivered a discharge capacity of greater than 180 mAh/g at the second cycle, indicating more than one electron exchange per transitional metal. The capacity retention of $\text{Li}_2\text{MnSiO}_4$ /carbon nanofibers was 54% at 20th cycle.

1. Introduction

The expanding demand for large-scale commercialization of Li-ion batteries with high energy and power densities has motivated active research on electrode materials with better performance and higher capacity. Goodenough's [1] discovery of LiFePO_4 as cathode materials has changed the landscape of Li-ion batteries due to its high stability and reliable safety. However, LiFePO_4 can only provide one lithium ion per formula unit, and hence its theoretical capacity is only 167 mAh/g [2,3]. Nyten [4, 5] firstly synthesized and characterized $\text{Li}_2\text{FeSiO}_4$, which not only has the same benefits as LiFePO_4 , but also can theoretically extract two lithium ions per formula unit from the

structure. The extraction of two lithium ions leads to a high theoretical capacity of 320 mAh/g for $\text{Li}_2\text{FeSiO}_4$. However, electrochemical tests only realized up to 1 lithium extraction per transitional metal in practice due to the poor conductivity and slow kinetics [4-6]. Dominko [6] then proposed the substitution of Fe with Mn. It was anticipated that with two redox pairs of Mn(II)/Mn(III) and Mn(III)/Mn(IV), two-electron reaction could become possible, corresponding to a high theoretical capacity of 332 mAh/g. However, they only achieved 0.7 lithium ion per formula unit during charge/discharge.

Extensive research on many cathode materials suggested that size reduction and conducting phase embedding could overcome the kinetic problem. We herein report a novel approach to prepare $\text{Li}_2\text{MnSiO}_4$ /carbon nanofibers by electrospinning and heat treatment. During electrospinning, the synthesized $\text{Li}_2\text{MnSiO}_4$ particles were embedded into polymer nanofibrous matrix. The heat treatment step converted the polymer into a conductive carbon matrix to provide enhanced electron and ion diffusions. The prepared $\text{Li}_2\text{MnSiO}_4$ /carbon nanofibers show improved capacity and reversibility.

2. Materials and method

The starting materials for $\text{Li}_2\text{MnSiO}_4$ were lithium acetate dihydrate, manganese acetate, and SiO_2 . After drying, the mixture was calcined in a furnace under Argon. The obtained sample was ground into fine $\text{Li}_2\text{MnSiO}_4$ powder. Then 30 wt% of $\text{Li}_2\text{MnSiO}_4$ powder was added into a 8 wt% polyacrylonitrile (PAN) solution. The dispersion was drawn into a syringe and secured in a syringe pump with a flow rate of 1 mL/hour. The electrospinning of nanofibers was carried out with a voltage of 18 kV and a needle tip-to-

collector distance of 15 cm. The electrospun $\text{Li}_2\text{MnSiO}_4/\text{PAN}$ composite nanofibers were first stabilized under air, following by carbonization under argon. The resultant $\text{Li}_2\text{MnSiO}_4/\text{carbon}$ composite nanofibers were then used as the cathode material for Li-ion batteries.

Scanning electron microscope (SEM, JEOL 6400F FESEM), field emission electron microscope (FETEM, Hitachi HF2000), and X-ray diffraction (Rigaku SmartLab) were performed to identify the structural variations of both $\text{Li}_2\text{MnSiO}_4$ powder and $\text{Li}_2\text{MnSiO}_4/\text{carbon}$ nanofibers.

Li sheet was used as the counter electrode, and polypropylene (PP) film (Celgard 2400) as the separator. The electrolyte used was 1 M solution of LiPF_6 in a mixture of ethylene carbonate (EC), dimethyl carbonate (DMC) and diethyl carbonate (DEC). The galvanostatic charge/discharge characteristics of the cells were recorded with a LAND battery testing system in the voltage range of 2.0 - 5.0 V (versus Li/Li^+) at room temperature.

3. Results and Discussion

Fig. 3-1 shows SEM images of the $\text{Li}_2\text{MnSiO}_4$ powder. The synthesized $\text{Li}_2\text{MnSiO}_4$ powder consists of agglomerated nanoparticles with primary particle size in the range of 30 - 50 nm.

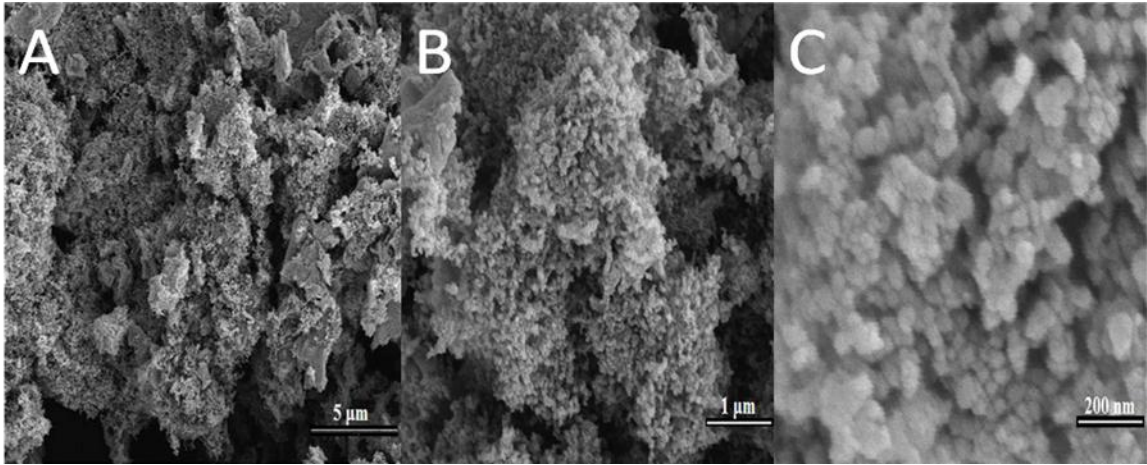


Figure 3-1. SEM images of $\text{Li}_2\text{MnSiO}_4$ particle at different magnifications.

Fig. 3-2A-C shows SEM images of $\text{Li}_2\text{MnSiO}_4/\text{PAN}$ precursor nanofibers. Electrospun $\text{Li}_2\text{MnSiO}_4/\text{PAN}$ nanofibers exhibit a rough fiber surface due to the presence of $\text{Li}_2\text{MnSiO}_4$ particles. The diameter of $\text{Li}_2\text{MnSiO}_4/\text{PAN}$ nanofibers is in the range of 250 - 360 nm. SEM images of $\text{Li}_2\text{MnSiO}_4/\text{carbon}$ composite nanofibers are presented in Fig. 2D and E. After heat treatment, substantial volume contraction and fiber diameter reduction were observed due to the removal of some species during the heat treatment process.

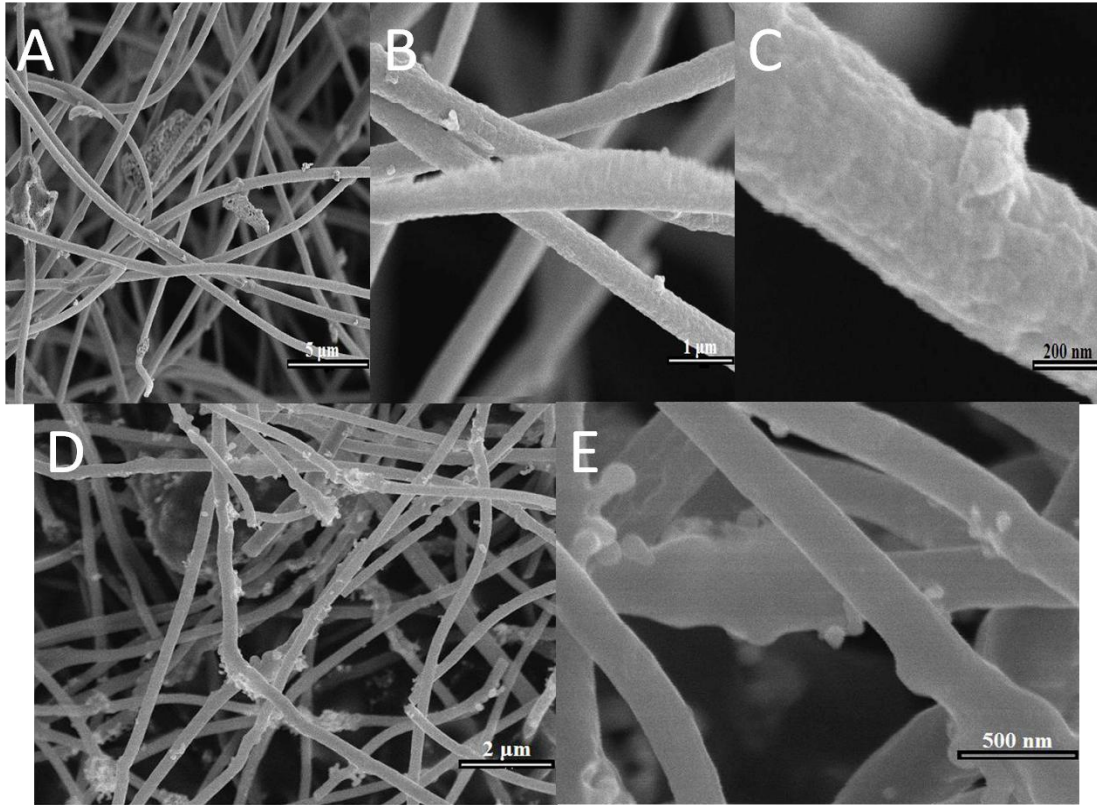


Figure 3-2. SEM images of electrospun $\text{Li}_2\text{MnSiO}_4/\text{PAN}$ nanofibers (A, B, and C) and $\text{Li}_2\text{MnSiO}_4/\text{carbon}$ nanofibers (D and E) at different magnifications.

Fig. 3-3 shows a TEM image of a $\text{Li}_2\text{MnSiO}_4/\text{carbon}$ composite nanofiber. It is seen that the $\text{Li}_2\text{MnSiO}_4$ particles are dispersed in the carbon nanofiber matrix. The XRD patterns of $\text{Li}_2\text{MnSiO}_4$ powder and $\text{Li}_2\text{MnSiO}_4/\text{carbon}$ nanofibers are shown in Fig. 3-4. For both $\text{Li}_2\text{MnSiO}_4$ powder and $\text{Li}_2\text{MnSiO}_4/\text{carbon}$ nanofibers, $\text{Li}_2\text{MnSiO}_4$ exists in the form of a stoichiometric orthorhombic structure [7]. The signal of MnO was also detected at around $2\theta = 41^\circ$ for both samples, which is considered as an impurity for $\text{Li}_2\text{MnSiO}_4$. The XRD pattern of $\text{Li}_2\text{MnSiO}_4/\text{carbon}$ nanofibers appears to be identical to that of $\text{Li}_2\text{MnSiO}_4$

powder, indicating that the heat treatment did not change the structure of the active material.

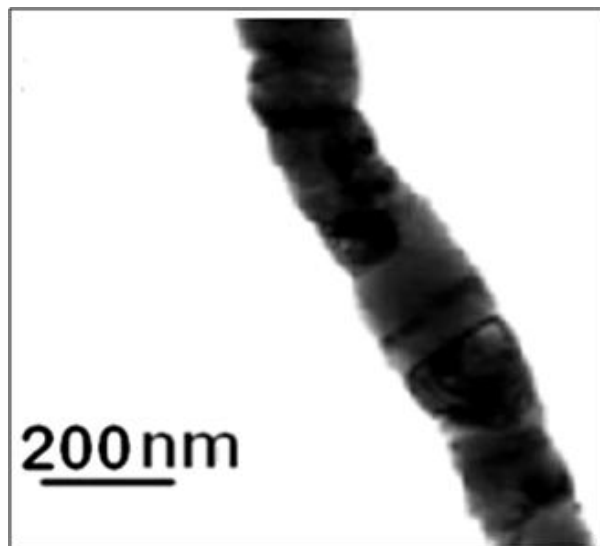


Figure 3-3. TEM image of a $\text{Li}_2\text{MnSiO}_4$ /carbon composite nanofiber.

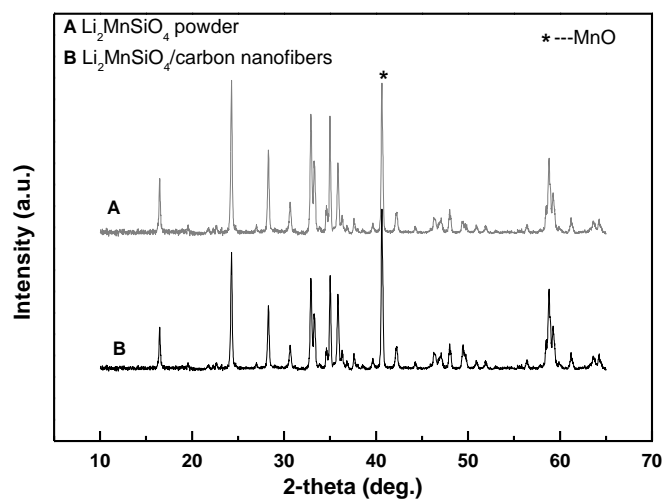


Figure 3-4. X-ray diffraction patterns of (A) $\text{Li}_2\text{MnSiO}_4$ powder, and (B)

$\text{Li}_2\text{MnSiO}_4$ /carbon nanofibers.

Fig. 3-5 shows representative charge-discharge curves of both $\text{Li}_2\text{MnSiO}_4$ powder and $\text{Li}_2\text{MnSiO}_4$ /carbon composite nanofibers. The charge and discharge capacities of $\text{Li}_2\text{MnSiO}_4$ powder are 215 and 176 mAh/g, respectively. Incorporating $\text{Li}_2\text{MnSiO}_4$ into composite carbon nanofibers increases the second-cycle charge and discharge capacities to 218 and 185 mAh/g, respectively. The reversible capacity for one electron transfer per transition metal is 167 mAh/g. Therefore, an electrochemical reaction of more than one electron transfer has been realized.

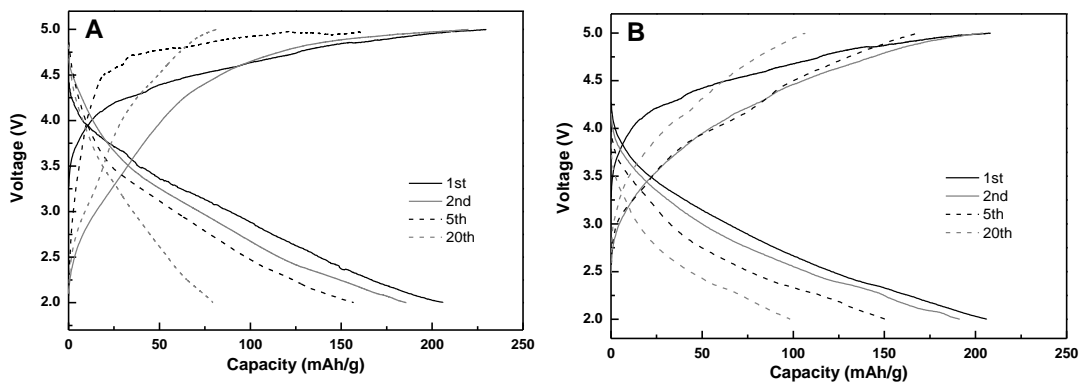


Figure 3-5. Galvanostatic charge-discharge curves of (A) $\text{Li}_2\text{MnSiO}_4$ powder, and (B) $\text{Li}_2\text{MnSiO}_4$ /carbon nanofibers.

From Fig. 3-5, it is also seen that $\text{Li}_2\text{MnSiO}_4$ powder has a discharge capacity of only 80 mAh/g after 20 cycles, corresponding to a capacity retention of 37%. However,

$\text{Li}_2\text{MnSiO}_4$ /carbon composite nanofibers exhibit higher capacity retention with 98 mAh/g at 20th cycle, indicating a capacity retention of 54% of the initial cycle.

The electrochemical performance, especially the cycling performance, is directly related to the robustness of the electrical contact between active particles. Embedding active particles into carbon nanofiber matrix can lead to higher and more robust electronic conductivity of the electrodes [8,9]. The enhanced cycling performance of $\text{Li}_2\text{MnSiO}_4$ /carbon nanofibers may be attributed to the improved electronic conductivity provided by the carbon nanofiber matrix with more pathways and shorter diffusion lengths for ions and electrons. In addition to facilitating charge transfer among active particles, the hybridization of carbon nanofibers with active $\text{Li}_2\text{MnSiO}_4$ particles also keeps the primary $\text{Li}_2\text{MnSiO}_4$ particles from further aggregation by confining them in the nanofibrous network structure.

4. Conclusions

$\text{Li}_2\text{MnSiO}_4$ /carbon nanofibers were prepared by electrospinning and heat treatment. For comparison, $\text{Li}_2\text{MnSiO}_4$ powder was also prepared. $\text{Li}_2\text{MnSiO}_4$ powder shows charge and discharge capacities of 215 and 176 mAh/g, respectively, at the second cycle. These capacities faded dramatically with a capacity loss of 63% at the 20th cycle. Incorporating $\text{Li}_2\text{MnSiO}_4$ particles into carbon nanofibers showed charge and discharge capacities of 218 and 185 mAh/g at the second cycle, respectively, indicating an electrochemical reaction of more than one electron transfer per transition metal. In addition, the capacity

retention was improved to 54% after 20 cycles.

References

- [1] Thackeray MM, David WIF, Bruce PG, Goodenough JB. Lithium insertion into manganese spinels. *Mater Res Bull* 1983;18:461-472.
- [2] Yang, S, Song S, Zavalij PY, Whittingham MS. Reactivity, stability and electrochemical behavior of lithium iron phosphates. *Electrochemistry Communications* 2002;4:239-244.
- [3] Toprakci O, Ji L, Lin Z, Toprakci HAK, Zhang X. Fabrication and electrochemical characteristics of electrospun LiFePO_4 /carbon composite fibers for lithium-ion batteries. *Journal of Power Sources* 2011;196(18):7692-7699.
- [4] Nyten A, Abouimrane A, Armand M, Gustafsson T, Thomas JO. Electrochemical performance of $\text{Li}_2\text{FeSiO}_4$ as a new Li-battery cathode material. *Mater Chem* 2005;7:156-160.
- [5] Nyten A, Kamali S, Hangstrom L, Gustafsson T, Thomas JO. The lithium extraction/insertion mechanism in $\text{Li}_2\text{FeSiO}_4$. *Mater Chem* 2006;16:2266-2272.
- [6] Dominko R, Bele M, Kokalj A, Gaberscek, M, Jamnik J. $\text{Li}_2\text{MnSiO}_4$ as a potential Li-battery cathode material. *Journal of Power Sources* 2007;174:457-461.
- [7] Dominko R, Bele M, Gaberscek M, Meden A, Remskar M, Jamnik J. Structure and electrochemical performance of $\text{Li}_2\text{MnSiO}_4$ and $\text{Li}_2\text{FeSiO}_4$ as potential Li-battery cathode materials. *Electrochemistry Communications* 2006;8:217-222.
- [8] Lin Z, Ji L, Woodroof M, Zhang X. Electrodeposited MnO_x /carbon nanofiber

composites for use as anode materials in rechargeable lithium-ion batteries. *Journal of Power Sources* 2010;195:5025-5031.

[9] Ji L, Lin Z, Medford AJ, Zhang X. In-Situ encapsulation of nickel particles in electrospun carbon nanofibers and their Electrochemical performance. *Chem Eur J* 2009;15:10718-10722.

Chapter 4 High-Capacity $\text{Li}_2\text{Mn}_{0.8}\text{Fe}_{0.2}\text{SiO}_4$ /Carbon Composite Nanofiber Cathodes for Lithium-Ion Batteries

$\text{Li}_2\text{MnSiO}_4$ has been considered as a promising cathode material with an extremely high theoretical capacity of 332 mAh/g. However, due to its low intrinsic conductivity and poor structural stability, only about half of the theoretical capacity has been realized in practice and the capacity decays rapidly during cycling. To realize the high capacity and improve the cycling performance, $\text{Li}_2\text{Mn}_{0.8}\text{Fe}_{0.2}\text{SiO}_4$ /carbon composite nanofibers were prepared by the combination of iron doping and electrospinning. X-ray diffraction, scanning electron microscope, and transmission electronic microscope were applied to characterize the $\text{Li}_2\text{Mn}_{0.8}\text{Fe}_{0.2}\text{SiO}_4$ /carbon nanofibers. It was found that $\text{Li}_2\text{Mn}_{0.8}\text{Fe}_{0.2}\text{SiO}_4$ nanoparticles were embedded into continuous carbon nanofiber matrices, which formed free-standing porous mats that could be used as binder-free cathodes. The iron doping improved the conductivity and purity of the active material, and the carbon nanofiber matrix facilitated ion transfer and charge diffusion. As a result, $\text{Li}_2\text{Mn}_{0.8}\text{Fe}_{0.2}\text{SiO}_4$ /carbon nanofiber cathodes showed promising improvement on reversible capacity and cycling performance.

1. Introduction

Among various known cathode materials for Li-ion batteries, LiCoO_2 , LiMn_2O_4 and LiNiO_2 have been most widely studied. Recently, LiFePO_4 provided an alternative for cathode materials with higher thermal stability and environmental benign nature [1,2].

LiFePO₄ has a theoretical capacity of 170 mAh/g; however, with the emerging high demand of Li-ion batteries for providing electricity in hybrid electric vehicles and storing energy in power grids, it falls short to offer sufficient specific capacity and energy density. Dominko [3] firstly synthesized and characterized a new material Li₂MnSiO₄ with the possibility to deliver two lithium ions per formula unit, leading to a theoretical capacity of 333 mAh/g. However, only less than one lithium ion per formula unit has been realized in practice, and serious capacity loss was also observed during cycling [3]. The poor conductivity (5×10^{-16} S/cm) and slow kinetics of Li₂MnSiO₄ are probably the main reason why researchers have not been able to extract more than one lithium ion per formula unit [4]. To circumvent the low electronic conductivity and slow kinetics of the lithium orthosilicate, several methods were employed including size reduction [3], carbon coating [5], and super-valent metal doping [6]. Although progress has been made by these methods, the overall performance of Li₂MnSiO₄ is still not sufficient for practical battery applications.

Electrospinning is considered as a simple but versatile strategy to fabricate various inorganic materials such as titanium oxide [7] and LiFePO₄ [8,9], and organic polymeric nanofibers as well. Herein, we report a novel approach for the synthesis of Li₂Mn_{0.8}Fe_{0.2}SiO₄/carbon composite nanofibers by iron doping and electrospinning to incorporate both advantages of structure optimization and electronic/ionic conductivity enhancement. Electrochemical results show that Li₂Mn_{0.8}Fe_{0.2}SiO₄/carbon nanofiber cathodes exhibited promising improvement in terms of reversible capacity and cycling

performance.

2. Experimental

2.1 Chemicals

N,N-dimethylformamide (DMF), manganese (II) acetate (98%), citric acid (>99.5%), and ethylene glycol (99%) were purchased from Sigma-Aldrich Chemical Company Inc (USA). Polyacrylonitrile (PAN, Mw= 150,000) was ordered from Pfaltz & Bauer Inc. Lithium acetate dihydrate (98%), iron acetate (98%), and tetraethyl orthosilicate (98%) were obtained from Acros Organics. Electrolyte composed of 1 mol of lithium hexafluorophosphate (LiPF₆) in a mixture solution of ethylene carbonate (EC), diethyl carbonate (DEC), and dimethyl carbonate (DMC) with a volume ratio of 1:1:1 was purchased from MTI corporation. All materials were used as-received without further purification.

2.2 Preparation of Li₂Mn_{0.8}Fe_{0.2}SiO₄ Powder

Li₂Mn_{0.8}Fe_{0.2}SiO₄ was prepared by a citric acid-assisted sol-gel Pechini method [3]. The synthesis was carried out by firstly dissolving lithium acetate, manganese acetate, and iron acetate with a molar ratio of 2.0:0.8:0.2 in distilled water under vigorous stirring for 2 hours. A saturated aqueous solution of citric acid and ethylene glycol complexation agents with a ratio of 2:1 was then slowly added into the above mixture under continuous stirring. After 12 hours, a homogenous solution was formed, and then it was transferred into a reflux system. Tetraethyl orthosilicate in ethanol was then added to the system by

about one drop per minute, and the solution was maintained at 80 °C under magnetic stirring during the entire process. A greenish solution was formed and it was kept at 75 °C to form a wet gel. The gel was vacuum-dried at 100 °C and was then ground with mortar and pestle. The obtained mixture was heat treated in a furnace at 700 °C for 12 hours in flowing argon. The resultant $\text{Li}_2\text{Mn}_{0.8}\text{Fe}_{0.2}\text{SiO}_4$ product was ground with mortar and pestle again for at least one hour. For comparison, $\text{Li}_2\text{MnSiO}_4$ powder was also prepared using the same method.

2.3 Fabrication of $\text{Li}_2\text{Mn}_{0.8}\text{Fe}_{0.2}\text{SiO}_4$ /Carbon Composite Nanofibers

PAN was used as the carbon source and electrospinning media. The electrospinning solution was prepared by mixing the obtained $\text{Li}_2\text{Mn}_{0.8}\text{Fe}_{0.2}\text{SiO}_4$ powder with an 8 wt% PAN solution in DMF. The content of $\text{Li}_2\text{Mn}_{0.8}\text{Fe}_{0.2}\text{SiO}_4$ was 65 wt% of the total mixture solution. A high voltage power supply (Gamma ES40P-20W/DAM) was used to provide a high voltage at around 20 kV for electrospinning. Fibers were collected on an aluminum plate as a mat. The electrospun $\text{Li}_2\text{Mn}_{0.8}\text{Fe}_{0.2}\text{SiO}_4$ /PAN nanofibers were firstly stabilized in air environment at 280 °C for 5 hours with a heating rate of 5 °C/min, and then carbonized at 700 °C for 8 hours with a heating rate of 2°C/min in high purity argon atmosphere.

2.4 Nanofiber Characterization

The morphology of $\text{Li}_2\text{Mn}_{0.8}\text{Fe}_{0.2}\text{SiO}_4$ /carbon nanofibers were evaluated by scanning electron microscopy (JEOL 6400 FESEM at 20 kV) and transmission electron

microscopy (Hitach HF-2000 TEM at 200 kV). The structure of $\text{Li}_2\text{Mn}_{0.8}\text{Fe}_{0.2}\text{SiO}_4$ /carbon nanofibers was also characterized using X-ray diffraction (Rigaku Smartlab).

2.5 Electrochemical Evaluation

Electrochemical tests were performed using 2032 coin-type half cells. The $\text{Li}_2\text{Mn}_{0.8}\text{Fe}_{0.2}\text{SiO}_4$ /carbon nanofiber mats were cut into circular electrodes by a punch of 1/2 inch in diameter. Li sheet was used as the counter electrode, and polypropylene (PP) film (Cellgard 2400) as the separator. The electrolyte used was 1 M solution of LiPF_6 in an EC/DMC/DEC mixture (1:1:1 by volume). The cell assembly process was carried out under dry argon atmosphere in a glove box. Charge and discharge were conducted on a Land battery testing system at a current density of C/20 between cut-off potentials of 2.0 and 4.8 V. For comparison, electrodes made from $\text{Li}_2\text{MnSiO}_4$ and $\text{Li}_2\text{Mn}_{0.8}\text{Fe}_{0.2}\text{SiO}_4$ powders were also prepared and tested by mixing powders with 10 wt% polyvinylidene fluoride (PVdF) binder and 10 wt% conducting carbon black and casting on aluminum current collector.

3. Results and Discussion

3.1 X-Ray Diffraction

The X-ray diffraction patterns obtained from $\text{Li}_2\text{MnSiO}_4$ and $\text{Li}_2\text{Mn}_{0.8}\text{Fe}_{0.2}\text{SiO}_4$ powders are presented in Fig. 4-1. Both $\text{Li}_2\text{MnSiO}_4$ and $\text{Li}_2\text{Mn}_{0.8}\text{Fe}_{0.2}\text{SiO}_4$ powders have the orthorhombic crystal structure and the space group is $\text{Pmn}2_1$. Without iron doping, $\text{Li}_2\text{MnSiO}_4$ has a large diffusion peak at $2\theta = 41^\circ$, which can be assigned to MnO as an

impurity. However, this impurity peak cannot be observed in iron-doped $\text{Li}_2\text{Mn}_{0.8}\text{Fe}_{0.2}\text{SiO}_4$, indicating that the iron doping can improve the purity of active material.

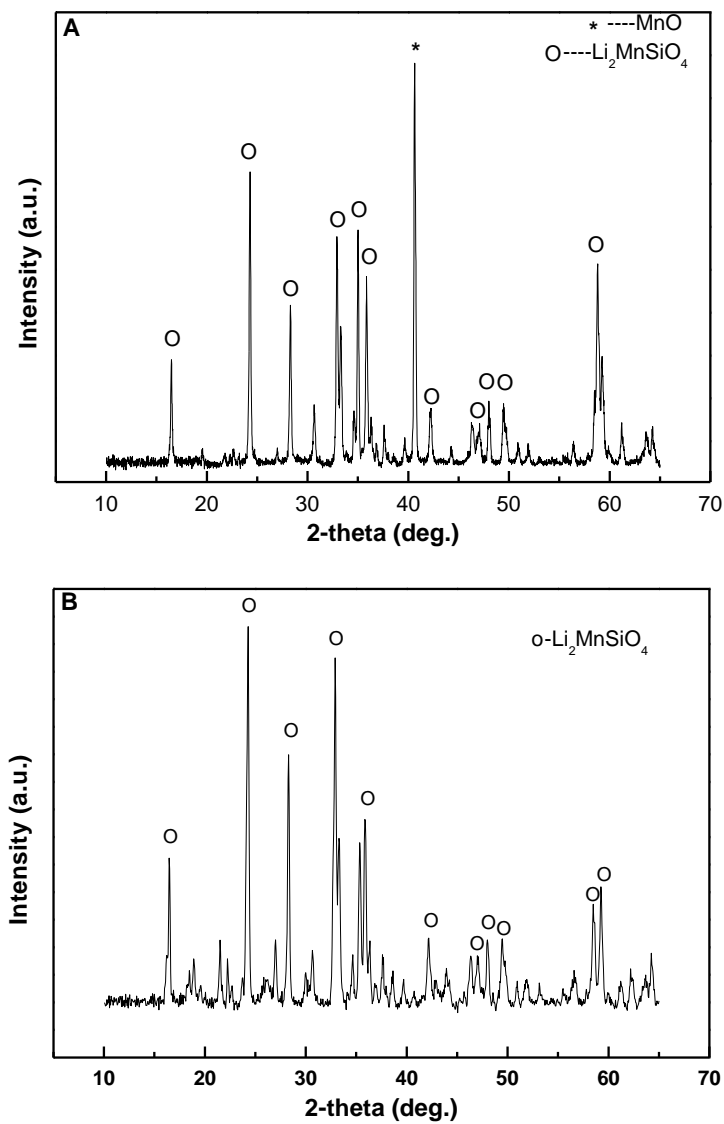


Figure 4-1. XRD patterns of (A) $\text{Li}_2\text{MnSiO}_4$ and (B) $\text{Li}_2\text{Mn}_{0.8}\text{Fe}_{0.2}\text{SiO}_4$ powders.

3.2 Morphology and Structure

Fig. 4-2 shows SEM images of $\text{Li}_2\text{MnSiO}_4$ and $\text{Li}_2\text{Mn}_{0.8}\text{Fe}_{0.2}\text{SiO}_4$ powders. Both $\text{Li}_2\text{MnSiO}_4$ and $\text{Li}_2\text{Mn}_{0.8}\text{Fe}_{0.2}\text{SiO}_4$ powders consist of agglomerated nanoparticles. For $\text{Li}_2\text{MnSiO}_4$, the primary particle diameter ranges from 30 to 50 nm. Iron doping decreases the particle size, and the primary particle diameter of $\text{Li}_2\text{Mn}_{0.8}\text{Fe}_{0.2}\text{SiO}_4$ powder is 15 - 30 nm. In addition, the particle distribution of $\text{Li}_2\text{Mn}_{0.8}\text{Fe}_{0.2}\text{SiO}_4$ powder is more uniform than that of $\text{Li}_2\text{MnSiO}_4$.

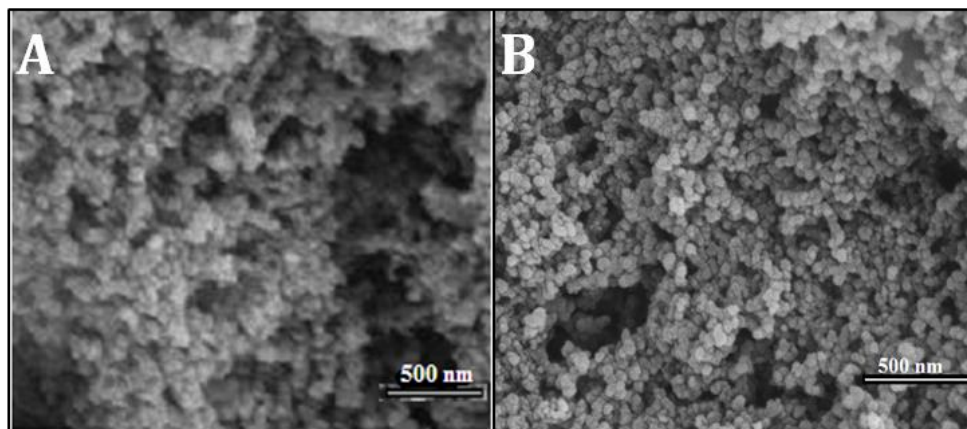


Figure 4-2. SEM images of (A) $\text{Li}_2\text{MnSiO}_4$ and (B) $\text{Li}_2\text{Mn}_{0.8}\text{Fe}_{0.2}\text{SiO}_4$ powders.

Fig. 4-3 shows SEM images of $\text{Li}_2\text{Mn}_{0.8}\text{Fe}_{0.2}\text{SiO}_4/\text{PAN}$ electrospun nanofibers. They exhibit a continuous fibrous morphology with relatively uniform diameter ranging from 160 to 230 nm. The randomly-aligned continuous fibers form a fibrous mat. The fiber surface is relatively rough probably due to the presence of active particles in the fibers.

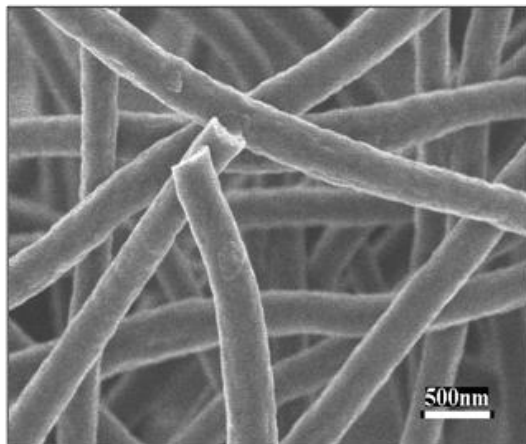


Figure 4-3. SEM image of electrospun $\text{Li}_2\text{Mn}_{0.8}\text{Fe}_{0.2}\text{SiO}_4/\text{PAN}$ nanofibers.

SEM images of $\text{Li}_2\text{Mn}_{0.8}\text{Fe}_{0.2}\text{SiO}_4/\text{carbon}$ nanofibers obtained after a thermal treatment of 700 °C in argon are presented in Fig. 4-4. After heat treatment, fibers become slimmer with diameters ranging from 76 to 158 nm. The diameter reduction is mainly caused by the removal of various species from PAN during the formation of carbon nanofiber matrix. Close-up images of the hybridization structure of $\text{Li}_2\text{Mn}_{0.8}\text{Fe}_{0.2}\text{SiO}_4$ particles with carbon nanofibers are shown in TEM images of Fig. 4-5. The TEM results confirm the formation of a $\text{Li}_2\text{Mn}_{0.8}\text{Fe}_{0.2}\text{SiO}_4/\text{carbon}$ nanocomposite with $\text{Li}_2\text{Mn}_{0.8}\text{Fe}_{0.2}\text{SiO}_4$ particles dispersed both along and inside the carbon nanofibers. Aggregation of primary particles or ‘beads-on-a-string’ morphology as shown in Fig. 4-5C can be only observed in a few small areas.

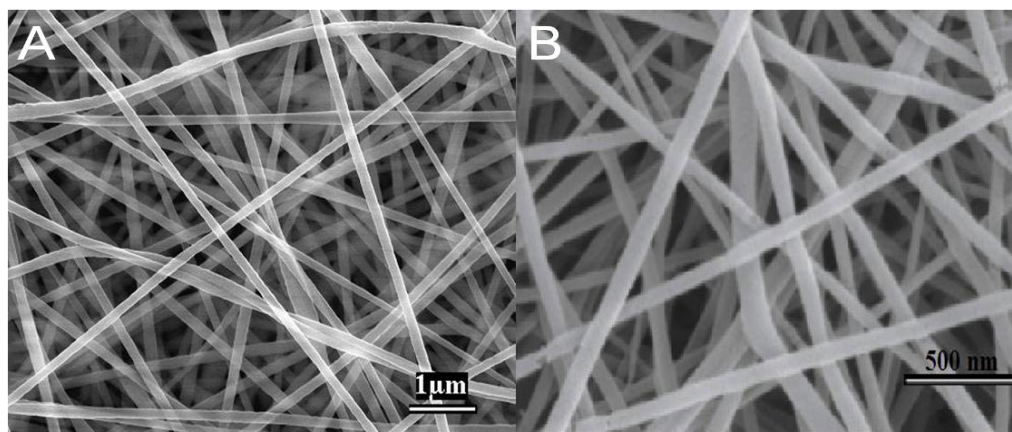


Figure 4-4. SEM images of $\text{Li}_2\text{Mn}_{0.8}\text{Fe}_{0.2}\text{SiO}_4$ /carbon nanofibers obtained after heat-treatment.

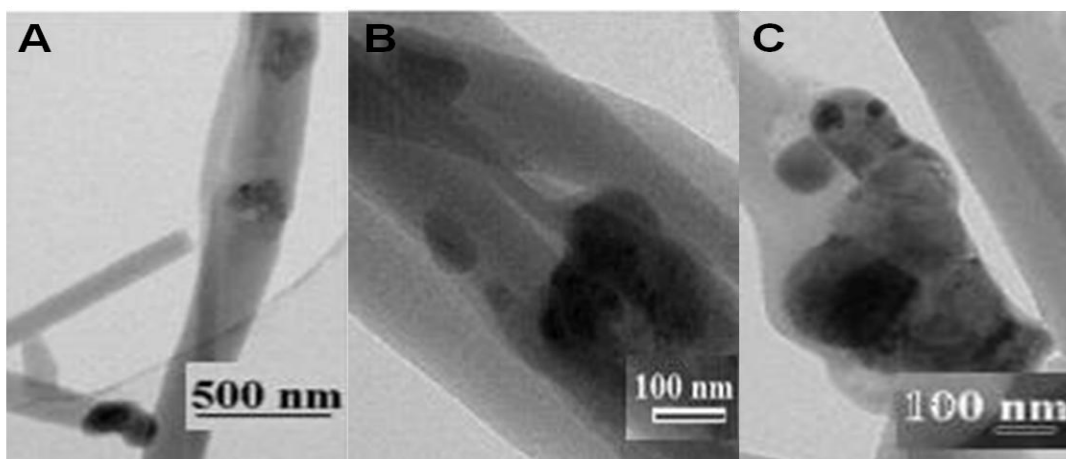


Figure 4-5. TEM images of $\text{Li}_2\text{Mn}_{0.8}\text{Fe}_{0.2}\text{SiO}_4$ /carbon nanofibers with magnifications of (A) $10,000\times$ and (B and C) $30,000\times$.

3.3 Raman Analysis

The Raman spectrum of $\text{Li}_2\text{Mn}_{0.8}\text{Fe}_{0.2}\text{SiO}_4$ /carbon nanofibers in the spectral region of 1100-2000 cm^{-1} was obtained (Fig. 6). Common Raman features of carbon materials are the presence of two strong bands at around 1350 and 1600 cm^{-1} , respectively. The strong peak centered near 1350 cm^{-1} (D-band) is characteristic of defect-induced structures of sp^3 structural disorder in the graphene layers of carbon materials, while the peak at 1600 cm^{-1} (G-band) is indicative of the high-frequency E_{2g} first-order graphitic crystallites [10]. As shown in Fig. 4-6, the spectrum of $\text{Li}_2\text{Mn}_{0.8}\text{Fe}_{0.2}\text{SiO}_4$ /carbon nanofibers clearly indicates the presence of both D band and G band, and hence the carbon nanofiber matrix is composed of both disordered carbon and ordered graphene sheets. However, the intensity of G band is greater than that of D band, suggesting a good structural integrity.

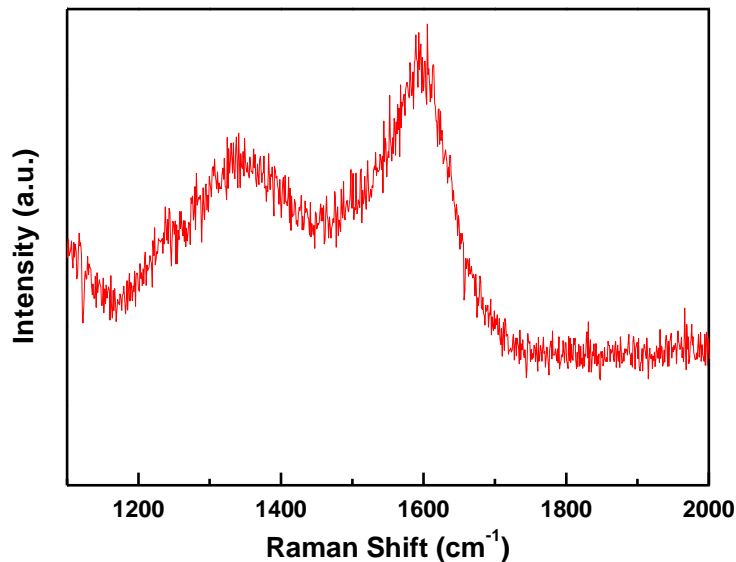


Figure 4-6. Raman spectrum of $\text{Li}_2\text{Mn}_{0.8}\text{Fe}_{0.2}\text{SiO}_4$ /carbon composite nanofibers.

3.4 Electrochemical Properties

To evaluate the electrochemical performance of $\text{Li}_2\text{Mn}_{0.8}\text{Fe}_{0.2}\text{SiO}_4$ /carbon nanofibers, charge-discharge cycles were conducted at room temperature between 2.0 to 5.0 V at a current density of C/20 (16.65 mA/g), and the results are shown in Fig. 4-7. For comparison, the charge-discharge curves of $\text{Li}_2\text{MnSiO}_4$ and $\text{Li}_2\text{Mn}_{0.8}\text{Fe}_{0.2}\text{SiO}_4$ powders are also shown. It is seen that $\text{Li}_2\text{MnSiO}_4$ powder presents a high discharge capacity of 212 mAh/g at the first cycle, corresponding to an electrode reaction of 1.27 electron transfer per formula unit. The discharge capacity of $\text{Li}_2\text{MnSiO}_4$ powder fades rapidly to less than one electron transfer per formula unit at the second cycle. Continuous capacity loss can be also observed after the second cycle. The capacity loss during cycling may be attributed to the intrinsic structural instability of $\text{Li}_2\text{MnSiO}_4$.

After iron doping, the resultant $\text{Li}_2\text{Mn}_{0.8}\text{Fe}_{0.2}\text{SiO}_4$ powder give a higher initial discharge capacity of 220 mAh/g at the first cycle, indicating a 1.32 electrons exchange per formula unit. At the 10th cycle, the discharge capacity of $\text{Li}_2\text{Mn}_{0.8}\text{Fe}_{0.2}\text{SiO}_4$ powder is 170 mAh/g, demonstrating that the electrode reaction still remains at more than one electron transfer per formula unit.

By introducing the $\text{Li}_2\text{Mn}_{0.8}\text{Fe}_{0.2}\text{SiO}_4$ powder into carbon nanofiber matrix, the resultant $\text{Li}_2\text{Mn}_{0.8}\text{Fe}_{0.2}\text{SiO}_4$ /carbon nanofibers show higher capacities and better capacity retention. For the first cycle, $\text{Li}_2\text{Mn}_{0.8}\text{Fe}_{0.2}\text{SiO}_4$ /carbon nanofibers exhibit charge and discharge capacities of 233 mAh/g and 224 mAh/g, respectively. At the 20th cycle, the discharge

capacity remains at 171 mAh/g, indicating a 1.02 electron transfer reaction per formula unit. In contrast, $\text{Li}_2\text{MnSiO}_4$ and $\text{Li}_2\text{Mn}_{0.8}\text{Fe}_{0.2}\text{SiO}_4$ powders show discharge capacities of 77 and 127 mAh/g at the 20th cycle.

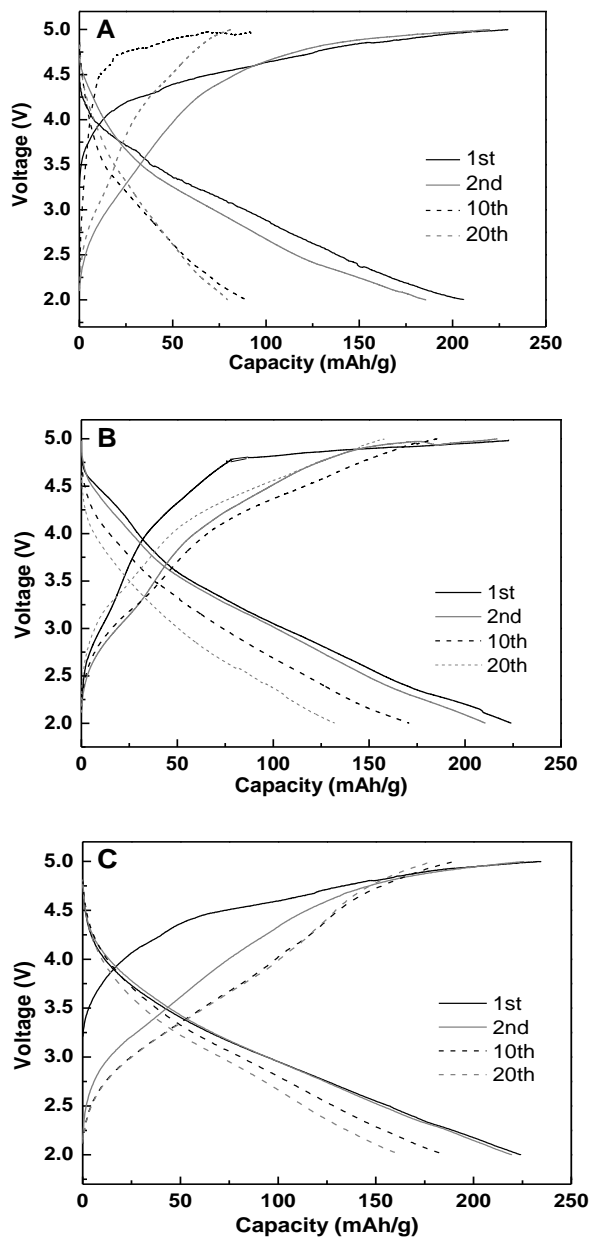


Figure 4-7. Charge-discharge curves of (A) $\text{Li}_2\text{MnSiO}_4$ powder, (B) $\text{Li}_2\text{Mn}_{0.8}\text{Fe}_{0.2}\text{SiO}_4$

powder, and (C) $\text{Li}_2\text{Mn}_{0.8}\text{Fe}_{0.2}\text{SiO}_4$ /carbon nanofibers.

Fig. 4-8 further compares the cycling performance of $\text{Li}_2\text{MnSiO}_4$ powder, $\text{Li}_2\text{Mn}_{0.8}\text{Fe}_{0.2}\text{SiO}_4$ powder, and $\text{Li}_2\text{Mn}_{0.8}\text{Fe}_{0.2}\text{SiO}_4$ /carbon nanofibers. Among all three cathode materials, $\text{Li}_2\text{Mn}_{0.8}\text{Fe}_{0.2}\text{SiO}_4$ /carbon nanofibers show the slowest capacity fading during cycling, with a capacity retention of 63.8% at the 50th cycle. The capacity retentions of $\text{Li}_2\text{MnSiO}_4$ and $\text{Li}_2\text{Mn}_{0.8}\text{Fe}_{0.2}\text{SiO}_4$ powders are only 20.5 and 41.3%, respectively, at the 50th cycle.

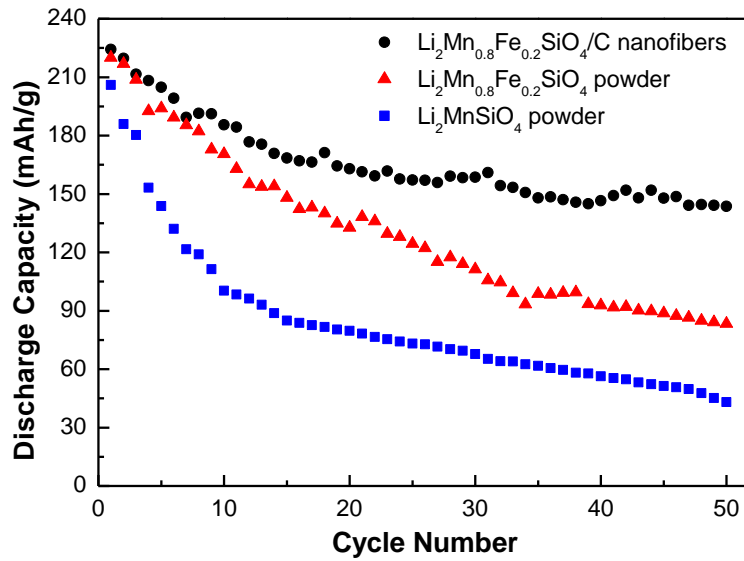


Figure 4-8. Cycling performance of $\text{Li}_2\text{MnSiO}_4$ powder, $\text{Li}_2\text{Mn}_{0.8}\text{Fe}_{0.2}\text{SiO}_4$ powder, and $\text{Li}_2\text{Mn}_{0.8}\text{Fe}_{0.2}\text{SiO}_4$ /carbon nanofibers.

The improved electrical performance of $\text{Li}_2\text{Mn}_{0.8}\text{Fe}_{0.2}\text{SiO}_4$ /carbon nanofibers can be

attributed to the effect of iron doping and the formation of conductive carbon nanofiber matrix. For $\text{Li}_2\text{MnSiO}_4$ powder, the poor electrochemical performance can be partially attributed to its low conductivity. As reported by Dominko [11], the measured conductivity of $\text{Li}_2\text{FeSiO}_4$ is two orders of magnitude higher than that of $\text{Li}_2\text{MnSiO}_4$. It is anticipated that $\text{Li}_2\text{Mn}_{0.8}\text{Fe}_{0.2}\text{SiO}_4$ with super-valent ion doping has higher conductivity than $\text{Li}_2\text{MnSiO}_4$ [11]. In addition to the enhanced conductivity, encapsulating active $\text{Li}_2\text{Mn}_{0.8}\text{Fe}_{0.2}\text{SiO}_4$ particles in the carbon nanofiber matrix keeps primary active particles from aggregation. The conductive carbon nanofiber matrix forms a three-dimensional porous network that can facilitate shorter transportation pathways for both lithium ions and electrons, which has been demonstrated in Si/carbon, Ni/carbon, $\text{Li}_4\text{Ti}_5\text{O}_{12}$ /carbon, and LiFePO_4 /carbon nanofiber electrodes [9,12-14]. Therefore, with combined advantages of enhanced conductivity resulted from iron doping and the improved electron and ion transportation due to the intimate networking of carbon nanofiber matrix, $\text{Li}_2\text{Mn}_{0.8}\text{Fe}_{0.2}\text{SiO}_4$ /carbon composite nanofibers have improved electrochemical performance.

However, the cycling performance of $\text{Li}_2\text{Mn}_{0.8}\text{Fe}_{0.2}\text{SiO}_4$ /carbon nanofibers remains an issue as the capacity still fades too fast during cycling. The absence of voltage plateaus is also indicative of irreversible structural changes. Herein, more work should be devoted to further enhancement of the kinetics and cycling stability of this new cathode material.

3.5 Conclusions

In this work, a super-valent ion doping was carried out to form $\text{Li}_2\text{Mn}_{0.8}\text{Fe}_{0.2}\text{SiO}_4$, and both cyclability and capacity retention were improved. Especially, for the first ten cycles, discharge capacities from more than one electron transfer reaction were delivered. The $\text{Li}_2\text{Mn}_{0.8}\text{Fe}_{0.2}\text{SiO}_4$ /carbon composite nanofibers were also prepared by a combination of electrospinning and heat treatment. The role of carbon fibers in the cathode material is mainly to facilitate fast transportation of electrons and lithium ions. This led to improved reversibility for $\text{Li}_2\text{Mn}_{0.8}\text{Fe}_{0.2}\text{SiO}_4$ /carbon nanofibers. Results demonstrated that $\text{Li}_2\text{Mn}_{0.8}\text{Fe}_{0.2}\text{SiO}_4$ /carbon nanofibers are as a promising high-capacity cathode material for Li-ion batteries.

References:

- [1]. S.Y. Chung, Y.M. Bloking, Y.M. Chiang, *Nature Materials* 1(2002) 123-128.
- [2]. O. Toprakci, H.A.K. Toprakci, L. Ji, *KONA Powder and Particle Journal* 28(2010) 50-73.
- [3]. R. Dominko, M. Bele, A. Kokalj, M. Gaberscek, J. Jamnik, *Journal of Power Sources* 174(2007) 457-461.
- [4]. R. Dominko, *Journal of Power Sources* 184(2008) 462-468.
- [5]. Y. Li, Z. Gong, Y. Yang, *Journal of Power Sources* 174(2007) 528-532.
- [6]. A. Kokalj, R. Dominko, G. Mali, A. Meden, M. Gaberscek, J. Jamnik, *Chem. Mater.* 19(2007) 3633-3640.

- [7]. N. Dharmaraj, H.C. Park, C.K. Kim, Y.K. Kim, D.R. Lee, *Mater. Chem. Phys.* 87(2004) 5-9.
- [8]. F. Yheng-Wen, J. Ma, Q. Zong, *Solid State Ionics* 176(2005) 1635-1640.
- [9]. O. Toprakci, L. Ji, Z. Lin, H.A.K. Toprakci, X. Zhang, *Journal of Power Sources* 196 (2011) 7692-7699.
- [10]. C. Kim, Y.I. Jeong, B.T. Ngoc, K.S. Yang, M. Kojima, Y.A. Kim, *Small*. 3(1)(2007) 91-95.
- [11]. M.E. Dompablo, U. Amador, J.M. Gallardo-Amores, E. Moran, H. Eharenberg, L. Dupont, R. Dominko, *Journal of Power Sources*, 189(2009) 638-642.
- [12]. L. Ji, Z. Lin, A.J. Medford, X. Zhang, *Chem. Eur. J.* 15(2009) 10718-10722.
- [13]. Z. Lin, L. Ji, M. Woodroof, X. Zhang, *Journal of Power Sources* 195(2010) 5025-5031.
- [14]. B. Guo, Y. Li, Y. Yao, Z. Lin, L. Ji, G. Xu, Y. Liang, Q. Shi, X. Zhang, *Solid State Ionics* 204(2011) 61-65.

Chapter 5 Cr-Doped $\text{Li}_2\text{MnSiO}_4$ /Carbon Composite Nanofibers as High-Energy Cathodes for Li-Ion Batteries

$\text{Li}_2\text{MnSiO}_4$ with an extremely high theoretical capacity of 332 mAh/g has recently gained tremendous interest. However, only around half of this capacity has been realized in practice and the cycling performance is also poor due to the low intrinsic conductivity and unsatisfactory structure stability. In this study, $\text{Li}_2\text{Mn}_{(1-x)}\text{Cr}_x\text{SiO}_4$ /carbon composite nanofibers are prepared by the combination of electrospinning and Cr doping. The electrospinning process leads to the formation of a conductive carbon nanofiber matrix, which provides fast ion transport and charge transfer. Cr doping further improves crystal structure stability by increasing the unit cell volume and inducing defects in the lattice. The resultant $\text{Li}_2\text{Mn}_{(1-x)}\text{Cr}_x\text{SiO}_4$ /carbon composite nanofibers exhibit a high discharge capacity of 314 mAh/g at the 5th cycle and stable cycling performance.

1. Introduction

Traditional cathode materials, such as LiCoO_2 and LiMn_2O_4 , have relatively low capacities of about 140 and 130 mAh/g, respectively. The search for new cathode materials with higher energy densities has hence become one of the most active fields in Li-ion battery research. Among various cathode materials, $\text{Li}_2\text{MnSiO}_4$ has gained tremendous research interests due to its low cost, low pollution to environment, and thermal stability.^[1, 2, 3] Most importantly, different from Fe, which has only two oxidation

states (Fe^{II} and Fe^{III}), the fully reduction of Mn^{II} from Mn^{IV} allows complete delithiation of $\text{Li}_2\text{MnSiO}_4$,^[4] which potentially enables two lithium ion extractions per transition metal and delivers a high theoretical capacity of around 330 mAh/g. However, although research has been devoted to utilize all the redox states of the constituent Mn, including enhancing the intrinsic conductivity of $\text{Li}_2\text{MnSiO}_4$ by carbon coating and iron doping in the Li-site,^[5, 6] desirable capacity and cycling performance still have not been obtained for this material. So far, the highest reported discharge capacity for $\text{Li}_2\text{MnSiO}_4$ is 209 mAh/g at the first cycle, obtained from Yang's group.^[5] However, this capacity faded rapidly in a few cycles. It is commonly accepted that the poor electrochemical performance of $\text{Li}_2\text{MnSiO}_4$ is associated with its low intrinsic conductivity and the collapse of crystal structure during lithium extraction process.^[5, 6] A strategy that can increase the conductivity, stabilize the crystal structure and improve the performance of $\text{Li}_2\text{MnSiO}_4$ is in urgent need.

In this chapter, $\text{Li}_2\text{Mn}_{(1-x)}\text{Cr}_x\text{SiO}_4$ ($x = 0.03, 0.06, \text{ and } 0.1$) was prepared by acid-assisted sol-gel method and was incorporated into a carbon nanofiber matrix by electrospinning. The synergistic effects of Cr doping and 1-dimensional carbon nanofiber network enhanced the material conductivity and stability, and the resultant $\text{Li}_2\text{Mn}_{(1-x)}\text{Cr}_x\text{SiO}_4$ /carbon nanofiber cathodes have excellent electrochemical performance, in terms of high capacity and improved capacity retention.

2. Experimental

2.1. Chemicals

N,N-dimethylformamide (DMF), manganese (II) acetate (98 %), chromium (III) nitrate nonhydrate (99 %), citric acid (99.5 %), and ethylene glycol (99 %) were purchased from Sigma-Aldrich Chemical Company Inc (USA). Polyacrylonitrile (PAN, Mw = 150,000) was ordered from Pfaltz & Bauer Inc. Lithium acetate dihydrate (98 %), iron acetate (98 %), and tetraethyl orthosilicate (98 %) were obtained from Acros Organics.

Electrolyte composed of 1 M of lithium hexafluorophosphate (LiPF₆) in a mixture of ethylene carbonate (EC), diethyl carbonate (DEC), and dimethyl carbonate (DMC) with a volume ratio of 1:1:1 was purchased from MTI corporation. All materials were used as received without further purification.

2.2. Preparation of Li₂Mn_xCr_(1-x)SiO₄ Powders

Li₂Mn_(1-x)Cr_xSiO₄ was prepared by a citric acid-assisted sol-gel method [4].

Stoichiometric amounts of lithium acetate dihydrate, chromium nitrate nonhydrate and manganese acetate were first dissolved in distilled water with different molar ratios of 2.00:0.03:0.97, 2.00:0.06:0.94, and 2.00:0.10:0.90 under vigorous stirring for 2 hours. A saturated aqueous solution of citric acid and ethylene glycol as complexation agents with a ratio of 2:1 was then slowly added into the mixed solutions. Tetraethyl orthosilicate in ethanol solution was also added to the solutions by about one drop per second, and the solutions were maintained at 80 °C under magnetic stirring. After 12 hours of reflux, light

pink solutions were formed and they were kept at 75 °C to evaporate ethanol and water. The resultant wet gels were then dried in vacuum at 100 °C. After complete drying, they were ground with mortar and pestle. The obtained particles were then calcined at 700 °C for 12 hours in grade 5.0 argon flows. The final products were ground with mortar and pestle again for at least one hour to obtain fine $\text{Li}_2\text{Mn}_{(1-x)}\text{Cr}_x\text{SiO}_4$ powders. For comparison, undoped $\text{Li}_2\text{MnSiO}_4$ powder was also prepared using the same method without adding chromium nitrate nonhydrate as the doping agent.

2.3. Fabrication of $\text{Li}_2\text{Mn}_{(1-x)}\text{Cr}_x\text{SiO}_4$ /Carbon Composite Nanofibers

DMF solutions of 8 wt % PAN containing 65 wt % $\text{Li}_2\text{Mn}_{(1-x)}\text{Cr}_x\text{SiO}_4$ particles were prepared at 60 °C through strong mechanical stirring for at least 24 hours. A variable high voltage power supply (Gamma ES40P-20W/DAM) was used to provide a high voltage of 20 kV for the electrospinning of as-prepared solutions. The feed rate and the needle-collector distance were fixed at 1 mL h⁻¹ and 15 cm, respectively. Electrospun nanofibers were collected on the collector as free-standing and flexible mats.

The carbonization of $\text{Li}_2\text{Mn}_{(1-x)}\text{Cr}_x\text{SiO}_4$ /PAN nanofibers was performed in a programmable electric heat-treating furnace. The collected nanofiber mats were firstly stabilized under air at 280 °C for 5 hours (heating rate was 5 °C min⁻¹), and then were carbonized in Argon at 700 °C for 8 hours (heating rate was 2 °C min⁻¹) to form $\text{Li}_2\text{Mn}_{(1-x)}\text{Cr}_x\text{SiO}_4$ /carbon composite nanofibers.

2.4. Structure Characterization

The morphology and diameter of both $\text{Li}_2\text{Mn}_{(1-x)}\text{Cr}_x\text{SiO}_4$ powder and $\text{Li}_2\text{Mn}_{(1-x)}\text{Cr}_x\text{SiO}_4$ /carbon nanofibers were evaluated using scanning electron microscopy (SEM, JEOL 6400F FESEM at 5 kV) and transmission electron microscope (TEM, Hitachi HF2000 FETEM). The structure variations were identified by X-ray diffraction (Rigaku Smartlab). The lattice constants were obtained through Rietveld refining using a PDXL analysis software.

2.5. Electrochemical Evaluation

The electrochemical performance of $\text{Li}_2\text{Mn}_{(1-x)}\text{Cr}_x\text{SiO}_4$ powders and $\text{Li}_2\text{Mn}_{(1-x)}\text{Cr}_x\text{SiO}_4$ /carbon nanofibers was investigated using two-electrode coin-type half cells (CR2032) with metallic lithium as the counter electrode. The working electrodes were prepared using two different methods, depending on the type of active materials used. For $\text{Li}_2\text{Mn}_{(1-x)}\text{Cr}_x\text{SiO}_4$ powders, the electrodes were assembled by coating and drying the slurries of 80 wt% active material, 10 wt% conductive carbon black, and 10 wt% polyvinylidene fluoride (PVdF) in N-methylpyrrolidinone (NMP) on aluminum foils. On the other hand, $\text{Li}_2\text{Mn}_{(1-x)}\text{Cr}_x\text{SiO}_4$ /carbon nanofibers form free-standing porous membranes and they were directly punched into electrodes of 0.5 inch in diameter without using PVdF binder. All materials were dried in vacuum oven at 120 °C for one day before they were transferred into glove box. A polypropylene (PP) film (Cellgard 2400) was used as the separator. The coin cell assembly was carried out under a dry

argon atmosphere. The galvanostatic charge/discharge characteristics of the cells were recorded with a LAND battery-testing system in the voltage range of 2.0-5.0 V at room temperature.

3. Results and Discussion

3.1. Morphology and Structure Characterization

Figure 5-1 shows SEM images of synthesized $\text{Li}_2\text{MnSiO}_4$ and $\text{Li}_2\text{Mn}_{(1-x)}\text{Cr}_x\text{SiO}_4$ ($x = 0.06$) powders. It is seen that both powders are composed of nanosized primary particles. The particle size of $\text{Li}_2\text{MnSiO}_4$ powder ranges from 30 to 60 nm. The Cr doping reduces the primary particle size, and the size of $\text{Li}_2\text{Mn}_{0.94}\text{Cr}_{0.06}\text{SiO}_4$ powder is between 15 and 40 nm.

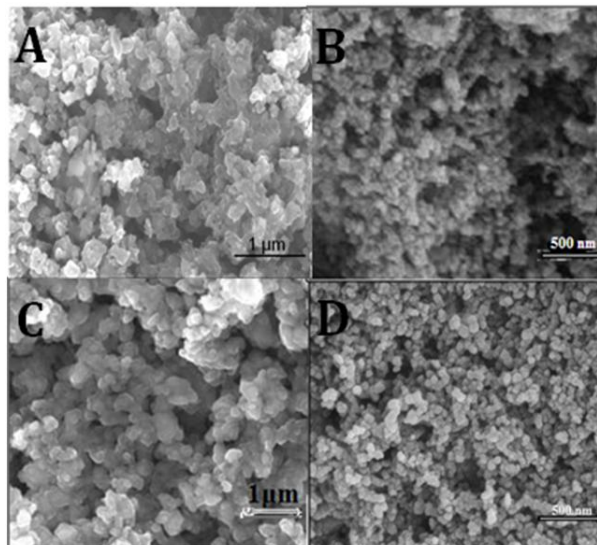


Figure 5-1. SEM images of (A and B) $\text{Li}_2\text{MnSiO}_4$ and (C and D) $\text{Li}_2\text{Mn}_{0.94}\text{Cr}_{0.06}\text{SiO}_4$ powders.

SEM images of $\text{Li}_2\text{Mn}_{0.94}\text{Cr}_{0.06}\text{SiO}_4/\text{PAN}$ precursor fibers are shown in Figure 5-2. It is seen that these nanofibers are uniform without the presence of bead-like irregularities. The fiber diameters vary from 180 to 250 nm. As presented in Figure 5-3, after carbonization, the diameters of the resultant $\text{Li}_2\text{Mn}_{0.94}\text{Cr}_{0.06}\text{SiO}_4/\text{carbon}$ nanofibers decrease to 70 - 150 nm, creating an increased surface area and enabling more contact with the liquid electrolyte. Due to the removal of non-carbon species during heat treatment at 700 °C, fibers present a curved rather than straight morphology.

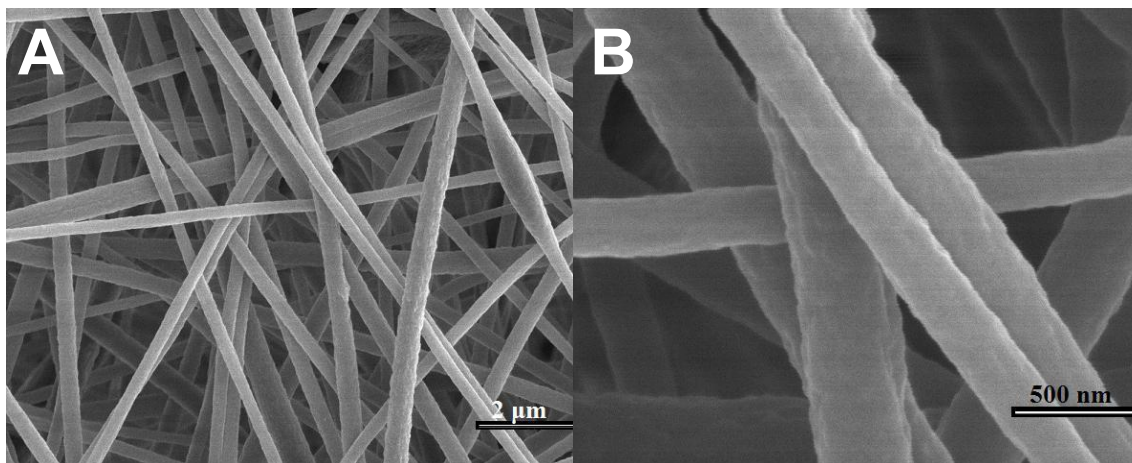


Figure 5-2. SEM images of Li₂Mn_{0.94}Cr_{0.06}SiO₄/PAN nanofibers.

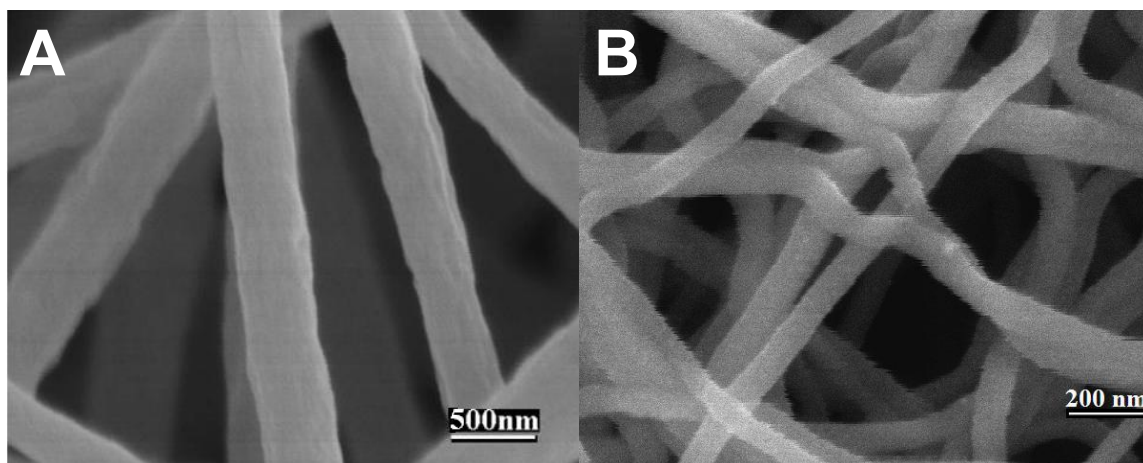


Figure 5-3. SEM images of Li₂Mn_{0.94}Cr_{0.06}SiO₄/carbon nanofibers.

Figure 5-4 shows TEM images of Li₂Mn_{0.94}Cr_{0.06}SiO₄/carbon nanofibers. Results confirm that Li₂Mn_{0.94}Cr_{0.06}SiO₄ particles are dispersed inside the carbon nanofiber matrix. As shown in Figure 4C, some Li₂Mn_{0.94}Cr_{0.06}SiO₄ particles aggregate to form clusters, but

they are still smaller than 300 nm.

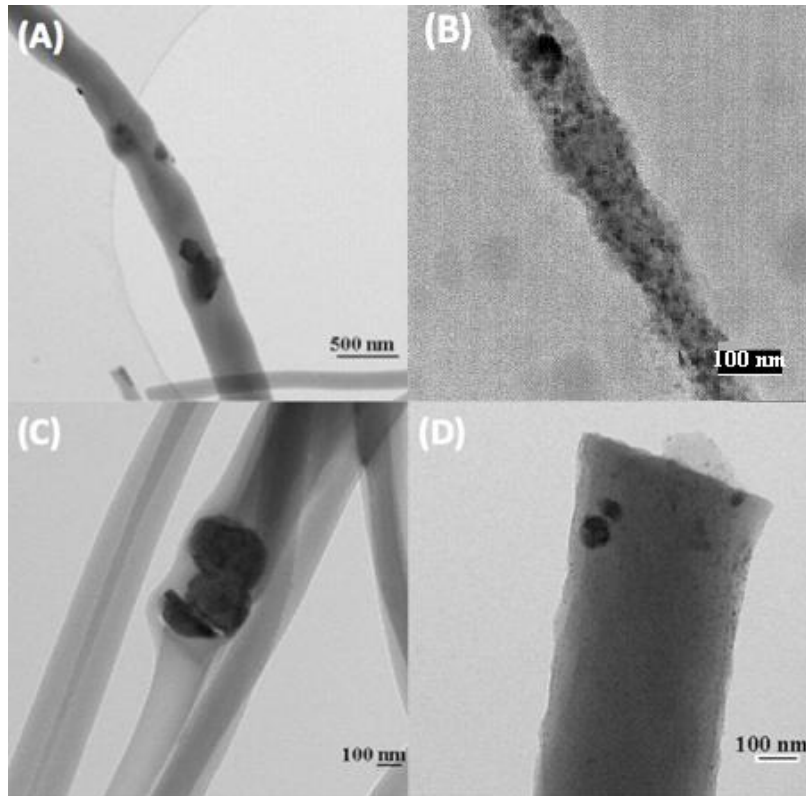


Figure 5-4. TEM images of $\text{Li}_2\text{Mn}_{0.94}\text{Cr}_{0.06}\text{SiO}_4$ /carbon nanofibers with different magnifications of (A) 20,000 \times , and (B, C, and D) 30,000 \times .

3.2. X-ray Diffraction Analysis

X-ray diffraction was employed to identify the compositions of prepared $\text{Li}_2\text{MnSiO}_4$ and $\text{Li}_2\text{Mn}_{(1-x)}\text{Cr}_x\text{SiO}_4$ powders with different doping ratios. The diffraction patterns are shown in Figure 5, and the calculated lattice parameters are listed in Table 5-1.

According to the ICSD patterns of $\text{Li}_2\text{MnSiO}_4$, there are two different types of crystalline

structures (00-055-0704 and 00-075-7861), *i.e.*, orthorhombic and monoclinic.^[7, 8] The pure $\text{Li}_2\text{MnSiO}_4$ powder prepared without Cr doping presents an orthorhombic crystal structure with $\text{Pmn}2_1$ space group. This is consistent with the structure observed by Dominko et al., as indicated by blue dash droplines shown in Figure 5A.^[7] From Table 1, it is seen that the unit cell volume (V) and unit cell volume per formula unit (V/z) of $\text{Li}_2\text{MnSiO}_4$ are 168.616 and 84.308 \AA^3 .

Table 1. Experimental Lattice Parameters (a, b, c), Unit Cell Volumes (V) and Unit Cell Volumes per Formula Unit (V/z) for $\text{Li}_2\text{MnSiO}_4$ and $\text{Li}_2\text{Mn}_{(1-x)}\text{Cr}_x\text{SiO}_4$ (x = 0.03, 0.06, and 0.10).

Samples	a (\AA)	b (\AA)	c (\AA)	α ($^\circ$)	β ($^\circ$)	γ ($^\circ$)	V (\AA^3)	V/Z (\AA^3)
$\text{Li}_2\text{MnSiO}_4$	6.311	5.380	4.966	90.00	90.00	90.00	168.616	84.308
$\text{Li}_2\text{Mn}_{0.97}\text{Cr}_{0.03}\text{SiO}_4$	6.300	5.341	5.101	90.00	90.00	90.00	171.640	85.820
$\text{Li}_2\text{Mn}_{0.94}\text{Cr}_{0.06}\text{SiO}_4$	6.316	10.910	5.084	90.00	91.09	90.00	350.263	87.566
$\text{Li}_2\text{Mn}_{0.90}\text{Cr}_{0.10}\text{SiO}_4$	6.400	5.400	4.870	90.00	90.00	90.00	168.307	84.154

In the case of $\text{Li}_2\text{Mn}_{(1-x)}\text{Cr}_x\text{SiO}_4$ powders, at x = 0.03, the XRD pattern still suggests an orthorhombic structure with $\text{Pmn}2_1$ space group. However, the V and V/z values increase slightly to 171.640 and 85.820 \AA^3 , respectively. As Cr doping increases to 0.06, a significant structure change is observed. The crystal structure shifts to monoclinic system with $\text{Pn}7$ space group, and the V and V/z values increase to 350.263 and 87.566 \AA^3 ,

respectively. This suggests that the structure of Cr-doped $\text{Li}_2\text{MnSiO}_4$ is heavily dependent on the amount of Cr doping. However, the change is not monotonic. As Cr doping continues to increase to 0.10, the crystal structure reverts to be orthorhombic, and the V and V/z values decrease to 168.307 and 84.154 \AA^3 , respectively.

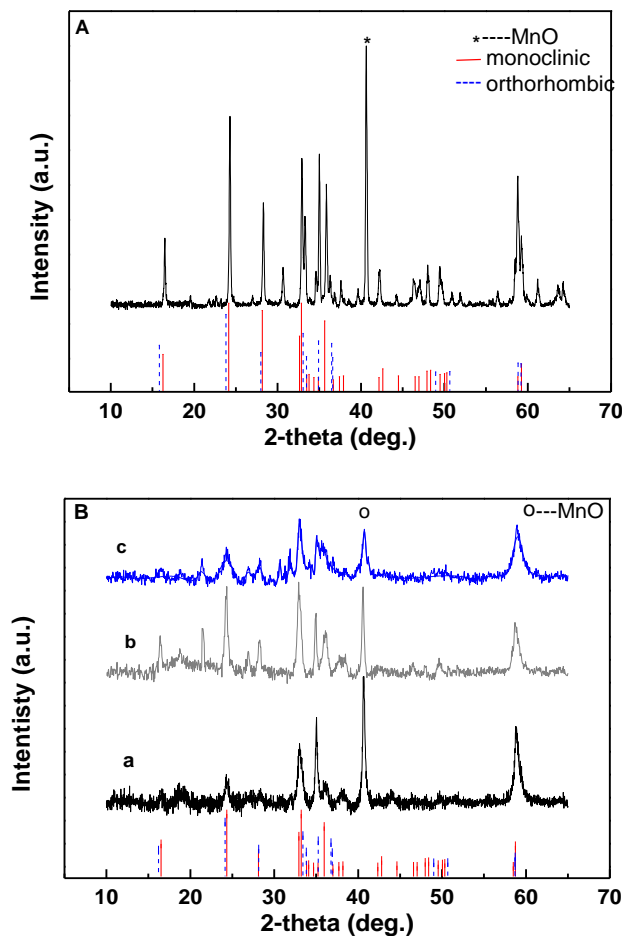


Figure 5-5. XRD diffractions of (A) $\text{Li}_2\text{MnSiO}_4$ and (B) $\text{Li}_2\text{Mn}_{(1-x)}\text{Cr}_x\text{SiO}_4$ (a: $x=0.03$, b: $x=0.06$, and c: $x=0.10$). Solid droplines correspond to $\text{Li}_2\text{MnSiO}_4$ with monoclinic structure, and dash droplines correspond to $\text{Li}_2\text{MnSiO}_4$ with orthorhombic structure.

From Figure 5-5, it is also seen that the $\text{Li}_2\text{MnSiO}_4$ powder has a strong peak at $2\theta = 40^\circ$, which is assigned to MnO as an impurity. With increase in Cr doping ratio, the intensity of the impurity peak decreases. This also indicates that Cr doping changes the crystal structure of the material rather than forming new impurities.

3.3. Electrochemical Performance

The electrochemical properties of $\text{Li}_2\text{Mn}_{(1-x)}\text{Cr}_x\text{SiO}_4$ powders and $\text{Li}_2\text{Mn}_{(1-x)}\text{Cr}_x\text{SiO}_4$ /carbon nanofibers were investigated at C/20 rate with cutoff voltages of 2.0 and 5.0 V. The charge-discharge curves of $\text{Li}_2\text{Mn}_{(1-x)}\text{Cr}_x\text{SiO}_4$ ($x = 0.03, 0.06, \text{ and } 0.1$) powders are shown in Figure 5-6. For comparison, the results of un-doped $\text{Li}_2\text{MnSiO}_4$ powder are also shown. It is seen that the $\text{Li}_2\text{MnSiO}_4$ powder delivers a high discharge capacity of 206 mAh/g at the initial cycle, but it fades rapidly with a high capacity loss of 61.3% at the 20th cycle. All three $\text{Li}_2\text{Mn}_{(1-x)}\text{Cr}_x\text{SiO}_4$ samples show increased discharge capacities. For $x = 0.03$ and 0.10, the discharge capacities are 224 and 219 mAh g^{-1} , respectively, at the fifth cycle, which indicate 1.34 and 1.31 electron transfers per unit formula. Although these capacities decrease to 171 and 162 mAh/g (i.e., 1.04 and 0.97 electron transfers per unit formula) on the tenth cycle, the capacity retention is still greatly improved, as compared to that of the un-doped $\text{Li}_2\text{MnSiO}_4$ powder. The highest capacity obtained is at $x = 0.06$. On the 5th cycle, the discharge capacity of $\text{Li}_2\text{Mn}_{0.94}\text{Cr}_{0.06}\text{SiO}_4$ reaches the maximum of 306 mAh/g, corresponding to 1.83 electron transfer and 91.9% of theoretical capacity (Figure 6C). Even after 20 cycles, the discharge capacity retains at 247 mAh/g (1.48 electron transfer), indicating a relatively

high retention of 80.8% from the initial capacity.

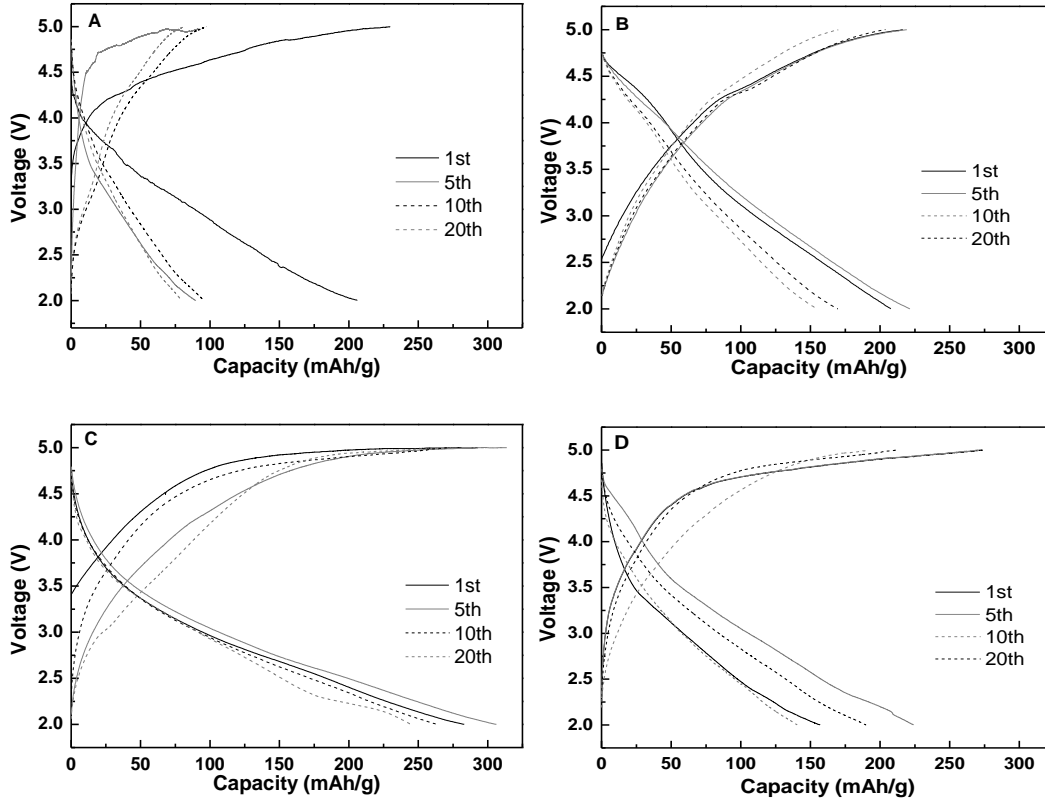


Figure 5-6. Charge-discharge curves of (A) $\text{Li}_2\text{MnSiO}_4$, and $\text{Li}_2\text{Mn}_{(1-x)}\text{Cr}_x\text{SiO}_4$ powders with (B) $x=0.03$, (C) $x=0.06$, and (D) $x=0.10$.

The highest capacity for $\text{Li}_2\text{Mn}_{(1-x)}\text{Cr}_x\text{SiO}_4$ powders is achieved when the Cr doping is 0.06. At this doping level, the enlargement of crystal unit cell volume is known to occur according to the XRD diffraction results (Table 1). Theoretically, Cr^{3+} does not participate in the charge-discharge process. However, the expansion in the crystal lattice could allow more space for lithium insertion and de-insertion. During the de-insertion

process, due to the unchangeable radius of Cr^{3+} , the lattice shrinking is minimized by the support of Cr^{3+} dopant ions. Therefore, Cr^{3+} acts as a pillar to prevent the lattice collapse during cycling. However, as the Cr doping increases to 0.10, the lattice structure drops back to a smaller unit cell volume, and the capacity reduces as a result. Therefore, the optimal ratio of Cr doping is 0.06 among all three ratios studied.

To further improve the electrochemical properties by improving the conductivity of the electrode, $\text{Li}_2\text{Mn}_{0.94}\text{Cr}_{0.06}\text{SiO}_4$ /carbon nanofibers were prepared by electrospinning. The charge-discharge curves of $\text{Li}_2\text{Mn}_{0.94}\text{Cr}_{0.06}\text{SiO}_4$ /carbon nanofibers are shown in Figure 5-7. Comparing Figures 5-6 and 5-7, it is seen that an increased discharge capacity can be observed after incorporating the $\text{Li}_2\text{Mn}_{0.94}\text{Cr}_{0.06}\text{SiO}_4$ powder into the carbon nanofiber matrix. The discharge capacity starts at 295 mAh/g (1.77 electron transfer) at the first cycle and reaches the highest value of 314 mAh/g (1.88 electron transfer) at the 5th cycle. At the 20th cycle, the discharge capacity still remains at 273 mAh/g, indicating an ongoing 1.63 electron transfer reaction per formula unit.

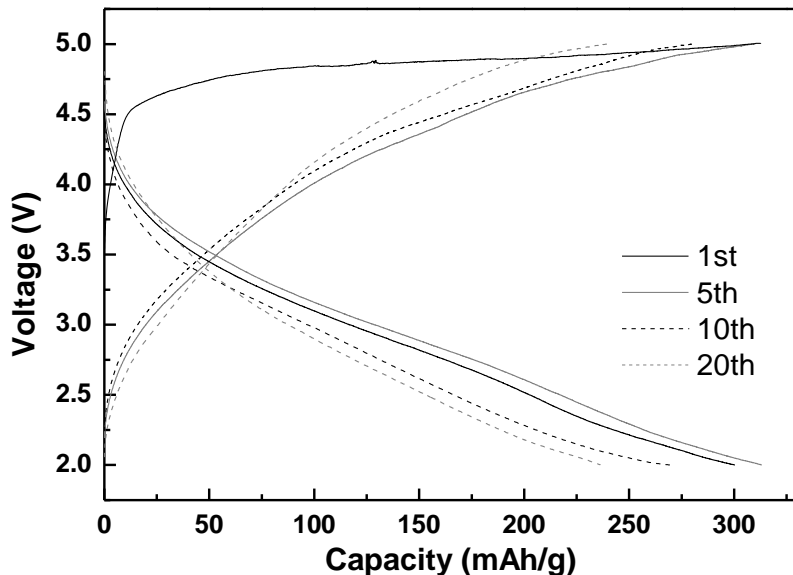


Figure 5-7. Charge-discharge curves of $\text{Li}_2\text{Mn}_{0.94}\text{Cr}_{0.06}\text{SiO}_4/\text{carbon nanofibers}$.

A comparison of the cycling performance of $\text{Li}_2\text{MnSiO}_4$ powder, $\text{Li}_2\text{Mn}_{0.94}\text{Cr}_{0.06}\text{SiO}_4$ powder, and $\text{Li}_2\text{Mn}_{0.94}\text{Cr}_{0.06}\text{SiO}_4/\text{carbon nanofibers}$ is shown in Figure 5-8. Among all three samples, $\text{Li}_2\text{Mn}_{0.94}\text{Cr}_{0.06}\text{SiO}_4/\text{carbon nanofibers}$ show the highest capacity retention of 65.8% at the 50th cycles. The improved electrochemical performance may be contributed to the small particle size and fiber diameter, large surface area, and conductive carbon matrix over which lithium diffusion and charge transfer could occur.^[9,10,11,12] There are several advantages that carbon composite nanofibers possess. Firstly, due to the short diffusion lengths for lithium ions and electrons between the active particles, the carbon nanofibers could increase the rates of lithium insertion and extraction.^[9] Secondly, with high surface-to-volume ratios, the nanofiber structure allows more contact between the electrode and electrolyte.^[13,14] Finally, dispersing active

cathode particles into the carbon nanofiber matrix can effectively prevent the accumulation of primary particles to form large agglomeration.^[13] Therefore, $\text{Li}_2\text{Mn}_{0.94}\text{Cr}_{0.06}\text{SiO}_4$ /carbon nanofibers combine the advantages of size reduction, carbon additive, and nanofiber structure, and exhibit high capacities and improved cycling performance.

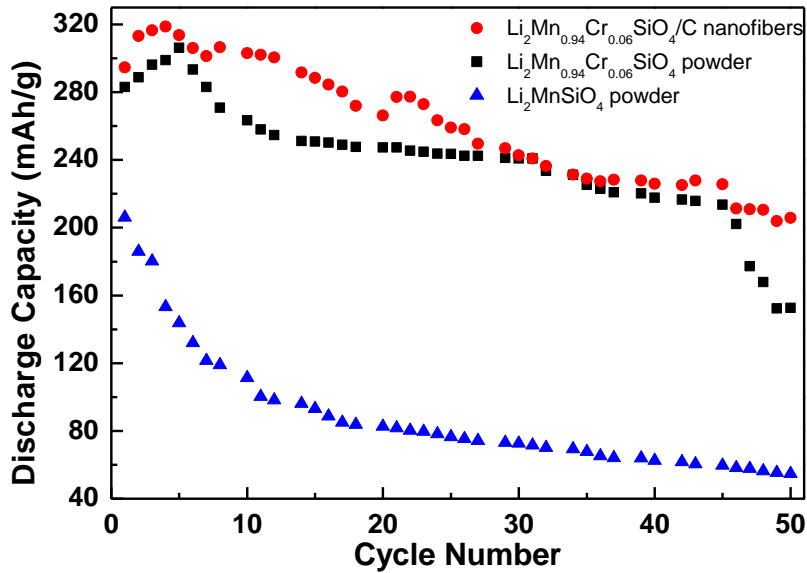


Figure 5-8. Cycling performance of $\text{Li}_2\text{MnSiO}_4$ powder, $\text{Li}_2\text{Mn}_{0.94}\text{Cr}_{0.06}\text{SiO}_4$ powder, and $\text{Li}_2\text{Mn}_{0.94}\text{Cr}_{0.06}\text{SiO}_4$ /carbon nanofibers.

4. Conclusions

In this study, $\text{Li}_2\text{MnSiO}_4$ was doped with different Cr ratios. XRD patterns of $\text{Li}_2\text{Mn}_{(1-x)}\text{Cr}_x\text{SiO}_4$ powders ($x = 0.03, 0.06, \text{ and } 0.1$) showed enlarged crystal unit cell volumes,

which prevented the crystalline structure from collapsing and improved the structural stability of the material during charge/discharge cycles. At a Cr doping ratio of 0.06, the obtained $\text{Li}_2\text{Mn}_{0.94}\text{Cr}_{0.06}\text{SiO}_4$ showed the best performance in terms of high capacity and improved cycling behavior due to the maximum unit cell volume.

$\text{Li}_2\text{Mn}_{0.94}\text{Cr}_{0.06}\text{SiO}_4$ /carbon nanofibers were also prepared by electrospinning, and improvements in capacity and cycling performance were achieved. The carbon nanofiber matrix contributed to the faster electron and ion transportation, leading to better reversibility of this new cathode material.

References

1. S. Yang, Y. Song, P.Y. Zavalij, M.S. Whittingham, *Electrochemistry Communications*, 2002, 4, 239.
2. A. Nyten, A. Abouimrane, M. Armand, T. Gustafsson, J.O. Thomas, *Mater. Chem.* 2005, 7, 156.
3. A. Nyten, S. Kamali, L. Hangstrom. T. Gustafsson, J.O. Thomas, *Mater. Chem.*, 2006, 16, 2266.
4. R. Dominko, M. Bele, A. Kokalj, M. Gaberscek, J. Jamnik, *Journal of Power Sources*, 2007, 174, 457.
5. Y. Li, Z. Gong, Y. Yang, *Journal of Power Sources*, 2007, 174, 528.
6. A. Kokalj, R. Dominko, G. Mali, A. Meden, M. Gaberscek, J. Jamnik, *Chem. Mater.*, 2007, 19, 3633.

7. R. Dominko, M. Bele, M. Gaberscek, A. Meden, M. Remskar, J. Jamnik, *Electrochemistry Communications*, 2006, 8, 217.
8. V. Nalbandyan, V. Politaev, Rostov State Univ., Rostov-na-Donu, ICDD, Russia 2003.
9. S. Vavaliere, S. Subianto, I. Savych, D.J. Jones, J. Roziere, *Energy Environ. Sci.*, 2011, 4, 4761.
10. L. Ji, Z. Lin, X. Zhang, *Carbon*, 2009, 47, 3219.
11. L. Ji, X. Zhang, *Energy & Environmental Science*, 2010, 3, 124.
12. O. Toprakci, L. Ji, Z. Lin, H.A.K. Toprakci, X. Zhang, *Journal of Power Sources*, 2011, 196, 7692.
13. Z. Lin, L. Ji, M. Woodroof, X. Zhang, *Journal of Power Sources*, 2010, 195, 5025.
14. L. Ji, K.H. Jung, A.J. Medford, X. Zhang, *J. Mater. Chem.*, 2009, 19, 499.

Chapter 6 LiF/Fe/Carbon Nanofibers as High-Energy Cathode Materials for Li-Ion Batteries

LiF/Fe/carbon nanofiber composites with different morphologies were prepared by electrospinning of LiF/ferrocene/polyacrylonitrile (PAN) solutions with different polymer concentration, followed by heat-treating the precursor composite in furnace. X-ray diffraction (XRD) and scanning electron microscopy were employed to study the structural variations of all samples. Fe and carbon nanofibers were obtained from the thermal decomposition of ferrocene and PAN precursors. Electrochemical performances were evaluated by using prepared composites as cathode materials in Li-ion batteries. The conditions to obtain uniform distribution of LiF/Fe in carbon nanofibers were investigated. The effects of morphology and structure of composites on electrochemical properties were discussed.

1. Introduction

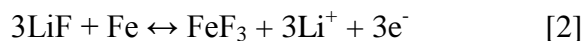
Li-ion batteries have been considered as one of the most promising candidates for large-scale power source and energy storage devices for the near future. However, although they possess numerous advantages such as high voltage and long cycle life, the rapidly growing demand of portable energy storage for electric vehicles and electronic tools requires further improvement in the energy density of Li-ion batteries. Among various factors limiting the performance of Li-ion batteries, the most crucial one relates to the low capacity of current cathode materials [1]. To reach the highest possible cathode

capacity, all the possible oxidation states of the active material should be utilized [2]. Iron trifluoride (FeF_3) was firstly studied by Arai et al. [3] because of its high theoretical capacity of 237 mAh g^{-1} per 1 electron transfer. With this material, a high capacity of 712 mAh g^{-1} can theoretically be achieved through a reversible conversion reaction which proceeds



However, due to the insulating nature of FeF_3 with a low conductivity of $10^{-17} \text{ S cm}^{-1}$, the observed reversible capacity for pure FeF_3 was only around 80 mAh g^{-1} [4].

Previous studies pointed out that it is essential to improve the transport properties of FeF_3 , which can be achieved by decreasing particle size, adding conductive additives, modifying particle surface, and optimizing microstructure [2,5]. Badway et al. demonstrated a highly reversible capacity of 600 mAh g^{-1} for FeF_3 by making it into FeF_3/C nanocomposites through high-energy milling. It was believed that nanosized carbon crystals introduced a great number of surface defects and enhanced electronic and ionic conductivities [6]. Although FeF_3/C has high a reversible capacity, it does not have lithium and cannot be directly used with graphite or other non-lithium anode materials in rechargeable Li-ion batteries. Hence, it is preferable to prepare LiF/Fe based composites. When a LiF/Fe composite is used as the cathode, the following reversible displacement reaction occurs [7]:



Several techniques have been employed to prepare LiF/Fe composites, including pulsed laser deposition [8,9], ultrahigh vacuum evaporation [10,11], and combinatorial sputtering [7]. However, no detailed performance was reported and the needs for the use of precision instruments limited their practical applications. Furthermore, to be used in rechargeable Li-ion batteries, Fe must be in the metallic form as an initial component to prelithiate the cathode [12]. Therefore, it is essential to explore a feasible method to both produce metallic Fe and enhance the conductivity of LiF.

Ferrocene is an excellent source for metallic Fe. It was found that under a high temperature in inert gas, ferrocene can be decomposed to Fe nanoparticles, and these particles work as nucleators for the formation of carbon nanotubes [13,14]. We hereon report a novel method to fabricate LiF/Fe/C nanofibers as a new cathode material by thermally treating electrospun LiF/ferrocene/polymer precursor nanofibers. Our concept is rooted in the fact that both carbon nanofiber formation and iron production can be performed at the same thermal condition, which allows the LiF/Fe/C nanofiber cathode material to be synthesized in one thermal treatment process. The effect of carbon nanofiber structure on the electrochemical performance of this cathode material is discussed on the basis of the experimental data.

2. Experimental

2.1 Chemicals

N,N-dimethylformamide (DMF), ferrocene ($\text{FeC}_{10}\text{H}_{10}$, 98%), lithium fluoride (LiF , >99.98%) were purchased from Sigma-Aldrich Chemical Company (USA).

Polyacrylonitrile (PAN, $M_w = 150,000$) was ordered from Pfaltz & Bauer Inc.

Electrolyte composed of 1 M of lithium hexafluorophosphate (LiPF_6) in a mixture of ethylene carbonate (EC), diethyl carbonate (DEC), and dimethyl carbonate (DMC) with a volume ratio of 1:1:1 was purchased from MTI corporation. All materials were used as received without further purification.

2.2 Fabrication of LiF/Fe/C nanofibers

Weighed LiF, ferrocene and PAN were added into DMF and were mechanically stirred at 60 °C for at least 24 hours to obtain four precursor solutions for electrospinning. The precursor concentrations (LiF + ferrocene + PAN) of the four solutions were 11, 16, 21, and 26 wt%, respectively. All solutions kept a constant LiF:ferrocene: PAN weight ratio of 1:22:14.

A variable high voltage power supply (Gamma ES40P-20W/DAM) was used to provide a high voltage of 20 kV for the electrospinning of the precursor solutions. The feed rate and the needle-collector distance were fixed at 1 mL h⁻¹ and 15 cm, respectively. Electrospun nanofibers were deposited on the collector as free-standing and flexible mats.

The heat treatment of LiF/ferrocene/PAN nanofibers was performed in a programmable electric furnace. The collected nanofiber mats were firstly stabilized under air at 280 °C for 5 hours (heating rate was 5 °C min⁻¹), and then were carbonized in Argon at 900 °C for 8 hours (heating rate was 2 °C min⁻¹) to form LiF/Fe/C composite nanofibers.

2.3 Structure Characterization

The morphology of both LiF/ferrocene/PAN and LiF/Fe/C nanofibers was evaluated using scanning electron microscopy (SEM, Hitachi S3200 VPSEM). The structure variations were identified by X-ray diffraction (Rigaku Smartlab) and energy-dispersed X-ray spectroscopy (EDX, JEOL 6400 FESEM at 5kV) with element mapping. The fiber diameters and particle sizes were obtained based on measuring at least 100 randomly selected fibers in SEM images using Revolution v1.6.0 software.

2.4 Electrochemical Evaluation

The electrochemical performance of LiF/Fe/C nanofibers was investigated by using two-electrode coin-type half cells (CR2032) with metallic lithium as the counter electrode. LiF/Fe/C nanofibers form free-standing porous membranes and they were directly punched into working electrodes of 0.5 inch in diameter. A polypropylene film (Celgard 2400) was used as the separator. All materials were dried in vacuum oven at 120 °C for one day before they were transferred into the glove box. The coin cell assembly was carried out under dry argon atmosphere in the glove box. The galvanostatic charge/discharge characteristics of the cells were recorded with a LAND battery-testing

system in the voltage range of 0.5 - 4.2 V at room temperature. The specific capacities were calculated based on the weight of active materials (LiF and Fe) measured by elemental analysis.

3. Results and Discussion

3.1 X-ray Diffraction Analysis

X-ray diffraction was employed to identify the composition of as-prepared LiF/Fe/C composite nanofibers, and Figure 6-1 show a representative X-ray diffraction pattern of LiF/Fe/C composite nanofibers prepared from 16 wt% precursor solution (PAN:ferrocene:LiF weight ratio = 14:22:1). The XRD data reveal that metallic Fe was produced from ferrocene after thermal treatment. LiF remained as a major component in the final product.

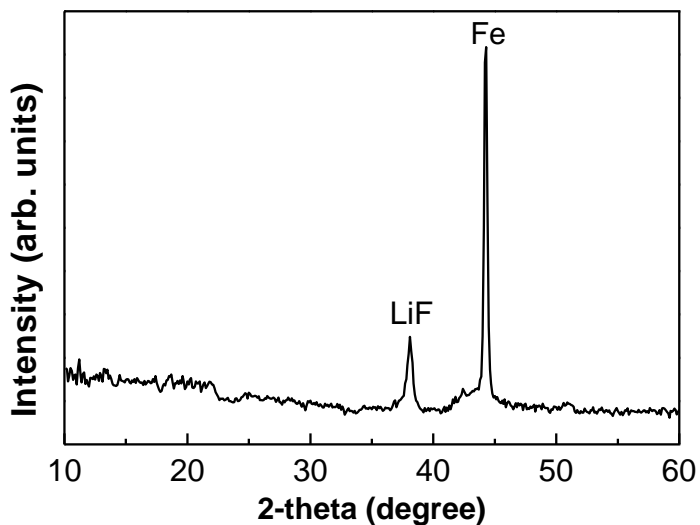


Figure 6-1. X-ray diffraction pattern of LiF/Fe/C composite nanofibers prepared from 16

wt% precursor solution.

Figure 6-2 shows the energy-dispersive (EDX) X-ray spectrum of LiF/Fe/C nanofibers.

The result also confirms the existence of Fe, carbon, fluoride, and trace amount of oxygen as well, which may be introduced during the stabilization step of PAN.

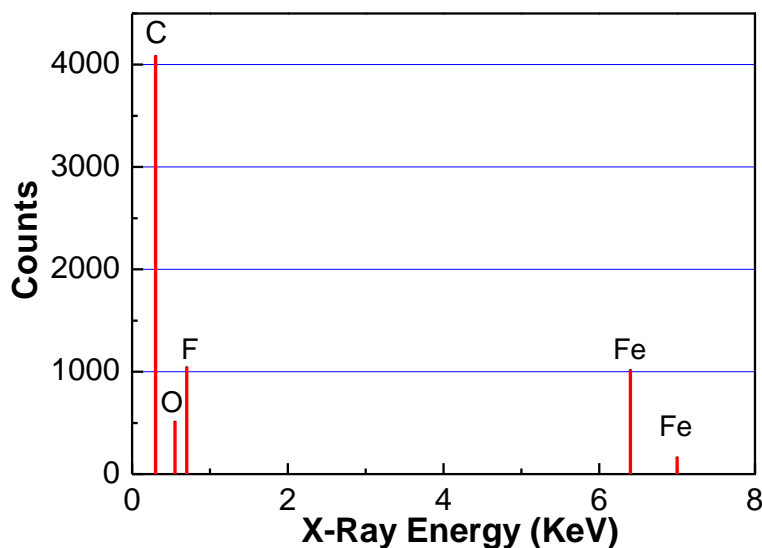


Figure 6-2. Energy-dispersive X-ray spectrum of LiF/Fe/C composite nanofibers prepared from 16 wt% precursor solution.

3.2 Morphology and Structure Characterization

In order to understand the effect of fiber morphology on the electrochemical performance, composite nanofibers with different morphologies were prepared. Figure 6-3 presents SEM images of electrospun LiF/ferrocene/PAN precursor nanofibers before heat treatment. It is seen that the fiber morphology heavily depends on the concentration in the

precursor solutions.

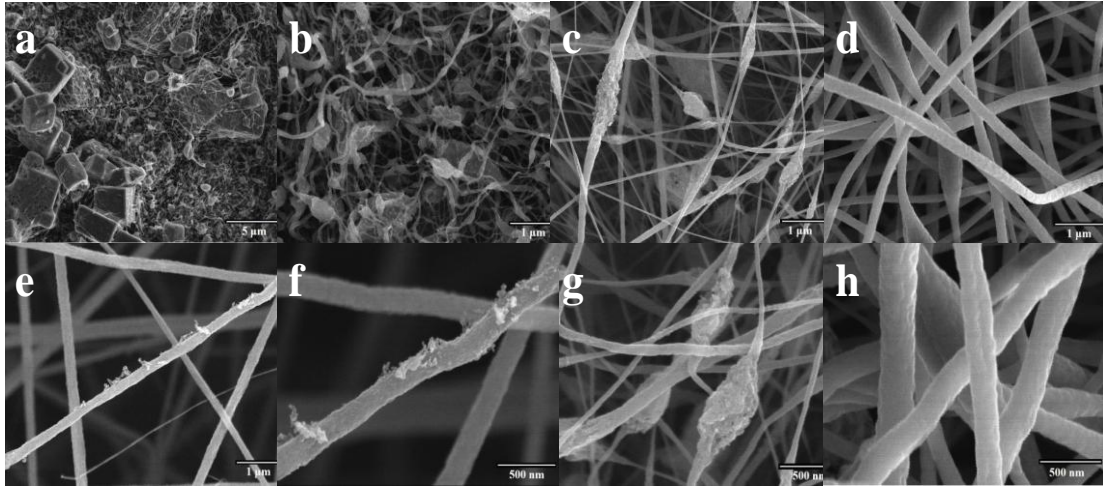


Figure 6-3. SEM images of LiF/ferrocene/PAN nanofibers electrospun from: (a,b) 11, (c,d) 16, (e,f) 21, and (g,h) 26 wt% precursor solutions.

The diameter distributions of LiF/ferrocene/PAN nanofibers prepared from solutions of different precursor concentrations are revealed in Figure 6-4. Fibers fabricated from the 11 wt% precursor solution shows the smallest average diameter of around 79 ± 12 nm. These slim fibers have less capability to hold LiF and ferrocene particles. As shown in Figures 6-3a and b, a significant amount of particles aggregate and form clusters instead of being embedded into the fiber matrix. With a higher precursor concentration of 16 wt%, more particles are loaded into the fibers, but particle aggregations are still present and form so-called ‘beads on the string’ morphology (Figures 6-3c and d). At the same time, the fiber diameter increases to 116 ± 21 nm. When the precursor concentration is 21 wt%, fibers become more uniform and no large clusters can be observed (Figure 6-3e and

f). The average fiber diameter increases to 175 ± 33 nm. When the precursor concentration further increases to 21 wt%, the fiber diameter increases to 204 ± 48 nm. As shown in Figures 6-3g and h, almost all particles are embedded into the nanofiber matrix. However, clumps are present again, which may be caused by the aggregation of LiF/ferrocene particles inside the fiber.

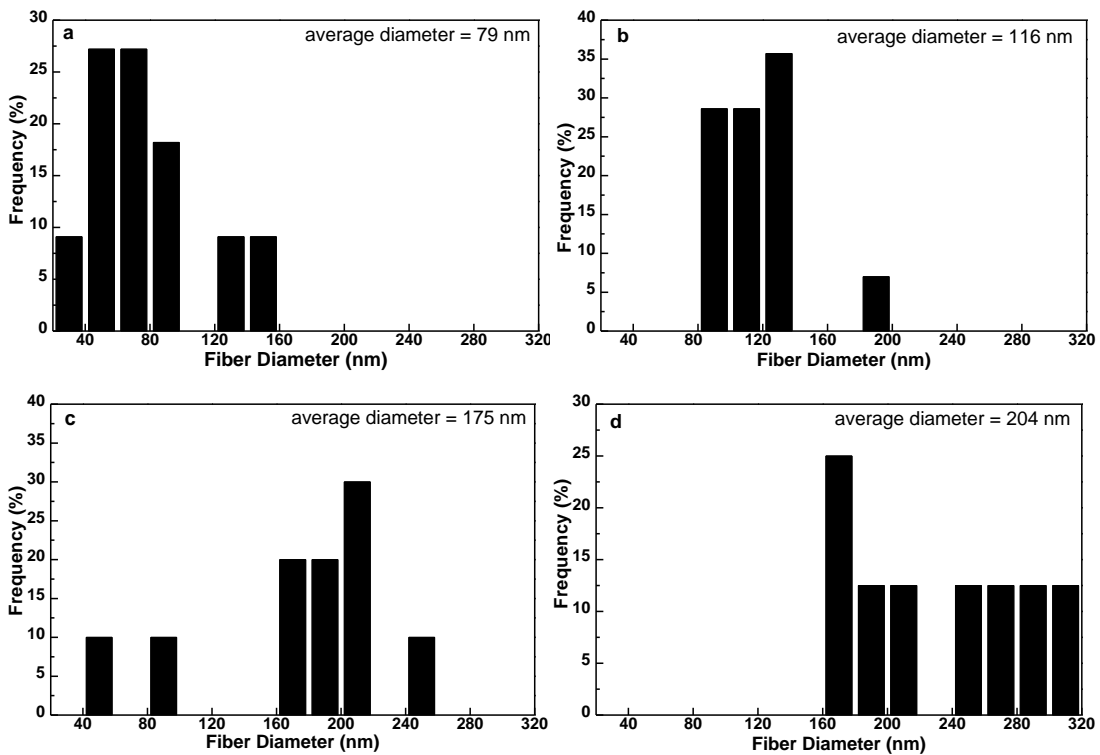


Figure 6-4. Diameter distributions of LiF/ferrocene/PAN nanofibers prepared from: (a) 11, (b) 16, (c) 21, and (d) 26 wt% precursor solutions.

SEM images and fiber diameter distributions of LiF/Fe/C composite nanofibers after heat treatment are presented in Figures 6-5 and 6-6, respectively. It is seen that all nanofibers

show size reduction after heat treatment due to the removal of various species at high temperatures. The average diameters are 74 ± 11 , 92 ± 22 , 148 ± 31 , and 178 ± 45 nm, respectively, for LiF/Fe/C composite nanofibers prepared from 11, 16, 21, and 26 wt% precursor solutions. With a low precursor concentration of 11 wt%, the aggregations of LiF and Fe particles can be clearly seen (Figures 6-4a and b). The particle/aggregation size is 334 ± 54 nm. With higher precursor concentrations, the LiF/Fe/C composite nanofibers show more uniform morphology although aggregations still occur. As shown in Figures 4c and d, with 16 wt% precursor concentration, the nanofibers are still not thick enough to prevent active particles from aggregating on the fiber surface, and the particle/aggregation size is measured to be 75 ± 28 nm. From Figures 4e and f, it is seen that composite nanofibers prepared from the 21 wt% precursor solution present the most homogeneous morphology with small active particles (33 ± 14 nm) distributed uniformly along the nanofibers. However, when the precursor concentration increases to 26 wt%, the fibers become thicker and the particle/aggregation size increases to 136 ± 36 nm.

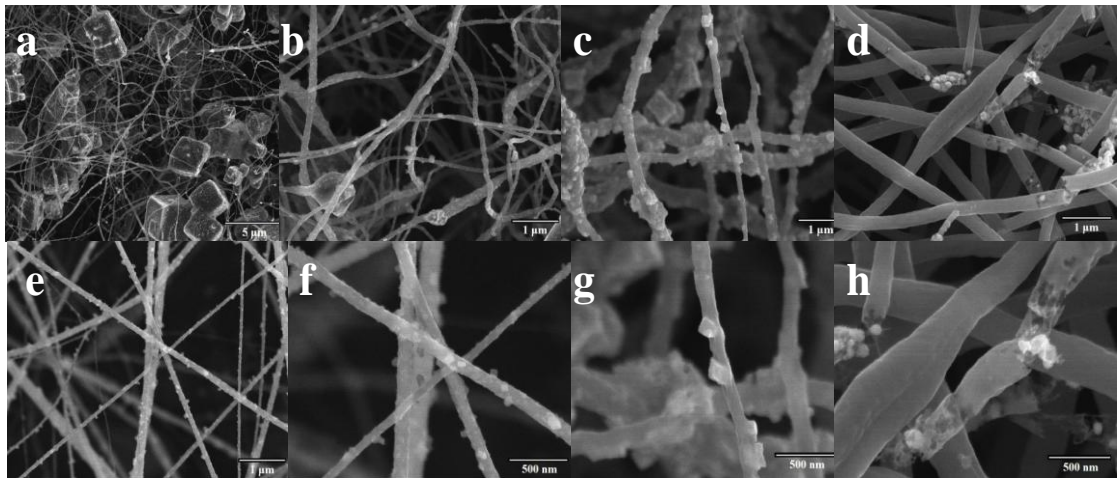


Figure 6-5. SEM images of LiF/Fe/C nanofibers prepared from: (a,b) 11, (c,d) 16, (e,f) 21, and (g,h) 26 wt% precursor solutions.

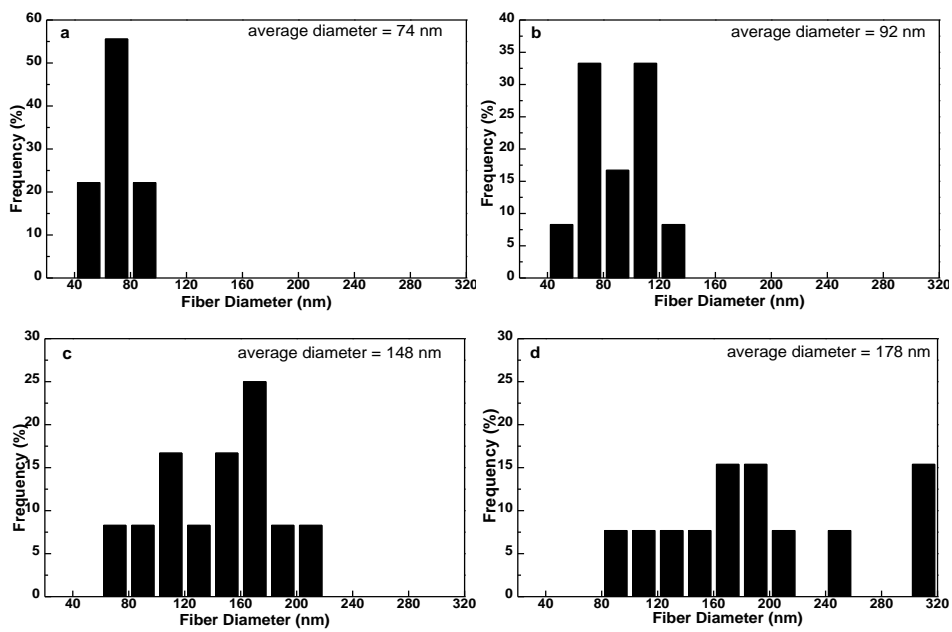


Figure 6-6. Diameter distributions of LiF/Fe/C nanofibers prepared from: (a) 11, (b) 16, (c) 21, and (d) 26 wt% precursor solutions.

Backscatter SEM images of LiF/Fe/C composite nanofibers prepared from 21 wt% precursor solution are provided in Figure 7. Since heavy atoms with higher atomic numbers are stronger scatterers than light ones, compositional information can be obtained from images with back-scattered electrons [12]. The contrast between areas with carbon (darker areas) and LiF/Fe (brighter areas) indicates a fine distribution of active particles along the carbon nanofiber matrix.

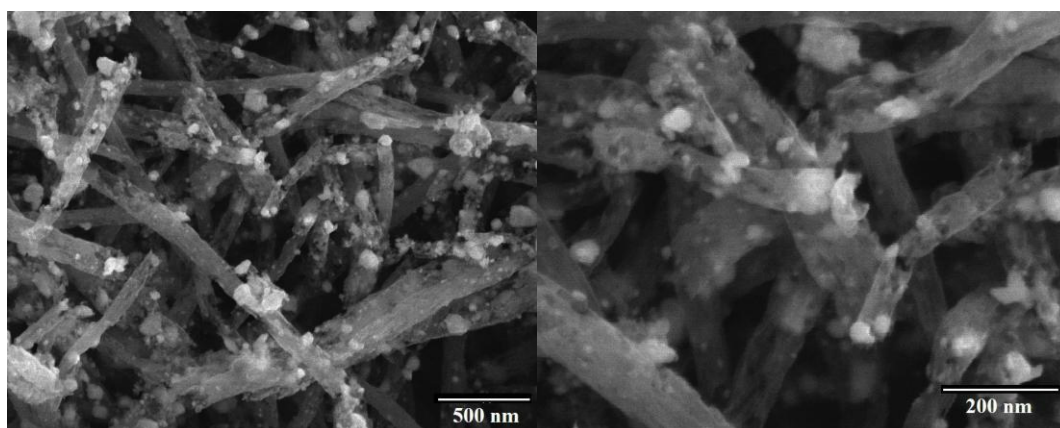


Figure 6-7. Backscatter SEM images of LiF/Fe/C composite nanofibers prepared from 21 wt% precursor solution. The bright dots indicate LiF and Fe particles.

3.3 Electrochemical Properties

To evaluate the electrochemical performance of LiF/Fe/C composite nanofibers, charge-discharge cycles were conducted at room temperature between 0.5 to 4.2 V with a current density of 35.6 mA g^{-1} , and the results are shown in Figure 6-8. The discharge capacities of LiF/Fe/C composite nanofibers prepared from 11, 16, 21, and 26 wt% precursor solutions are 327.6, 543.6, 589.9, and 367.5 mAh g^{-1} , respectively, at the first cycle. No

significant capacity losses are found in the 10th and 30th cycles. Compared with the capacities of current cathode materials LiCoO₂ (about 140 mAh g⁻¹) and LiMn₂O₄ (about 130 mAh g⁻¹), a high discharge capacity of 596.5 mAh g⁻¹ for LiF/Fe/C nanofibers prepared from the 21 wt% precursor solution is a significant achievement.

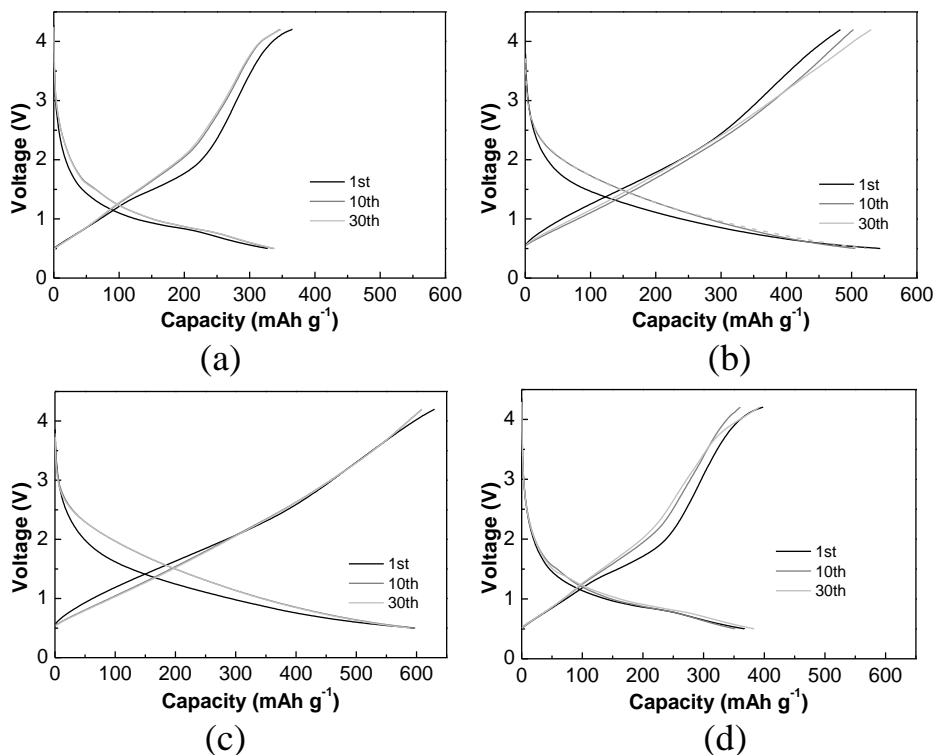


Figure 6-8. Galvanic charge-discharge curves of LiF/Fe/C nanofibers prepared from: (a) 11, (b) 16, (c) 21, and (d) 26 wt% precursor solutions.

The cycling performance of LiF/Fe/C composite nanofibers prepared from solutions of four different precursor concentrations are shown in Figure 6-9. In addition to the high initial discharge capacities, good capacity retention is obtained for all four LiF/Fe/C nanofibers. For LiF/Fe/C nanofibers prepared from the 21 wt% precursor solution, the

discharge capacity remains at 588.8 mAh g⁻¹ at 50th cycle, indicating that the displacement reaction between 3LiF and Fe is electrochemically reversible (see Reaction 2).

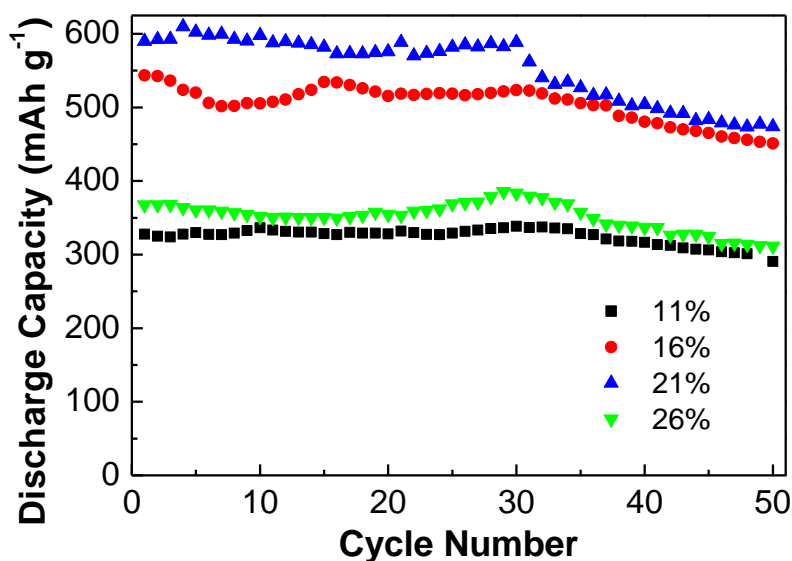


Figure 6-9. Cycling performance of LiF/Fe/C nanofiber composites prepared from precursor solutions with different concentrations.

The electrochemical properties of LiF/Fe/C nanofibers are related to the homogeneity of their morphology and structure. For lithiation reaction to take place, it is essential to have enough contact points between LiF and Fe. For LiF/Fe/C nanofibers prepared from the 11 and 16 wt% precursor solutions, the fiber diameters are too small and the nanofiber matrix cannot hold LiF/Fe particles, resulting in severe particle/fiber phase separation (Figures 5a, b, c, and d). For nanofibers prepared from the 26 wt% precursor solution, the fiber diameter is too large and severe LiF/Fe particle aggregation occurs inside the fiber

(Figures 5g and h). Uniform nanofiber structure with well-distributed active particles is ideal for the displacement reaction between 3LiF and Fe , which is achieved in LiF/Fe/C nanofibers prepared from the 21 wt% precursor solution. Therefore, among all samples studied, LiF/Fe/C nanofibers prepared from the 21 wt% precursor solution have the best electrochemical performance, in terms of high capacity and stable cycling behavior.

The excellent performance of LiF/Fe/C nanofibers is determined by its unique structure. The effective contact between LiF and Fe is important [14]. LiF/Fe/C nanofibers have high surface-to-volume ratio and small fiber diameter, which enable more contact between LiF and Fe . At an appropriate solution composition (e.g., precursor concentration = 21 wt%), LiF and Fe particles are dispersed relatively uniformly along the carbon nanofiber matrix, which can prevent them from accumulating to form large aggregations [15,16]. In addition, the carbon nanofiber matrix allows fast lithium diffusion and charge transfer, which promotes rapid lithiation/delithiation reaction [17-20].

However, it is noticeable that the majority of discharge capacities are obtained in the region of 1.0 to 2.0 V (Figure 8). The working potentials for all samples are lower than the theoretical value (2.74 V). Similar phenomena have been found by other research groups [21,22]. For example, Badway et al. used high-energy milling to prepare LiF/Fe/C nanocomposites and found that, although there are two plateaus existing (2.0 V and 3.5 V), over 60% of the total discharge capacity was obtained below 2.0 V [22]. This can be related to the slow kinetics of this cathode material and, therefore, exploring new methods to obtain better particle distribution and faster kinetics for LiF/Fe/C nanofiber

cathode materials should be addressed in the future work.

4. Conclusions

LiF/Fe/C nanofiber cathodes with different structures were prepared by using ferrocene as the Fe precursor and PAN as the carbon source. Their structures were investigated by XRD and SEM. It was found that LiF/Fe/C composite nanofibers prepared from a 21 wt% precursor solution show the most uniform structure with evenly distributed active particles encapsulated by the carbon nanofiber matrix. The electrochemical evaluation indicates a relationship between composite morphology and electrochemical properties. The more homogeneous distribution of active particles in the carbon nanofiber matrix leads to better electrochemical performance, in terms of high capacity and stable cycling behavior.

References

- [1]. F. Badway, N. Pereira, F. Cosandey, G.G. Amatucci, *Solid State Ionics*, 2002, 756, 207.
- [2]. F. Badway, F. Cosandey, N. Pereira, G.G. Amatucci, *Journal of the Electrochemical Society*, 2003, 150(10), A1318.
- [3]. H. Arai, S. Okada, Y. Sakurai, J. Yamaki, *Journal of Power Sources*, 1997, 68, 716.
- [4]. M. Lascaud, A. Lachter, J. Salarfenne, A.S. Barriere, *Thin Solid Films*, 1979, 59, 353.
- [5]. F. Badway, N. Pereira, F. Cosandey, G.G. Amatucci, *Journal of Electrochemical Society*, 2003, 150, 1209.

- [6]. J. Maier, *Solid State Ionics*, 2002, 148, 367.
- [7]. P. Liao, R.A. Dunlap, J.R. Dahn, *Journal of Physics: Condensed Matter*, 2008, 20, 55203.
- [8]. Y. Makimura, A. Rougier, L.Laffont, M. Womes, J.C. Jumas, J.B. Leriche, J.M. Tarascon, *Electrochemistry Communications*, 2006, 8, 1769.
- [9]. Y. Zhou, W. Liu, M. Xue, L. Yu, C. Wu, X. Wu, Z. Fu, *Electrochemical and Solid-State Letters*, 2006, 9(3), A147.
- [10]. M. Ochi, E. Kita, N. Saegusa, T. Erata, A. Tasaki, *Journal of Physical Society*, 1992, 61, 35.
- [11]. E. Kita, M. Ochi, T. Erata, A. Tasaki, *Journal of Magnetism and Magnetic Materials*, 1992, 117, 294.
- [12]. J. C. H. Spence, *High-Resolution Electron Microscopy*, Oxford University Press, 3rd Ed., 2003
- [13]. G.G. Amatucci, N. Pereira, F. Badway, M. Sina, F. Cosandey, M. Ruotolo, C. Cao, *Journal of Fluorine Chemistry*, 2011, 6, 33.
- [14]. D. Conroy, A. Moisala, S. Cardoso, A. Windle, J. Davidson, *Chemical Engineering Science*, 2010, 65, 2695.
- [15]. A. Moisala, A.G. Nasibulin, D.P. Brown, H. Jiang, L. Khriachtchev, E. Kauppinen, *Chemical Engineering Science*, 2006, 61, 4393.
- [16]. Z. Lin, L. Ji, M. Woodroof, X. Zhang, *Journal of Power Sources*, 2010, 195, 5025.
- [17]. S. Vavaliere, S. Subianto, I. Savych, D.J. Jones, J. Roziere, *Energy Environ. Sci.*, 2011, 4, 4761.

- [18]. L. Ji, Z. Lin, X. Zhang, *Carbon*, 2009, 47, 3219.
- [19]. L. Ji, X. Zhang, *Energy & Environmental Science*, 2010, 3, 124.
- [20]. O. Toprakci, L. Ji, Z. Lin, H.A.K. Toprakci, X. Zhang, *Journal of Power Sources*, 2011, 196, 7692.
- [21]. H. Li, G. Richter, J. Maier, *Advanced Materials*, 2003, 15, 736.
- [22]. F. Badway, N. Pereira, F. Cosandey, G.G. Amatucci, *Materials Research Society Proceedings*, 2003, 756, EE 7.1.

Chapter 7 Recommended Future Work

The recommended future work can include but not limited to:

1. Carry out electrochemical impedance measurements to identify the kinetics of the reactions in cathode materials and evaluate the impact of carbon nanofibers on the cathode performance.

Electrochemical impedance spectroscopy (EIS) is widely used to characterize the electrode processes and complex interfaces. By preparing a lithium half cell, which uses active materials as the cathode and non-active counterpart as the anode, it is possible to reveal the information related to the reaction mechanism of an electrochemical process on the cathode, because different reaction steps will dominate at certain frequencies and the frequency responses shown by EIS can help identify the rate limiting step. The impedance plot for an electrochemical system is usually composed of two regions- mass transfer control at low frequencies and kinetics control at high frequencies. Therefore, both the impedance of the cathode material and reaction constant k^0 can be obtained from the impedance plot. With this information, by comparing active material/carbon nanofiber composite materials with different compositions and morphologies, we can evaluate the effect of carbon nanofibers on the resistance and charge transfer reactions of cathode materials. Finally, we can determine optimum parameters to prepare and possess the active material/carbon nanofiber composite cathodes.

2. Prepare LiF/Fe/C nanofiber composite cathodes by chemical vapor deposition.

Chemical vapor deposition (CVD) is one of the most versatile techniques to

microfabricate high-purity solid materials. In this method, carbon nanofiber matrix can be used as the substrate. Active materials LiF and Fe are deposited onto the carbon nanofibers substrate by CVD. In this way, a uniform distribution of active particles on carbon nanofiber matrix can be obtained. Particle aggregations are considered as one of the most critical issues to high irreversible capacities and short cycle lives. With more uniform morphology of composite materials achieved by the CVD process, carbon nanofiber matrix act as a suspension host to hold active particles evenly and prevent local agglomerations. Therefore, an improved overall electrochemical performance can be expected, especially the cycle life.

3. Use carbon nanotubes to prepare active material/carbon nanotube cathodes for Li-ion batteries.

Although carbon nanofibers promote charge transfer between active particles, the structures of electrospun carbon nanofibers are usually porous with 100s of nanometers at diameter. The low density of carbon nanofibers sacrifices energy densities of prepared cathode materials. Carbon nanotubes possess the similar properties as carbon nanofibers, but they are more compact than carbon nanofibers. As a result, to fabricate carbon nanotubes with active materials by electrospinning may be a promising way to improve the conductivity of cathode material without compromising the energy density of the composite cathodes.